Multidisciplinary investigations of the Chaman strike-slip fault along the western Indo-Asian collision boundary, Pakistan

……...

A Dissertation

Presented to

the Faculty of the Department of Earth and Atmospheric Sciences

University of Houston

……

In Partial Fulfillment

of the Requirements for the Degree

Doctor of Philosophy

……

By

Shams Ul-Hadi

May 2012

Multidisciplinary investigations of the Chaman strike-slip fault along the western Indo-Asian collision boundary, Pakistan

_____

Shams Ul-Hadi

APPROVED BY:

_____

Dr. Shuhab D. Khan, Associate Professor
(Committee Chair)
Department of Earth and Atmospheric Sciences
University of Houston

_____

Dr. Thomas Lapen, Associate Professor
Department of Earth and Atmospheric Sciences
University of Houston

_____

Dr. Jolante van Wijk, Assistant Professor
Department of Earth and Atmospheric Sciences
University of Houston

_____

Dr. Lewis A. Owen, Professor
Department of Geology
University of Cincinnati, Ohio

_____

Dr. Mark A. Smith, Dean,
College of Natural Sciences and Mathematics
University of Houston

Dedication

Dedicated to my beloved parents, who I will miss throughout my life. My mother (died on December 01, 2009) and my father (died on January 11, 2012) always believed in me and they are a life time inspiration for me. May my Allah bestow His blessing on them, Ameen.

Acknowledgements

Four years ago when I was working in the petroleum industry I met Dr. Shuhab Khan in University of Peshawar when he was visiting Pakistan. Dr. Khan asked me to pursue a Ph.D. in geology at the University of Houston. So I filled out the admission form along with an application for Teaching Assistantship. I got admitted to the Ph.D. geology program in the Department of Earth & Atmospheric Sciences (EAS) at UH, but could not qualify for a TA position due to my low scores in GRE. Then I started to find a sponsor for my studies and I was fortunate enough to get a scholarship from Higher Education Commission (HEC) of Pakistan under the Faculty Development Program at University of Peshawar (UoP). HEC and UoP were generous enough to fund me for three continuous years; without this it would have been impossible to start my Ph.D. at UH. I am greatly indebted to HEC and UoP who supported me in those hard times when money mattered a lot. So I got the scholarship for three years, but normally it takes four years in USA to complete a Ph.D. So at that time I wrote to Dr. Casey (Chairman, Dept. EAS) about my situation and he encouraged me to join UH and that I would be able to get funding for the fourth year of my Ph.D. Many thanks to Dr. Casey for his support throughout my stay here at UH. In fact I got support for my last two semesters from Dr. Khan and I believe that this is one of the turning points in completing my Ph.D. in time. So this is how the four years journey started. In a totally different world it was always hard to get adjusted. Fortunately I was lucky enough to have a brother-like friend, a teacher, and a supporter in the form of Dr. Khan. Besides his guidance in my studies and research he was always there for me in any hardship in my life. As my advisor I would like to mention one

special quality about Dr. Khan, which is his non-stop interaction with students and continuous pushing of students to do more and write. I guess this is the reason that almost all the students who assign him as advisor graduate in time. Since I concentrated on my research project from the first day I was able to defend my dissertation with 3 ½ years, courtesy of Dr. Khan.

In any project each member has to be efficient enough to keep pace with the rest of the team. In my research project I would name Dr. Lewis A. Owen (University of Cincinnati) as the lead of the team. I emailed him about processing my samples at the Cosmo Lab at UC. He replied that we could meet and discuss it during his transit time at Houston Airport on his way from a field trip in Argentina. From there on it started. Besides his guidance during my lab work at UC he has helped me in writing my whole dissertation. I believe that he has gone through my whole dissertation word by word at least five times.

Kate Hedrick helped me understand the process of extracting ^{10}Be from the samples at Cosmo Lab, UC. She is thanked for measuring the samples at PRIME Lab. Purdue University. Dr. Craig Dietsch is thanked for many sessions of discussions and his extended hospitality during my stay at the Department of Geology, UC. Zhenzhu Wan let me stay at her apartment during my visits to UC.

I would like to thank Dr. Tomas Lapen who always encouraged me in my research and helped me in geochemical analysis and U-Pb dating. As a person Tom is very positive and always willing to help anytime. Dr. Jolante van Wijk suggested many corrections and helped me improve the final draft of my dissertation. I am also indebted to Dr. Kevin

Burke, Dr. Alex Robinson, and Dr Mike Murphy for suggestions on my project during the many Structure/Tectonics seminars in the department. Dr. Williaum Dupre´ is specially thanked for editing one of the three manuscripts (Chapter 3).

Dr. Abdul Salam Khan from Baluchistan University, Pakistan helped during my three field trips to the study area. With his help my research became feasible otherwise geological data collection is almost impossible from this politically hostile area. Aziz Ozyavous, Xiong, Veronica Sanchez, Barry Shaulis, and many other fellow students at the department helped me in learning GIS/Remote Sensing, geochemical analysis, and helped me writing my research.

Satellite Imaging Corp. Houston provided the GeoEye-1 image data on educational discount rate. Ellington & Associates, Inc. Houston are thanked for XRF processing of some of the samples on subsidized rates.

This dissertation contains the following three manuscripts that are either in revision or review stages in different journals;

1. Ul-Hadi, S., Khan, S.D., Owen, L.A., and Khan, A.S. Geomorphic response to an active transpressive regime: A case study along the Chaman strike-slip fault, western Pakistan. Earth Surface Process and Landforms (under revision, 2012).

2. Ul-Hadi, S., Khan, S.D., Lapen, T., and Khan, A.S. Geochemistry and geochronology of a part of the pre- to syn-collisonal Chagai-Ras Koh island arc system along the

western Indo-Asian plate boundary. Journal of Asian Earth Sciences (under review, 2012).

3. Ul-Hadi, S., Khan, S.D., Owen, L.A., Khan, A.S., Hedrick, K.A., and Caffee, M.W. Slip rates along the Chaman fault: implication for transient strain along the western Indian plate margin. Tectonophysics (under review, 2012).

Multidisciplinary investigations of the Chaman strike-slip fault along the western Indo-Asian collision boundary, Pakistan

……...

An Abstract of a Dissertation

Presented to

the Faculty of the Department of Earth and Atmospheric Sciences

University of Houston

……

In Partial Fulfillment

of the Requirements for the Degree

Doctor of Philosophy

……

By

Shams Ul-Hadi

May 2012

Abstract

The Chaman left-lateral strike-slip fault bounds the collision zone between Indian and Eurasian plates at the western end of the Himalayan-Tibetan orogen and connects the Makran subduction zone to the Himalayan convergence zone. This western collision boundary received extensive magmatism as Kandahar and Chagai-Ras Koh arcs, which evolved from oceanic to continental arcs before the closure of the neo-Tethyan Ocean and initiation of the left-lateral movement along the Chaman fault as the north-bound translation of the Indian plate continued. Geochemical analyses of the andesitic/basaltic arc rocks exposed west of the Chaman fault show a subduction-related source that was enriched with large ion lithophile elements and depleted with high field strength elements. Younger granitoids intrusions show a source with continental contamination depicting proximity of the Afghan block at the time of emplacement. U-Pb emplacement ages from granitic samples in the Khwaja Amran-Spinatizha area suggest that granitic intrusions within the Chagai-Ras Koh ceased by ~58 Ma as in the Kandahar arc. The fission track ages of ~35 Ma and ~20 Ma from the intrusive rocks of the Chagai-Ras Koh correspond well to the final Indo-Asian collision in the south along the western collision boundary and the initiation of strike-slip movement along the Chaman fault, respectively.

Geomorphic history of an active transpression was reconstructed using digital elevation model data integrated with Advance Spaceborne Thermal Emission and Reflection Radiometer and images from GeoEye-1 to understand the interaction of a strand of the Chaman fault and the Spinatizha thrust fault with the evolving landscape within the

Chaman basin in western Pakistan. Topographic analysis and geomorphic indices of active tectonics reveal northward growth of the thrust with the presence of three water gaps and two wind gaps. Left-lateral displacement along the Chaman fault and uplift along the Spinatizha fault record slip partitioning resulting from the difference in the Chaman fault azimuth and orientation of the velocity vector of the Indian plate. About 1150 m displaced alluvial fan with a ^{10}Be exposure age of ~ 35 kyr along a strand of the Chaman fault yields a slip rate of ~ 33 mm/yr which agrees with the geologically constrained slip rates along the Chaman fault, but is twice as larger than that inferred from global positioning system measurements (~18 mm/yr). This contrast in slip rates accounts either for; 1) transient variations in rates of elastic strain accumulation, such that the geodetic rates might represent a period of reduced displacement as compared to the averaged Late Pleistocene rate; or 2) fault inversion and strain partitioning within the plate boundary zone. While fault inversion could be the reason of strain variations along mega-structures over longer periods of time (>10^6 years), transient strain accumulation could explain contrasting slip rates along the Chaman fault which is late in its seismic cycle.

List of Contents

List of Figures

List of Tables

Chapter 1 : Introduction

The Cenozoic collision between the Indian and Eurasian Plates (Molnar and Tapponnier, 1975) has resulted in the uplift of the Himalayas and formation of the Tibetan Plateau (Yin, 2006) that has significant climatic impacts on a major part of the planet (Burbank, 2005). Paleomagnetic reconstruction of two points on the Indian plate estimates present-day convergence rate between these two plates to be 34–44 mm/yr (Molnar and Stock, 2009) which averages to the GPS constrained 38 mm/yr convergence rate of India (Altamimi et al., 2007). About half of this total Indian plate movement is accommodated by underthrusting of the Indian plate beneath the Himalaya (Thatcher, 2007), but much of the remaining movement is adjusted within the Tibet plateau, either localized along the major scale strike-slip faults (Tapponnier et al., 2001) or distributed within the plateau (England and Molnar, 2005). While many studies (e.g. Bendick et al., 2000; Bilham, 2004; Wright et al., 2004; Chevalier et al., 2005; He and Chéry, 2008) have focused on understanding the deformation along these mega-structures in the Himalaya and Tibet (Figure 1.1), little focus has been given to the western Indian plate boundary which connects the Makran subduction zone in the south and Himalayan convergence zone in the north. This transform boundary is known as Chaman fault system, which includes several subsidiary faults and thrust belts along with the active left-lateral Chaman strike-slip fault which bounds the ~ 100 – 250 km wide shear zone on the west (Lawrence et al., 1992). Understanding of the evolution of the Chaman fault and its Quaternary activity is the main objective of this dissertation. Three major datasets including geochemical/geochronologic, high resolution satellite image, and cosmogenic ray

exposure data are utilized to accomplish this objective. Geochemical analyses and U-Pb dating of the arc rocks from the boundary zone are used to understand the evolution of the collision boundary, while satellite data and CRE dating are used to estimate slip rate along the Chaman fault. A brief outline of the dissertation follows below.

1.1. Dissertation outline

Chapter 2 provides details on the evolution of the western collision boundary. Geochemical analyses were carried out on igneous rocks collected from the Chagai-Ras Koh arc in the south and the Khwaja Amran-Spinatizha Crystalline Complex near the Chaman town in the north. Khwaja Amran-Spinatizha crystalline complex is exposed to the west of the Chaman fault, covering ~ 300 km of the southern part of the Chaman fault. A comparison of these data with the previously published data on the Chagai-Ras Koh arcs and Khwaja Amran-Spinatizha crystalline complex suggests that arc rocks present in the two regions are similar. U-Pb dating of the granitoids from the Khwaja Amran-Spinatizha area gives Paleocene age, which suggests that initiation of collision between the Indian plate and Afghan block started during Paleocene time.

In Chapter 3 satellite remote sensing data coupled with field observations are used to predict fault growth and direction of propagation in an active strike-slip and thrust fault system. A gentle bend in the strike of the Chaman fault provides this opportunity to examine the growth of an active transpression. ASTER 15 m resolution elevation data and multispectral GeoEye-1 data were used to map the pop-up zone of the transpression.

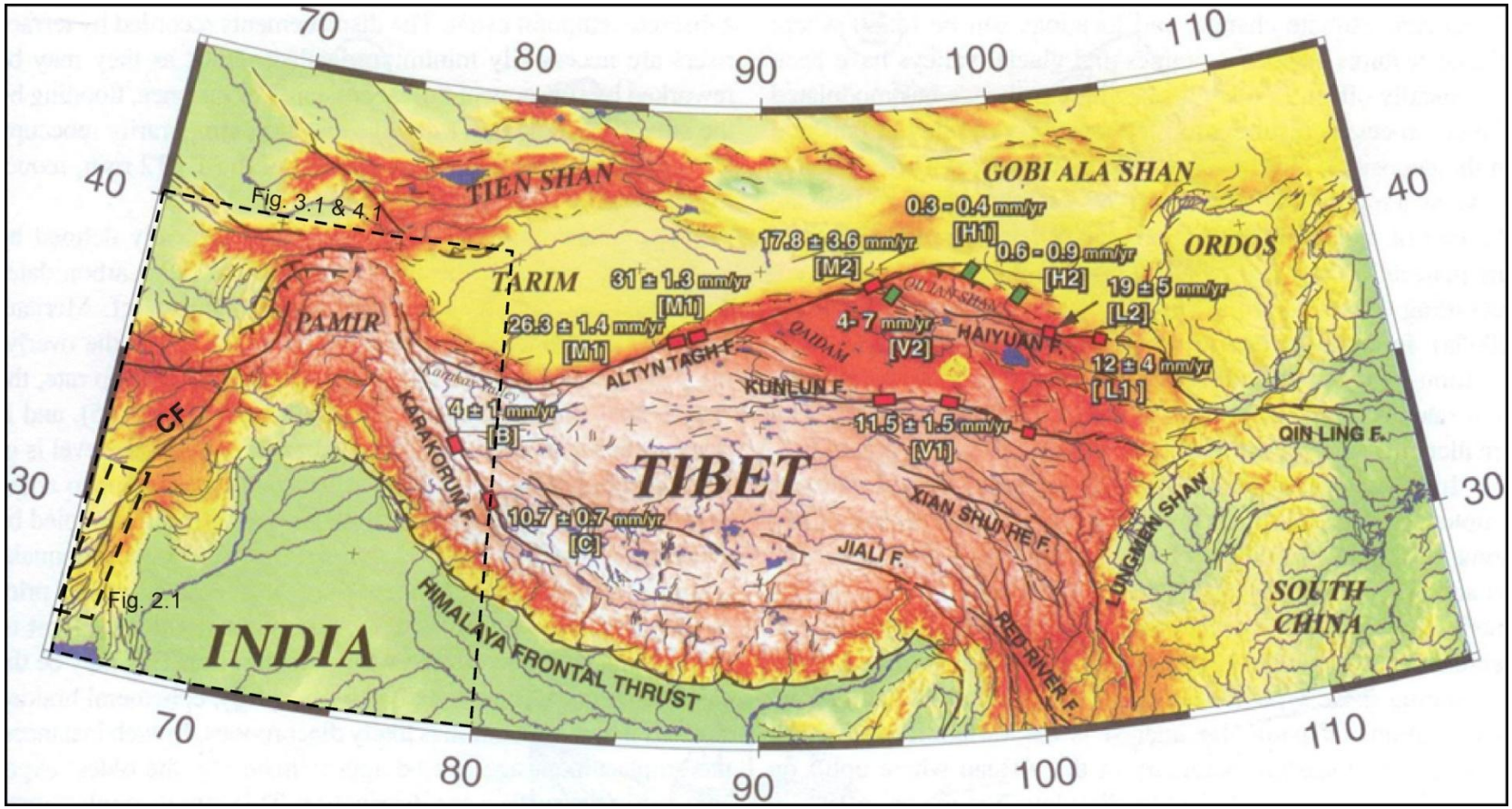

Figure 1.1: Tectonic map of active faults in Himalaya and Tibet displaying the geomorphic slip-rate determinations constrained by cosmogenic, radiocarbon, and optically stimulated luminescence dating (Ryerson et al., 2006). Red boxes are the locations of slip rate on strike-slip faults by Meriaux et al., 2004 (M1); Meriaux et al., 2005 (M2); Van der Woerd et al., 2002b (V1); Lasserre et al., 1999 (L1); Lasserre et al., 2002 (L2); Chevalier et al., 2005 (C); Brown et al., 2002a (B), and green boxes are the individual shortening rates by Van der Woerd et al., 2001 (V2); Hetzel et al., 2002 (H1); Hetzel et al., 2004 (H2). Western collision boundary which includes Chaman fault (CF) is the focus of this study.

These datasets provide insight to the actively interacting landscape in the Chaman basin and the evolving Chaman strike-slip and Spinatizha thrust faults.

Chapter 4 provides an estimate of the slip rate from one site along a strand of the Chaman fault. Displacement along the fault cutting an alluvial fan was seen in the field and measured using the GeoEye-1. The landform surface was sampled to get exposure age of the surface. Beryllium-10 was separated from samples collected from meter-sized boulders on the flat alluvial surfaces and was measured with AMS. Modeled ^{10}Be ages were matched with the observed displacement. Estimated slip rate from this strand of the Chaman fault is compared to the geological slip-rate estimates since the inception of the strike slip movement, and the geodetic slip-rate modeled from GPS and InSAR data to understand kinematic evolution of the Indian plate boundary in Late Quaternary.

Chapter 5 summarizes and correlates all the three aspects of this dissertation and gives a broader evolutionary view of the western Indo-Asian collision boundary.

Chapter 2 : Geochemistry and geochronology of a part of the pre- to syn-collisonal Chagai-Ras Koh island arc system along the western Indo-Asian plate boundary

2.1. Abstract

The western collision boundary between the Indian and Asian plates contains the Knadahar and Chagai-Ras Koh arcs, which developed before the closure of the neo-Tethyan Ocean and initiation of the left-lateral movement along the Chaman fault. Andesitic arc rocks of the Chagai-Ras Koh arc system in the south and Khwaja Amran-Spinatizha Crystalline Complex in the north are exposed west of the Chaman fault in western Pakistan. Geochemical analyses of these andisitc-basaltic rocks show a subduction-related source showing enrichment in large ion lithophile elements (LILE) and depletion in high field strength elements (HFSE). A younger granitoids suite of rocks intruded these andesites/basalts in both areas. The granitic intrusions from both areas show crustal contamination. U-Pb zircon ages of ~62 -58 Ma from three granitic samples in the Khwaja Amran-Spinatizha area suggest that granitic magmatism within the Chagai-Ras Koh arc ceased by ~58 Ma similar to that in Khwaja Amran-Spinatizha and Kandahar arc. The fission track ages of ~ 35 Ma and ~ 20 Ma from the intrusive rocks of the Chagai-Ras Koh correspond well to the final Indo-Asian collision in the south along the western collision boundary and the initiation of strike-slip movement along the Chaman fault, respectively.

2.2. Introduction

The Indo-Asian collision marks closure of the Tethyan Ocean (Yin and Harrison, 2000) the remnants of which are found all along the Himalayan-Tibetan orogen in the form of ophiolites (Tapponnier et al., 1981; Searle, 1986; Treloar and Izatt, 1993). Collision itself has resulted in the emplacement and consequent exhumation of a chain of oceanic to continental volcanic island arcs (Yin, 2006). These island arcs help define the timing of cessation of the Tethyan Ocean and consequent continent-continent collision (Khan et al., 2009). The less explored western collision boundary between Indian plate and the Afghan block, which is marked by the Chaman fault (Lawrence et al., 1992), also received extensive island arc magmatism from the Late Jurassic to Cretaceous in Kandahar and Chagai-Ras Koh arcs (Tapponnier et al., 1981; Debon et al., 1987) and up to Early Quaternary magmatism in Chagai-Ras Koh arc system (Sillitoe and Khan, 1977; Siddiqui, 2004; Figure 2.1), although the later activity was much restricted (Farah et al., 1984). Furthermore, these arc systems were intruded by a whole range of calc-alkaline granitoides (Hunting Survey Corporation Limited 1960; Tapponnier et al., 1981; Debon et al., 1987). As such, the Cretaceous to Paleocene tectonic setup of the western Indo-Asian collision boundary is marked by subduction related oceanic arc volcanism (Treloar and Izatt, 1993). This neo-Tethyan oceanic island arc system became continental island arc with continued subduction of the oceanic floor that eventually became sutured to the eastern margin of the Asian plate as a part of the Afghan block (Tapponnier et al., 1981). The Kandahar and Chagai-Ras Koh arc systems are important to understand the crustal growth of the Afghan block, which represents the southeastern part of the Asian plate,

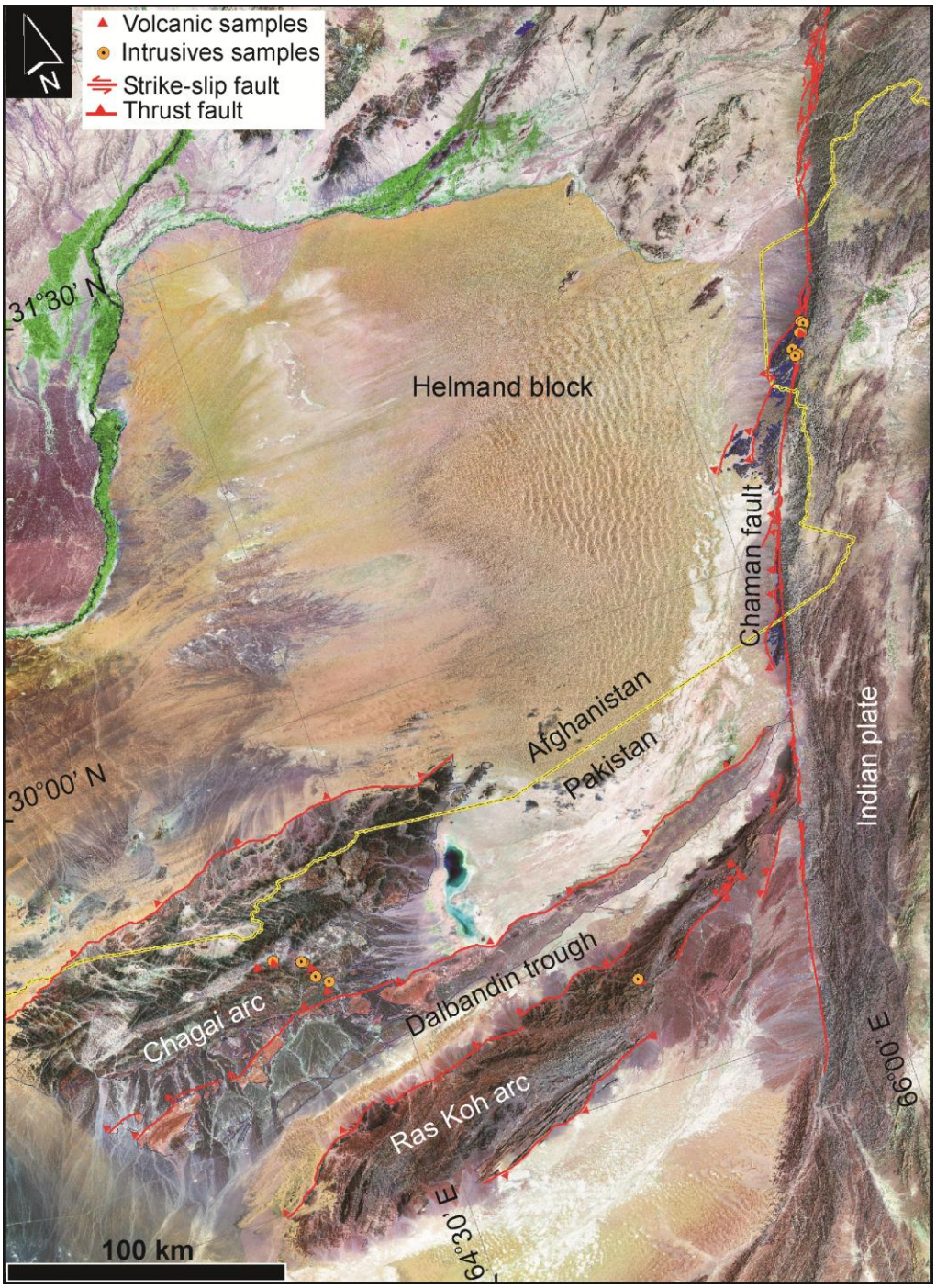

Figure 2.1: Locations of samples and configuration of the Chagai-Ras Koh arc and its relationship to the crystalline complex of the Khwaja Amran-Spinatizha areas. Nicolson et al. (2010) and Siddiqui et al. (2005) limit the arc system to just north of the Pakistan-Afghanistan border (yellow border line). Slivers of the arc related rocks present just west of the Chaman fault in Khwaja Amran and Spinatizha area could be a part of arc system that initiated sometime during Cretaceous.

and for determining the timing of collision of the Indian plate with the Asian plate along the western Indian plate boundary.

This chapter presents major and trace elements geochemistry and U-Pb age dating of volcanic and plutonic rocks from Chagai-Ros Koh arc system and Khwaja Amran-Spinatizha Crystalline Complex.

2.3. Tectonic setup

A detailed synthesis of the tectonic evolution of the western collision zone is provided by Treloar and Izatt (1993) who showed that subduction-related magmatism continued in Kohistan-East Nuristan arcs in the northwest and Chagai-Ras Koh arc in the southeast during the Cretaceous through Paleocene. In the Helmand block magmatism stopped during Late Cretaceous (Treloar and Izatt, 1993) and is marked by the emplacement of calc-alkaline diorites-granites (Debon et al., 1987). Similar intrusive rocks are reported from the Cretaceous part of the Chagai-Ras Koh arc system (Hunting Survey Corporation Limited, 1960; Nagell, 1975). In addition, Breitzman et al. (1983) reported two separate magmatic events at ~ 35 Ma and ~ 20 Ma that contradicted a continuous Paleocene calc-alkaline intrusion within Kandahar and Chagai-Ras Koh arcs. Sillitoe (1978) mapped the crystalline rocks exposed west of the Chaman fault along the Pakistan-Afghanistan border predicting a continuous arc volcanic chain that prevailed over the region prior to collision. Lawrence et al. (1981) provided preliminary geochemical data of the crystalline rocks exposed along the northern segment of the Chaman fault in Pakistan and concluded

that the andesitc/basaltic rocks of the Spinatizha area may be a sliver of the present day Chagai-Ras Koh arc that continued northward as the Kandahar arc. These slivers are common on the western side of the Chaman fault and are exhumed as small transpressional slabs along the fault due to the presence of gentle bends in the strike of the Chaman fault (Ruleman et al., 2007; Ul-Hadi et al.(in revision).

2.4. Petrography, geochemistry, and U-Pb dating

2.4.1. Analytical methods

Twenty seven samples were analyzed including ten samples from Chagai area, six from Ras Koh area, and eleven from Khwaja Amran-Spinatizha Crystalline Complex. Samples locations are shown in Figure 2.1. Samples were collected from fresh surfaces avoiding any surface alterations and leaching (Figure 2.2). Arc volcanic rocks (andesites to basalts) and later stage intrusions (diorites to granites) were collected for geochemical analysis. A rock saw was used to cut slides of rock from each sample for thin sections preparation for petrographic studies and to obtain fresh rock for geochemical analysis. Sample surfaces were washed and scrubbed using aluminum oxide powder to remove any residue from the saw blades. The samples for geochemical analysis were then crushed for mineral separation of zircons and pulverized for measuring major and trace elements.

Major and trace elements analysis were carried out at the Inductively Coupled Plasma-Mass Spectrometer (ICP-MS) Laboratory at the University of Houston, which is equipped with the Varian 810 ICP-MS. Major element analysis of the samples KA-4 to

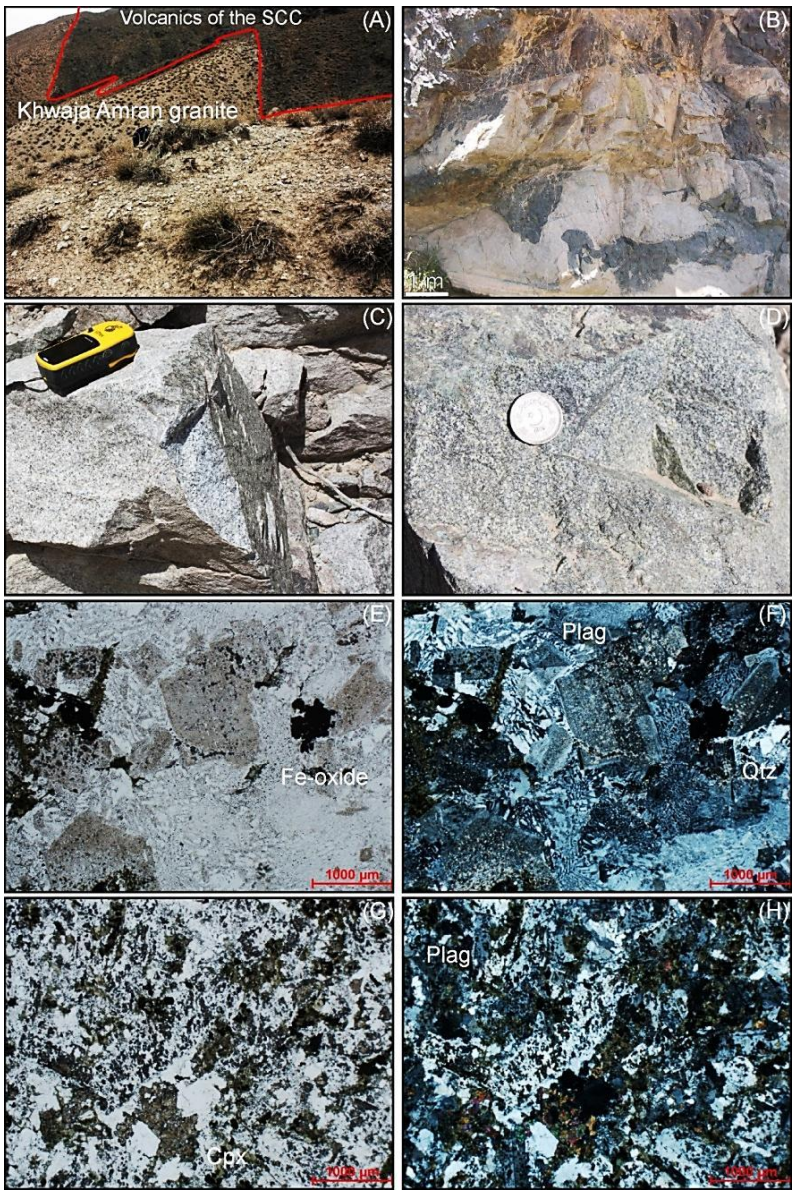

Figure 2.2: Petrology of selected rocks in the study area. (A) Nonconformable contact between granitic intrusion and the andesitic basalts of the Spinatizha crystalline complex. (B) Xenoliths of basalts within the dioritic intrusions in the Chagai area are common. Examples of granodiorites (C) and andesites (D) that were sampled. Photomicrographs of a granodiorite sample in plane-polarized (E) and cross-polarized light (F). The euhedral to sub-euhedral plagioclase and feldspars show a granular texture with no post-crystallization alterations. Perthitic texture is common in these rocks but rare in more acidic rocks of the suite. Photomicrographs of an andesitic sample from Spinatizha Crystalline Complex in plane-polarized (G) and cross-polarized light (H). Coarse zoned plagioclase grains are embedded in cryptocrystalline groundmass of clinopyroxene. Rare alterations on plagioclase and pyroxene to chlorites can be seen in thin sections.

KA-7 and ST-1 and 2 were conducted at the Geochemistry Laboratory of Ellington & Associates, Inc. Houston using X-Ray Fluoresce (XRF).

Sample digestion for major elements was done at ~ 1125 °C utilizing ~ 200 mg of finely ashed portion of sample. The lithium metaborate mixed sample beads were dissolved in 100 ml of 1.5N HNO_3 with Tri-X added to prepare the final solution for ICP-MS analysis. Oxides including SiO_2, Al_2O_3, FeO, CaO, Na_2O, K_2O, MgO, MnO, TiO_2, and P_2O_5 were measured with three methods BASME04, BASME05 and UMNAKP. Selective two USGS standard samples from a list including AGV-2, BCR-Rice, BHVO-2, BIR-1, DNC-1, JB-2, and W-2 were run after every set of five analyses ensuring a relative standard deviation (RSD) range of 5-10%. Measured variation of the same element between different methods was less than 5%. Major element analysis for the six samples from Khawaja Amran-Spinatizha area were carried out with XRF alongside three standards (SCO-1-3, Slate-1 and Slate-3) with a mean standard deviation of < 10%.

For trace element analysis 100 mg of powdered samples were digested in 16N HNO_3 and 24N HF at 180 °C along with USGS standards (NIM-G (granite) and BHVO-2 (basalt) and a blank. The final solution containing 2 wt % HNO_3 was spiked with 1 ml internal standard (1 ppm Li^6, Ni^{61}, Sr^{84}, Rh^{103}, In^{115}, Nd^{145}, Tm^{169}, Re^{187}, $Bi^{209}$with a final internal standard concentration of 10 ppb). Trace elements Li, Be, Sc, Ti, V, Cr, Co, Ni, Cu, Zn, Ga, Rb, Sr, Y, Zr, Nb, Sn, Cs, Ba, La, Ce, Pr, Nd, Sm, Eu, Tb, Gd, Dy, Ho, Er, Tm, Yb, Lu, Hf, Ta, Pb, Th, U were measured. Standard samples were analyzed after every three

sample analysis to avoid any instrumental drift or background accumulation. Data reduction with and without oxides confirmed a relative standard deviation in the range of 3-5%. The geochemical data for all the samples is provided in Table 2.1 and presented in Figures 2.3, 2.4, 2.5, and 2.6.

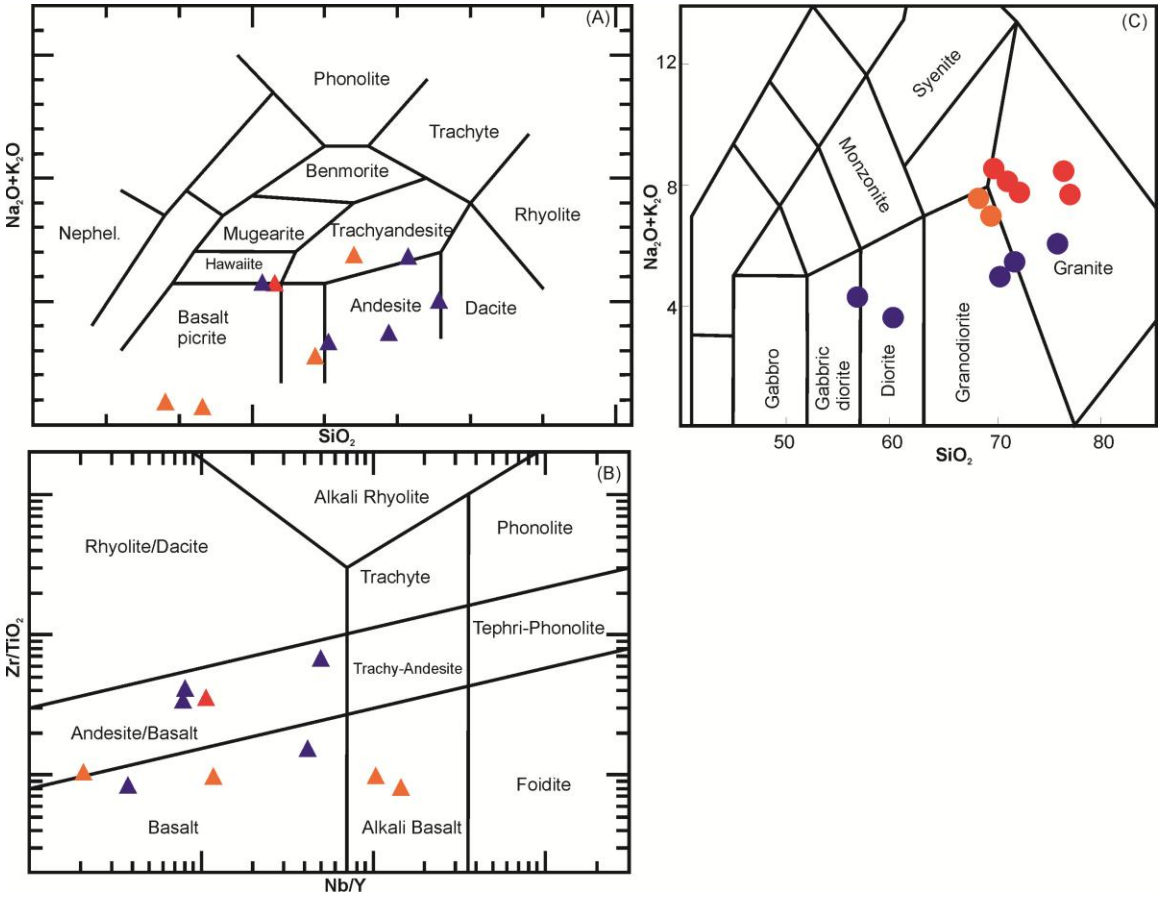

Figure 2.3: Classification diagrams for the analyzed volcanic and granitic rocks of the Chagai (blue), Ras Koh (orange) and Khwaja Amran (red) arc systems. Boundaries are (A) Cox et al. (1979), (B) Pearce (1996), and (C) Middlemost (1985).

Table 2.1: Major and trace elements data of all the samples analyzed.

Sample#	Ch-2	Ch-5	Ch-6	Ch-7	Ch-9	Ch-10	Ch-12	Ch-13	C-15	RK-1	RK-4	RK-6	RK-19	KA-1	KA-2	KA-3	KA-4	KA-5	KA-6	KA-7	ST-1	ST-2	ST-3	ST-4
SiO_2	50.8	69.4	58.8	62.7	74.5	55.0	70.3	55.3	60.7	57.0	68.0	67.2	54.4	-	-	-	63.5	59.9	62.3	51.6	65.9	66.5	-	-
TiO_2	1.36	0.43	0.80	0.96	0.29	0.68	0.35	1.10	0.51	1.26	0.65	0.36	0.62	-	-	-	0.45	0.42	0.48	0.91	0.25	0.17	-	-
$Al2O_3$	16.0	14.2	16.4	17.9	14.0	17.2	14.4	16.7	16.3	15.8	14.4	16.4	17.0	-	-	-	11.4	11.6	11.3	11.2	10.7	11.1	-	-
$Fe2O_3$	13.1	3.99	8.18	7.48	2.15	8.23	3.31	11.2	5.71	11.0	5.14	3.88	9.86	-	-	-	3.61	3.12	3.72	8.54	1.48	0.84	-	-
MnO	0.10	0.08	0.16	0.09	0.07	0.14	0.07	0.39	0.12	0.16	0.09	0.11	0.17	-	-	-	0.07	0.06	0.08	0.13	0.04	0.03	-	-
MgO	5.51	1.20	3.26	3.25	0.09	3.50	1.04	4.90	4.05	3.78	1.46	0.87	4.56	-	-	-	0.65	1.09	0.75	2.72	0.14	0.10	-	-
CaO	7.55	4.43	6.62	1.32	2.14	8.10	3.44	7.24	5.52	5.16	1.41	2.24	8.24	-	-	-	1.94	2.18	2.04	5.44	0.73	1.01	-	-
Na_2O	5.33	3.45	2.97	0.73	3.25	3.26	3.38	2.93	3.77	5.66	6.06	6.00	2.56	-	-	-	3.94	3.83	3.97	4.12	3.77	3.70	-	-
K_2O	0.34	1.49	1.02	3.97	2.70	0.92	1.98	0.28	2.94	1.08	0.83	1.42	0.09	-	-	-	3.25	3.38	3.21	1.49	3.50	2.98	-	-
P_2O_5	-	-	-	-	-	-	-	-	-	-	-	-	-	-	-	-	0.10	0.12	0.11	0.32	0.03	0.02	-	-
Sr	238.0	234.1	251.5	1016	123.6	110.9	298.7	302.8	264.4	164.5	190.0	202.1	126.8	418.9	183.8	578.8	136.1	151.2	156.4	293.8	42.5	89.4	434.1	342.6
Ba	147.8	146.2	215.6	33.1	278.3	53.6	552.3	552.5	221.1	136.3	154.6	158.5	40.8	212.0	141.5	519.3	402.9	415.8	481.7	184.1	509.5	340	216.3	336.2
Li	2.1	2.0	9.5	15.4	7.7	16.3	11.2	11.8	9.5	7.9	2.4	2.4	10.1	7.9	7.4	4.3	14.0	11.8	14.3	20.0	5.0	1.6	8.0	7.4
Be	0.5	0.4	0.5	0.3	1.2	0.9	1.1	1.1	0.5	0.5	1.0	1.0	0.2	0.8	0.5	1.1	1.5	1.4	1.5	1.1	1.4	1.5	0.7	0.5
Rb	11.7	11.5	32.4	3.3	5.9	2.4	21.6	23.7	34.0	17.3	14.3	15.2	5.0	27.7	21.1	37.3	67.4	60.6	54.7	25.9	101.6	85.4	28.2	23.6
Y	32.1	31.6	25.7	9.2	19.5	24.4	10.0	10.2	26.8	21.7	34.6	36.5	16.3	30.1	17.5	8.6	33.6	32.9	38.1	39.5	19.5	15.8	30.9	19.7
Zr	67.6	66.5	118.5	32.2	128.3	163.7	102.2	100.5	123.4	71.9	136.6	143.6	38.4	120.3	46.7	69.2	189.4	165.3	257.7	189.8	75.2	64.5	124.1	70.1
Nb	1.2	1.2	2.1	4.1	18.6	24.8	4.3	4.2	2.2	2.5	4.6	4.8	0.3	9.0	1.2	5.2	8.6	5.8	7.9	4.2	6.9	5.1	9.1	1.3
Mo	0.3	-	0.2	-	-	-	0.1	0.1	-	-	0.4	-	0.2	9.0	1.2	5.2	1.4	0.2	1.7	0.6	1.8	1.1	9.1	1.3
Cs	1.1	1.1	9.4	0.3	0.1	0.1	2.1	2.0	9.7	2.5	0.4	0.4	0.2	0.9	2.9	1.7	1.3	1.1	1.1	1.3	3.1	1.9	0.9	3.4
La	2.9	2.9	8.9	11.2	13.3	19.6	23.3	22.2	9.1	5.4	14.3	14.7	1.2	11.2	2.6	16.3	11.2	10.4	22.7	18.3	23.0	10.7	11.4	6.4
Ce	8.0	7.9	19.0	21.1	30.6	43.9	30.6	30.5	19.5	13.2	30.4	31.3	3.9	27.6	6.7	29.9	22.9	22.7	48.5	39.8	33.8	18.5	28.3	14.6
Pr	1.5	1.5	3.0	2.1	4.6	6.8	4.1	3.9	3.1	1.8	4.2	4.3	0.8	4.0	1.0	3.2	3.2	3.3	6.3	5.6	4.4	2.0	4.1	2.0

Table 2.1 continues on next page.

Table 2.1 continued.

Sample#	Ch-2	Ch-5	Ch-6	Ch-7	Ch-9	Ch-10	Ch-12	Ch-13	C-15	RK-1	RK-4	RK-6	RK-19	KA-1	KA-2	KA-3	KA-4	KA-5	KA-6	KA-7	ST-1	ST-2	ST-3	ST-4
Nd	9.3	9.2	14.2	7.8	18.9	30.4	14.8	13.6	14.2	8.4	18.9	18.8	4.6	19.1	4.9	11.3	13.9	14.6	25.0	23.8	14.7	6.7	19.5	9.0
Sm	3.4	3.3	3.6	1.8	4.5	6.2	2.4	2.3	3.6	2.5	4.6	4.5	1.6	5.3	1.7	2.0	3.6	3.8	5.5	5.9	2.8	1.4	5.4	2.5
Eu	1.1	1.1	1.0	1.1	1.4	2.2	0.6	0.6	1.0	0.9	1.3	1.3	0.6	1.9	0.7	0.7	1.1	1.1	1.2	1.8	0.4	0.3	1.9	0.9
Gd	4.9	4.9	4.2	1.8	4.7	6.4	2.0	2.0	4.3	3.3	5.3	5.3	2.3	5.8	2.2	1.9	4.1	4.2	5.6	6.2	2.7	1.6	5.9	2.9
Dy	6.1	6.1	4.8	2.0	4.4	5.8	1.8	1.8	4.8	4.0	6.0	6.0	3.4	6.1	2.8	1.3	4.9	5.0	5.9	6.5	2.9	2.1	6.2	5.6
Ho	1.3	1.3	1.0	0.3	0.8	1.1	0.4	0.3	1.0	0.8	1.3	1.3	0.7	1.1	0.6	0.3	1.1	1.1	1.3	1.4	0.6	0.5	1.2	0.7
Yb	3.4	3.4	2.9	0.7	1.7	2.1	1.1	1.1	2.9	2.5	3.5	3.5	2.2	2.7	2.0	0.9	3.6	3.6	4.1	4.1	2.4	1.8	2.7	2.3
Lu	0.5	0.5	0.4	0.1	0.2	0.3	0.2	0.2	0.4	0.3	0.5	0.5	0.3	0.4	0.3	0.1	0.5	0.5	0.6	0.6	0.4	0.3	0.4	0.3
Hf	2.1	2.0	3.2	0.9	2.9	4.1	3.0	3.0	3.2	2.0	3.7	3.6	1.2	3.3	1.4	1.9	4.9	4.5	6.4	4.6	2.4	2.0	3.3	2.0
Ta	0.1	0.1	0.1	0.2	1.0	1.5	0.3	0.3	0.1	0.2	0.3	0.3	0.0	-	-	-	0.5	0.9	1.0	0.6	0.6	0.8	-	-
Pb	2.0	1.9	6.7	7.1	1.4	1.3	5.7	5.7	6.8	28.9	3.8	3.7	1.4	1.0	1.7	7.0	8.8	5.0	12.7	7.3	14.5	7.9	1.0	8.7
Th	0.7	0.7	2.8	1.3	0.9	1.0	15.6	15.7	2.7	1.6	4.5	4.5	0.1	0.9	0.4	5.8	6.8	7.9	8.2	3.7	9.0	10.8	0.9	2.4
U	0.2	0.2	0.7	0.4	0.3	0.3	3.3	3.4	0.7	0.3	0.9	0.9	0.1	0.2	0.2	1.7	1.7	1.5	2.0	0.9	1.4	1.3	0.2	0.7
Sc	45.7	45.2	21.0	3.0	26.0	32.4	16.7	16.7	21.0	22.6	15.5	15.5	32.6	45.1	42.4	6.9	7.7	6.7	7.7	22.4	2.4	2.9	45.4	26.0
Ti	7791	7706	4848	980	11649	15194	1991	2038	4863	7136	3788	3798	3415	14018	3934	1890	3203	2850	3255	6621	1082	867	14290	3818
V	426.8	422.1	187.4	12.8	250.1	328.2	70.5	69.6	188.0	356.5	16.2	16.2	253.4	414.6	327.1	63.1	35.9	38.1	43.4	149.8	6.0	5.8	417.6	225.0
Cr	19.5	17.6	20.9	13.3	187.0	250.8	17.0	17.8	19.3	2.8	2.7	0.9	15.0	308.9	13.2	-1.1	27.8	-10.1	35.0	5.3	8.8	11.2	313.1	41.0
Co	31.4	31.0	22.2	2.1	41.7	63.9	8.2	7.9	22.3	29.7	5.1	5.1	26.7	53.5	35.7	7.8	4.5	45.2	25.9	48.1	0.9	19.1	53.0	28.3
Ni	19.1	18.1	14.2	6.2	119.8	119.9	13.4	13.3	13.4	5.7	0.8	-	9.0	101.9	14.3	7.0	8.0	-0.3	7.9	56.6	5.2	11.0	103.2	33.0
Cu	7.1	6.7	67.7	17.9	18.2	200.4	6.7	6.6	68.8	57.3	16.6	16.9	32.5	59.2	167.5	15.2	9.4	4.4	26.7	37.6	68.5	1.9	59.4	121.9
Zn	18.4	17.7	67.9	18.0	90.2	114.2	23.5	23.1	69.1	93.1	62.9	65.0	77.4	85.7	64.2	37.4	31.6	83.5	24.9	47.5	118.6	5.8	86.5	66.2
Ga	19.0	18.8	16.6	1.9	19.5	18.8	15.2	15.3	17.1	17.0	15.9	17.0	15.9	24.6	15.3	17.1	15.8	14.9	14.6	18.5	12.4	11.4	24.8	17.1

Out of six samples from Khwaja Amran-Spinatizha area including two granites, three granodiorites, and one andesite, only the granites and one granodiorite samples produced enough zircon grains for U-Pb dating. Mounted single-grain zircons were measured using Laser Ablation-ICP-MS. The ICP-MS is coupled with a Photon Machines Analyte 193 nm wavelength laser ablation system. Analyzed raw data (signal intensities) of ^{202}Hg, ^{204}Pb(Hg), ^{206}Pb,^{207}Pb, ^{208}Pb, ^{232}Th, and ^{238}U was imported into Wavemetrics Igor Pro™ (v. 6.12A) with an add-in module Iolite (v. 2.11) (Hellstrom et al., 2008) to select baseline (~15 s) and sample signals (~20 s) for each analysis. The baseline-subtracted mean sample signal intensities and 2 standard error uncertainties were exported as a comma delimited values file. Sample data was imported into a data reduction spreadsheet and corrected for instrumental mass and elemental fractionation to calculate random and systematic errors in addition to the internal errors exported from Iolite.

The fractionation factor caused by instrumental drift is applied to the each sample measured at any particular analytical session. The standard error of at least two standards run before and after the sample is calculated to estimate an uncertainty in the fractionation factor correction and add those errors quadratically to the internal errors exported from Iolite. Correlated errors are calculated with the equations given by Ludwig (1980) and IsoPlot (v. 3.50) is used to construct concordia diagrams (Ludwig, 2003). Isoplot assigned U decay constants are included in the concordia diagram. Common Pb corrections were made following the methods provided by Shaulis et al. (2010).

2.4.2. Petrography, major element geochemistry, and classification

Greenschist facies metamorphism is reported from the rocks of Khwaja Amran-Spinatizha Crystalline Complex (Lawrence et al. 1981) and the Chagai-Ras Koh area (Siddiqui, 2004). In Khawaja Amran-Spintizha area the impact of shearing along the Chaman fault is only evident in the meta-sedimentary rocks of the Spinatizha metamorphic complex of Lawrence et al. (1981). However, volcanic rocks that are intruded by late stage granitoids have only chilled margins and in the outcrops these rocks stand undeformed (Figure 2.2 A to D). In thin sections all the rock types have typical igneous textures with no or very minute alterations (Figure 2.2 E and F).

The Khwaja Amran-Spinatizha rocks include granodiorite, diorite, dacite, basalt, and andesite (Figure 2.3 A). The volcanic suite is intruded by the more felsic stocks of granodioritic-granitic rocks (Figure 2.2 A). These intrusive plutons have sharp contacts with the Spinatizha metamorphic complex and the volcanic rocks. Petrographically, the granites and granodiorites have no observed secondary mineralization or alterations, and are characterized by euhedral quartz and alkali-feldspar grains, and are coarse grained with hypideomorphic to granular textures (Figure 2.2 E and F). The volcanic rocks are mainly andesitic in composition as tuffs and agglomerates. The andesites have a porphyritc texture with large plagioclase grains surrounded by a groundmass of dominantly clinopyroxene. In contrast to the intrusive rocks, the volcanics are slightly altered, with plagioclase and mafic minerals replaced by chlorite and epidote.

The Chagai-Ras Koh area rocks are dominantly andesites, trachy-andesites, and basalts grading to more felsic suites of dacites with intrusions of a series of rocks ranging from granite through granodiorites to diorites (Figure 2.3). Breitzman et al. (1983) named these intrusive rocks the Chagai Intrusives. The volcanic rocks are petrographically similar to those of Khwaja Amran-Spinatizha area with plagioclase phenocrysts within a clinopyroxene-rich groundmass. These volcanic rocks show more alterations as compared to the Khwaja Amran-Spinatizha area volcanic rocks but still preserve the original porphyritic textures.

The rocks of the Chagai-Ras Koh area are more enriched with alumina as compared to that of the Khwaja Amran-Spinatizha area, while they have similar concentrations of Ti except for the two diorite samples of the Ras Koh (Figure 2.4). This pattern is also evident for Ca and Mg concentrations with increasing Zr. However, rocks of the Chagai-Ras Koh are more depleted in K in contrast to the rock of the Khwaja Amran-Spinatizha area. This may be due to the difference in the degree of alteration of the two suites. The samples that lie in the same window of K concentration as those of Khwaja Amran-Spinatizha area are the dacites/granodiorites. Overall rocks of the Khwaja Amran-Spinatizha area are depleted in Al_2O_3, CaO, MgO and Fe_2O_3 except for the volcanic rocks that resemble a more fractionated portion of the source and earlier crystallization of plagioclase, pyroxene, and hornblende.

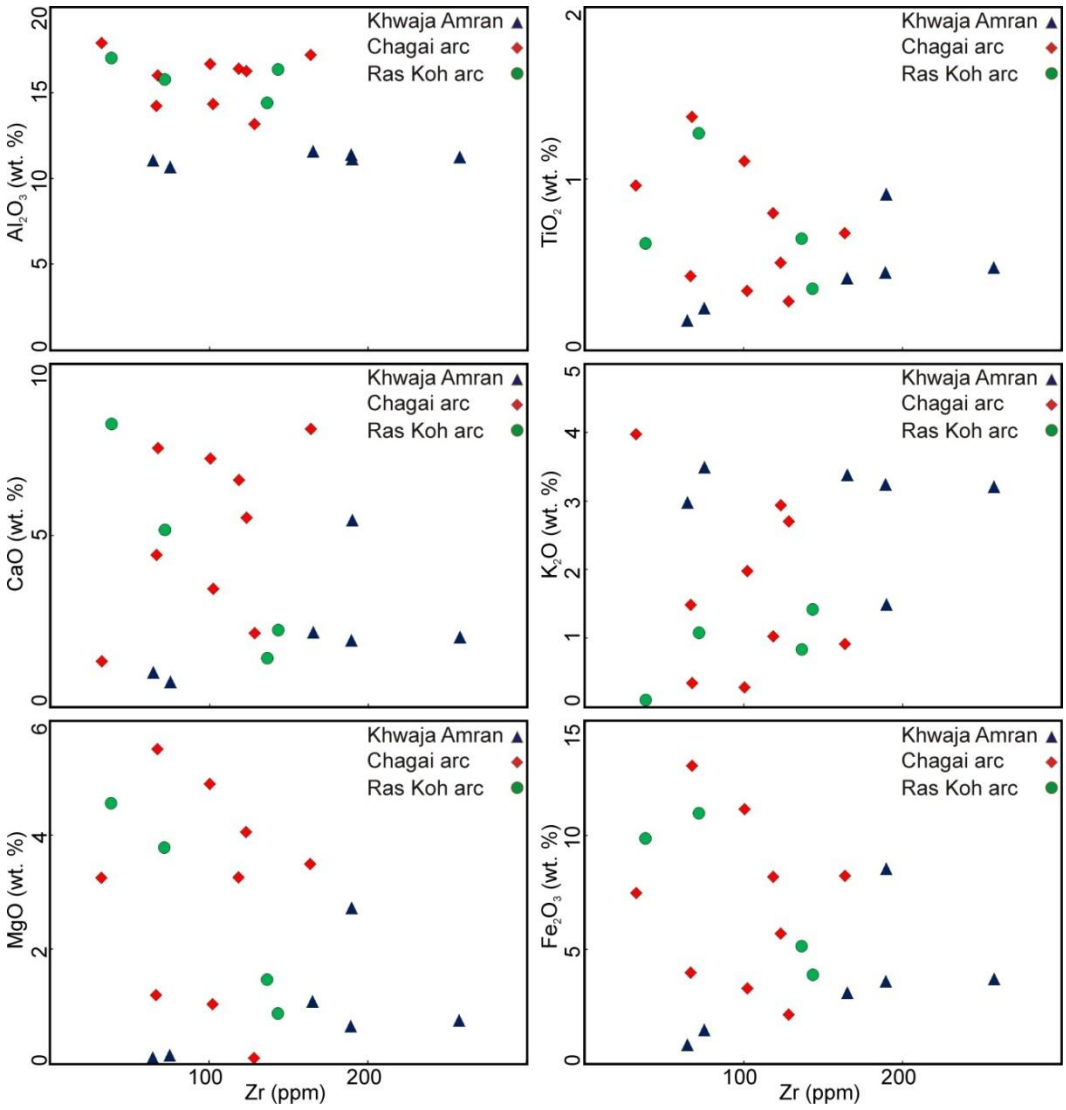

Figure 2.4: Binary plots of major elements versus Zr (ppm) in samples from Chagai (diamonds), Ras Koh (circles) and Khwaja Amran (triangles) areas.

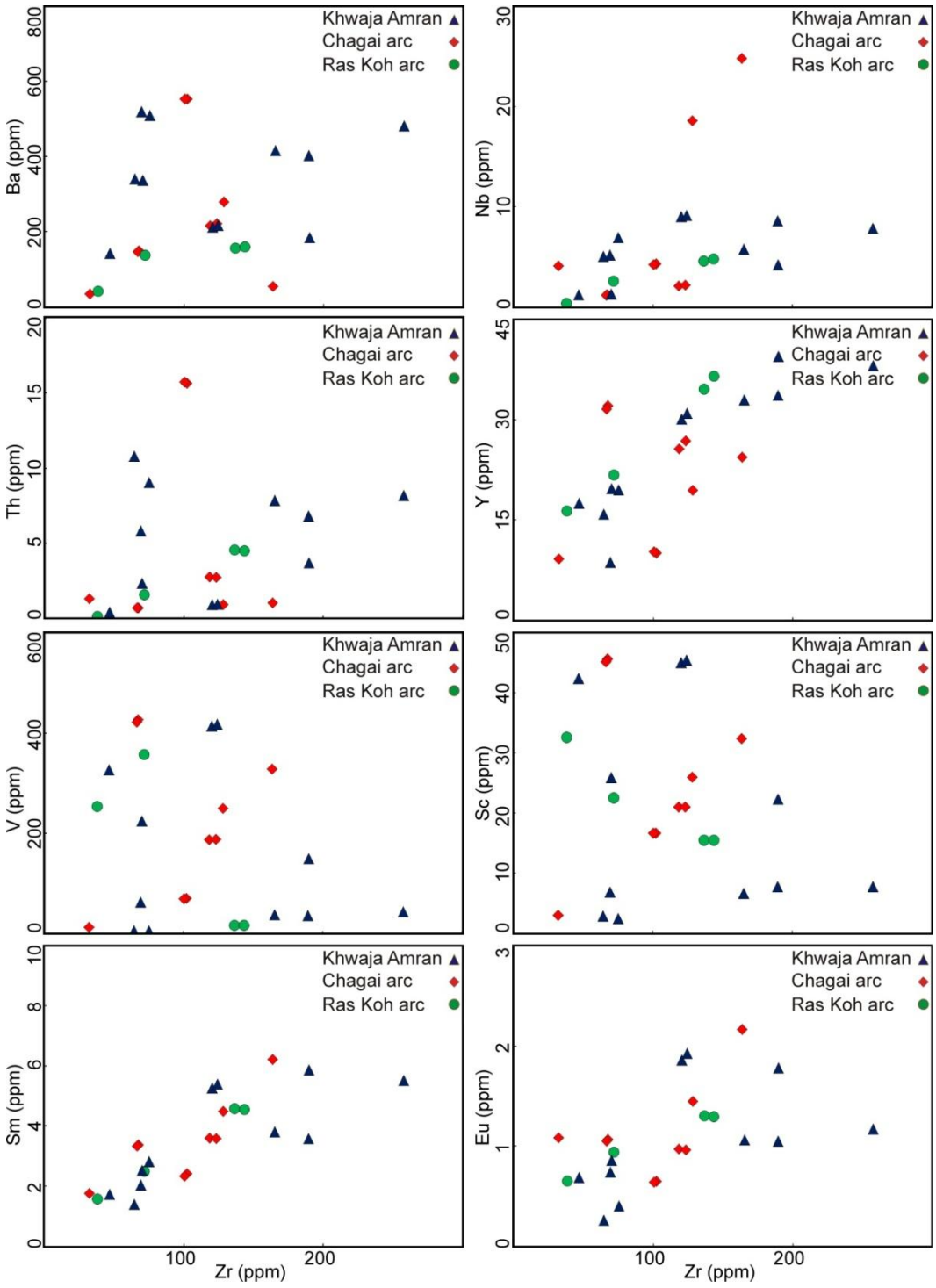

Figure 2.5: Binary plots of trace elements versus Zr (ppm) in samples from Chagai (diamonds), Ras Koh (circles) and Khwaja Amran (triangles).

2.4.3. Trace element geochemistry

To avoid mobile Na and K in classifying the rocks of the three complexes, Nb/Y versus Zr/TiO_2 classification diagram were used (Pearce, 1996; Figure 2.3 B). All the rocks cluster within and around the field of andesite-basalt. This is in accordance with the earlier studies for the Khwaja Amran-Spinatizha (Lawrence et al., 1981) and Chagai-Ras Koh areas (Hunting Survey Corporation Limited, 1960; Siddiqui, 2004). Trace elements plotted against Zr exhibits a positive correlation with increasing Zr except for V and Sc (Figure 2.5). This behavior may reflect alteration in some of the samples but may also be the result of partitioning into mineral phases.

Spider diagram (Figure 2.6 A) shows that large ion lithophile elements (LILE) excluding Cs have values 20-30 times more than that for the N-MORB. Cs values are at the range of 300 while Sr is in the range of 2-4 times the N-MORB; however Eu in some samples is < 1, which may be due to the plagioclase fractionation. In contrast to this, the high field strength elements (HFSE) have much lower normalized values with Nb and Ti having values ranging between < 1 to ~ 2. A similar pattern is shown by light rare earth elements (LREE) with N-MORB values of more than 30 for Ce and a range of 5-10 for La, Pr and Sm (except Eu, which is depleted) in contrast to the < 1 to 5 times N-MORB values for the heavy rare earth elements (HREE).

The intrusive rocks of all the three complexes show a very consistent trend. LILE ranges between 35-70 more than the N-MORB while Cs has values > 300 than the N-MORB. Sr

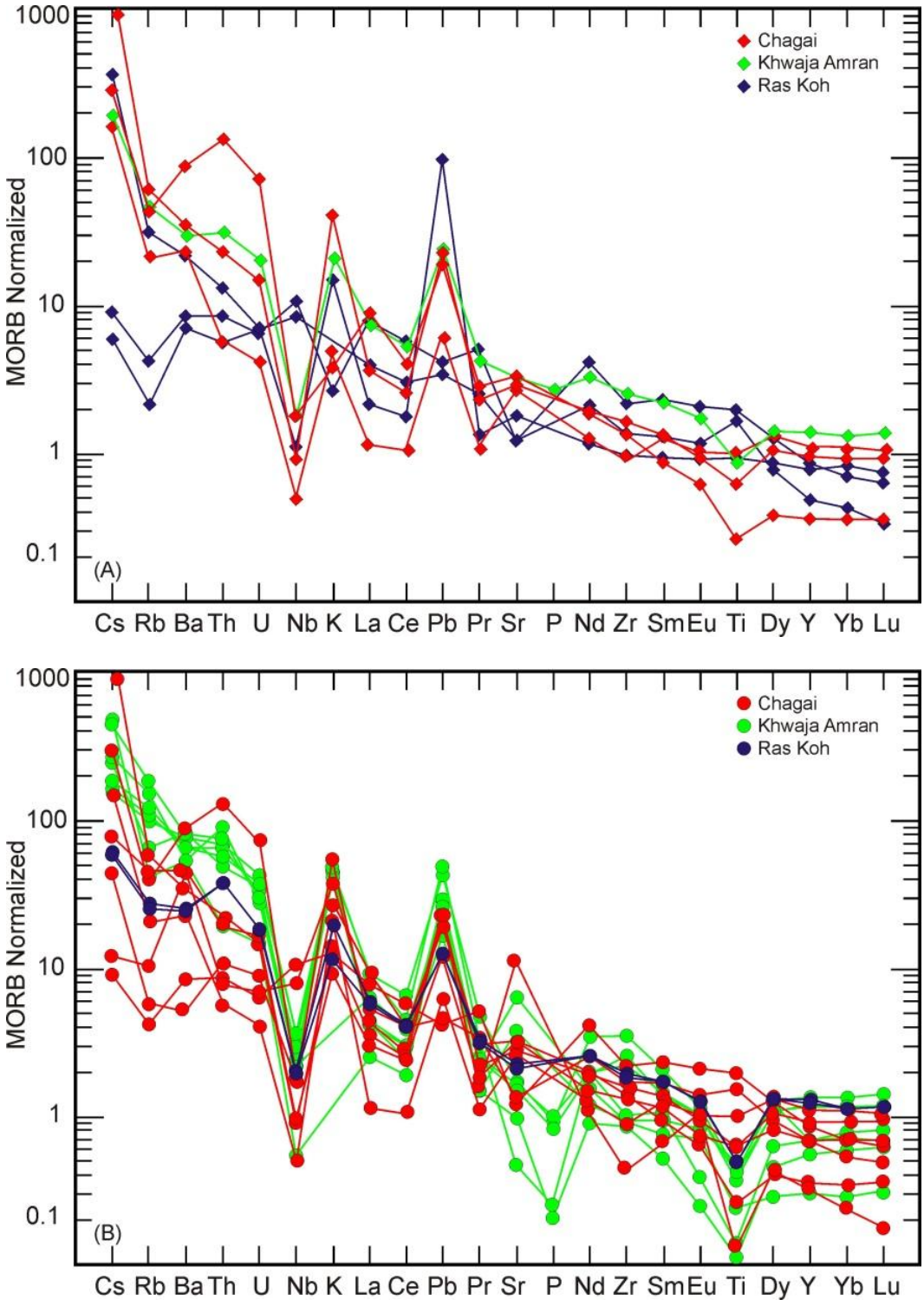

Figure 2.6: MORB normalized (after Sun and McDonough, 1989) spider diagrams of (A) volcanic rocks and (B) intrusive rocks of all the three crystalline complexes.

values range from 3 to 5, and Eu having negative values in some samples (Figure 2.6 B). The HFSE values range from 20 to 40 more than N-MORB with < 1 values for Ti and Y, and 1 to 3 more than N-MORB values for Nb. LREE show a positive correlation with respect to HREE except for the Sm and Eu, which range from < 1 to ~ 3. The Yb, Lu, Y, and Dy also range from < 1 to ~ 2. Higher K and HFSE values for all the three suites reflect highly fractionated source magma with crustal contaminations. Overall all the three complexes show enrichment of LILE with respect to HFSE, and enrichment of the LREE with respect to HREE.

2.4.4. The U–Pb zircon ages

Weighted average age for all U-Pb analysis of the individual samples (15 – 25 zircon grains from each sample) and age concordia diagram for all analyses based on $^{207}Pb/^{206}Pb$ vs. $^{238}U/^{206}Pb$ plots are shown in Figures 2.7, 2.8 and 2.9. No crystal inheritance was observed as the analyses are based on both cores and rims of the individual zircon grains. Single age for each sample is preferred with no later stage adjustments within the zircons either due to metamorphism or younger intrusions. These samples have no older ages and their age ellipsoids concentrate nicely along the Concordia. Furthermore, standards samples that were run along the individual zircon analyses have given standards' ages within less than 1% errors (Figure 2.10). Therefore these ages represent emplacement period of these rocks. The outliers in each sample reflect presence of the background Hg and hence the outliers were rejected while calculating the mean weighted ages. All analyzed data is shown in Table 2.2 and is filtered using techniques set forth by Shaulis et al. (2010).

The mean ages for samples ST-1 and ST-2 are 59.8 ± 1.1 Ma and 58.8 ± 1.2 Ma respectively and 66.1 ± 1.5 Ma for sample KA-4. The Spinatizha granites (ST-1 and ST-2) resemble the youngest phase of intrusion in the Khwaja Amran-Spinatizha Crystalline Complex. Therefore it is suggested that the average age of the intrusive rocks of the Khwaja-Amran Spinatizha Crystalline Complex ranges from ~ 59 to 62 Ma as is shown by the close clustering of ellipsoids around a single point on the Concordia (Figures 2.7, 2.8, and 2.9).

2.5. Discussion

It has been suggested that the Chagai-Ras Koh arc system represents an oceanic island arc that was built on the subducting Tethyan ocean floor and had matured to an Andean-type continental arc system as the Indian plate approached the Afghan block (Nicolson et al., 2010; Siddiqui, 2004); however the extent of this arc system is still debated (Shareq et al., 1977; Sillitoe, 1978; Arthurton et al., 1979; Farah et al. 1984; Siddiqui, 1996; Kazmi and Jan, 1997). The comparison of geochemical data from Chagai-Ras Koh with the Khwaja Amran-Spinatizha crystalline rock shows similarities and supports the hypothesis that rocks of the two areas may be genetically related. This is supported by the field evidences from this study and work of Lawrence et al. (1981) based on their field observations and stratigraphic positions of the different units. Tectono-magmatic discrimination diagrams (Figure 2.11) classify the rocks of Chagai-Ras Koh and Khwaja Amran-Spinatizha areas as of a syn-collisional arc system that transformed from a pure oceanic to continental arc system (Siddiqui, 2004). The oldest rock unit in the Chagai-

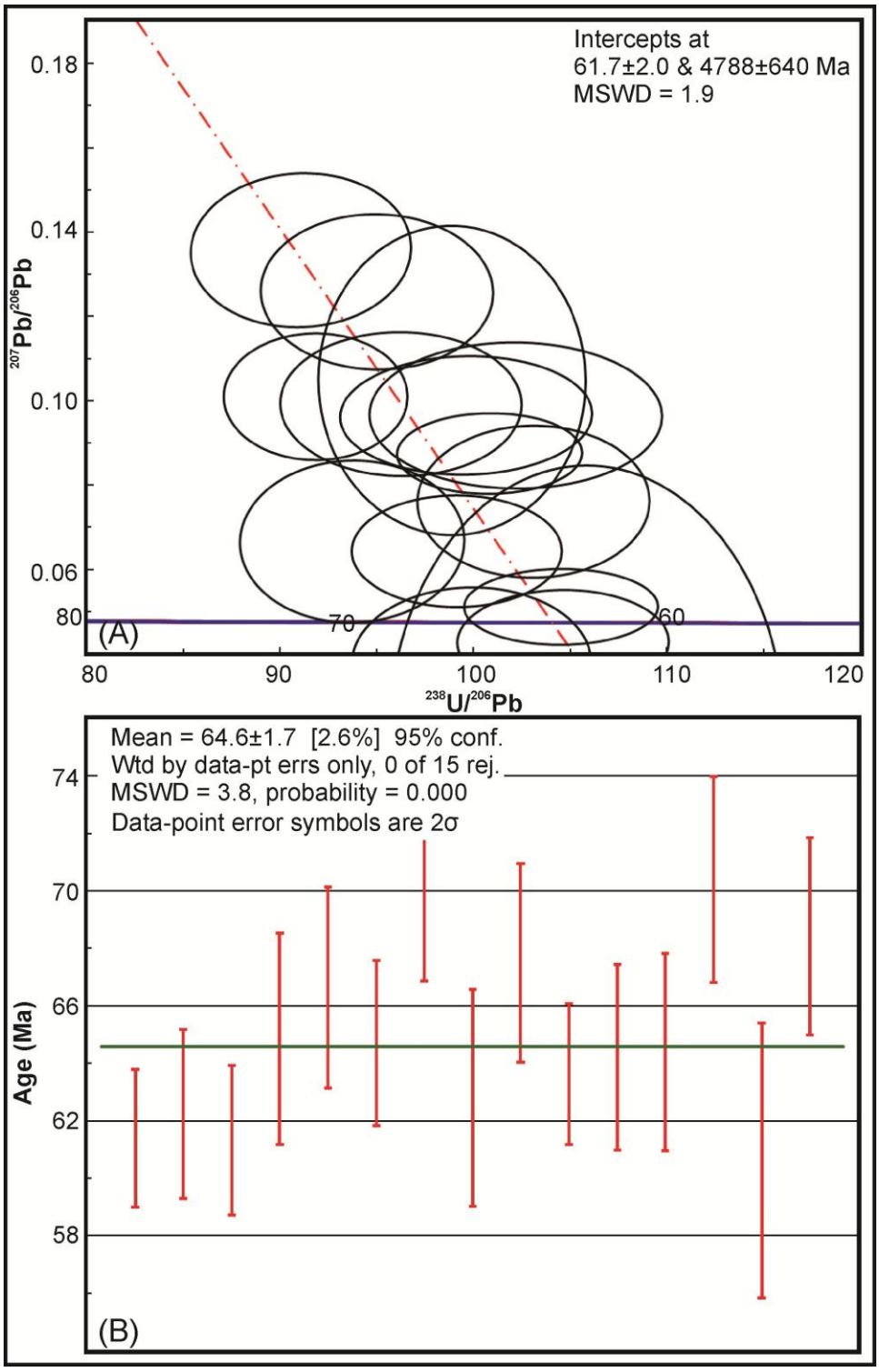

Figure 2.7: (A) Concordia, age probabilities and (B) weighted mean U–Pb age results for sample number KA-4.

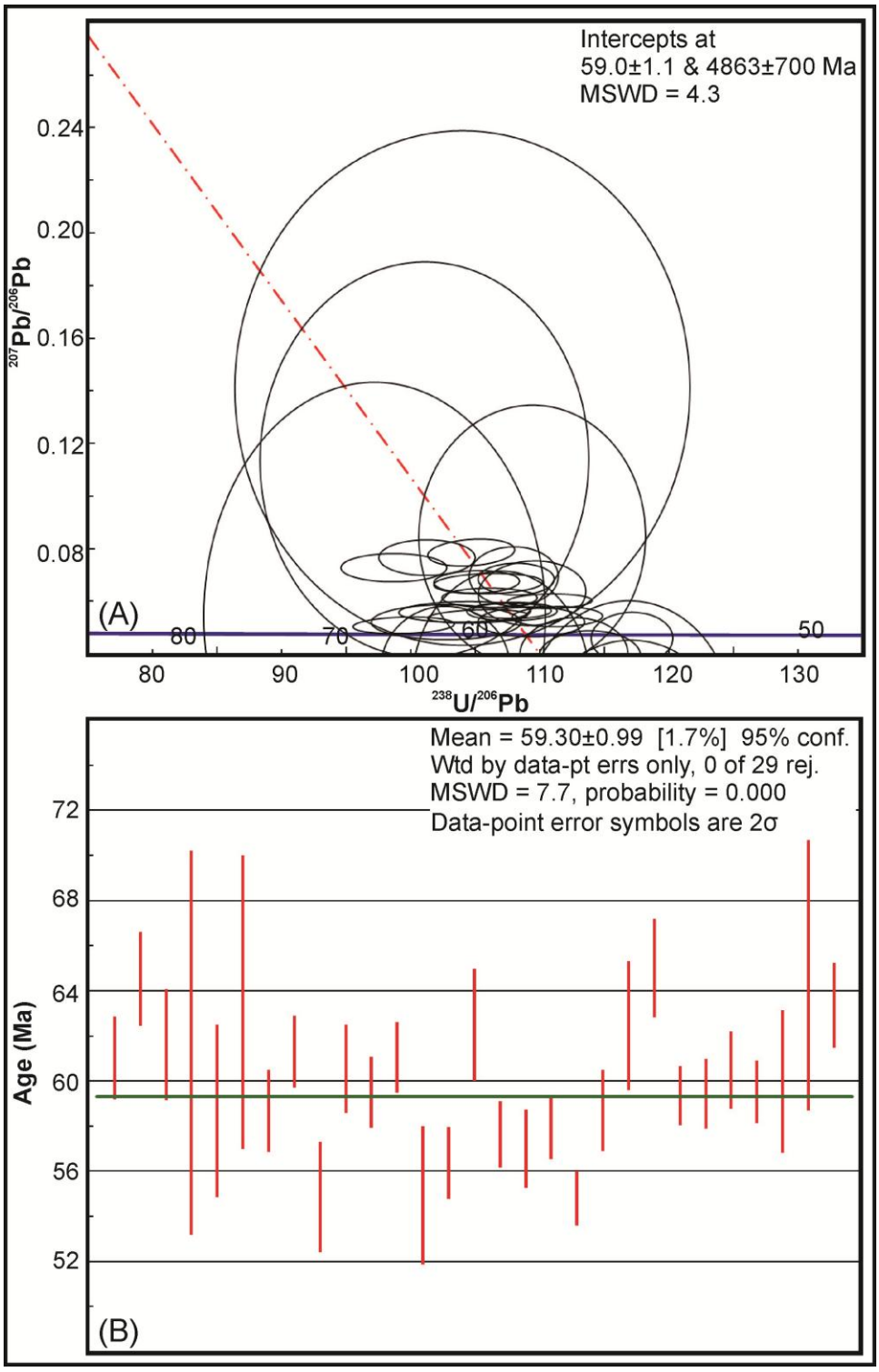

Figure 2.8: (A) Concordia, age probabilities and (B) weighted mean U–Pb age results for sample number ST-1.

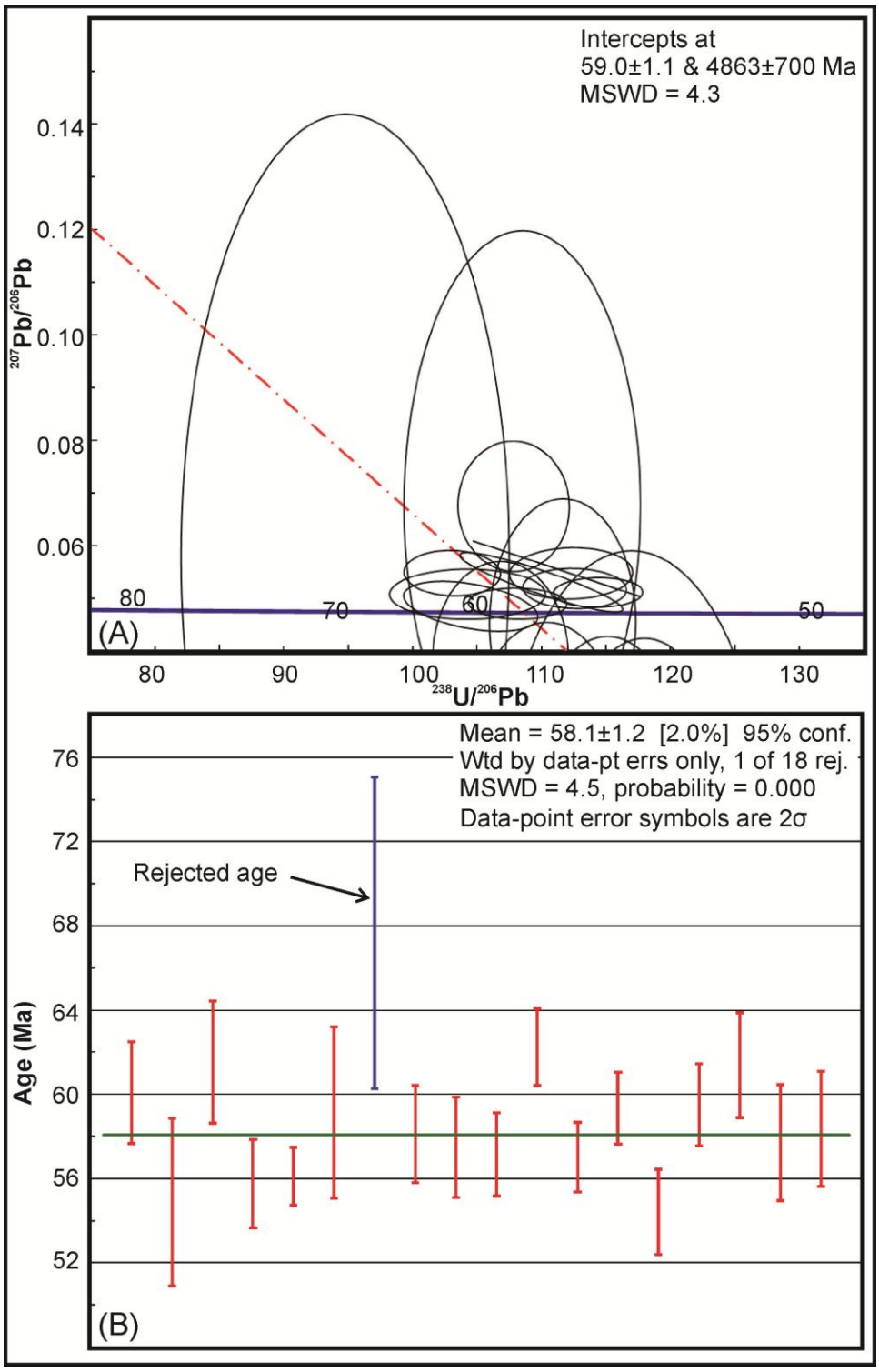

Figure 2.9: (A) Concordia, age probabilities and (A) weighted mean U–Pb age results for sample number ST-2. The ~ 59 Ma granites of ST-1 and ST-2 intrude the ~ 62 Ma dioritic to granodioritic suites of rocks.

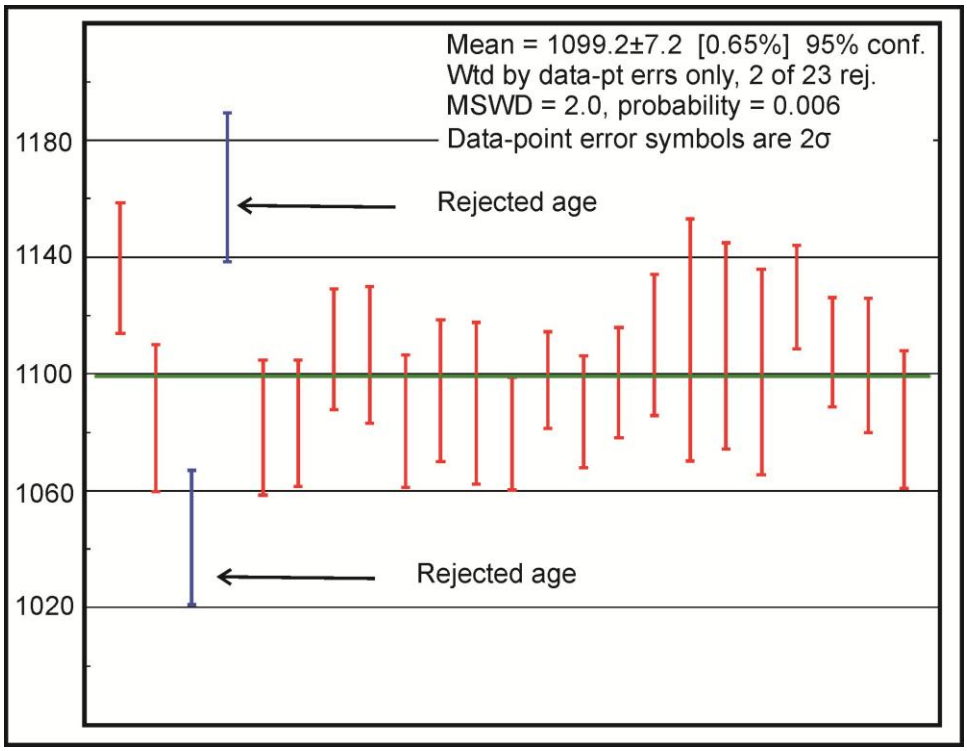

Figure 2.10: Weighted mean age of the standard FC5Z sample that was run as unknown. The analyzed samples have less than 1% analytical error.

Ras Koh is the well-classified Sinjirani-Kuchkki volcanic group (Hunting Survey Corporation Limited, 1960) which is dominantly composed of andesitic basalts and volcaniclastics, and can be correlated with the andesitic rocks of the Khwaja Amran-Spintaizha area; as been previously reported by Lawrence et al. (1981). The granitic rocks within the Cretaceous Sinjirani-Kuchakki group were previously reported to be of Late Cretaceous age (Hunting Survey Corporation Limited, 1960) based on the presence of the granitic pebbles in the Humai and Rakhshani Formations, which overlie the Sinjirani-Kuchakki group in Chagai-Ras Koh area. However, Breitzman et al. (1983) using fission-track dating of zircons and apatites from these intrusive rocks showed two separate episodes of magmatic activity at ~ 35 Ma and ~ 20 Ma within the Chagai-Ras

Koh arc system. U-Pb dating of the granitic rocks of the Khwaja Amran-Spinatizha area yields ~ 58–62 Ma age of emplacement. Since geochemical data suggest a probable common source for the intrusive rocks from both the areas, the U-Pb ages from the rocks in Khwaja Amran-Spintizha area may suggest that the intrusive rocks of Chagai-Ras Koh area are emplaced at the same time as that of the Khwaja Amran-Spintizha area.

Nicolson et al. (2010) suggested that volcanism in the Chagai-Ras Koh had already switched to Andean-type continental margin volcanism by the Late Cretaceous, implying the proximity of the Afghan block to the western Indian plate margin. Therefore by the time of emplacement of these intrusive rocks Indian plate was close to the eastern margin of the Asian plate (Afghan block). Emplacement of intrusive rocks in a compressional environment at comparatively shallower depths and over short durations is common in major arc systems (Miller et al., 2009), as would be the case for the Chagai-Ras Koh. This puts an upper limit of ~55 Ma for the timing of Indo-Asian collision in the north-west, which broadly coincides with ~ 50 Ma collision age reported from elsewhere in the Himalaya (Yin, 2006). However, if by 55 ma the collision was not initiated in the south as been evidenced by the sediments of the Katawaz basin (Carter et al., 2010) it was started in the north. Based on the deformation of the Katawaz basin sediments, Lawrence et al. (1992) estimated that the strike-slip movement along the Chaman fault started from ~25-20 Ma. These dates are consistent with the fission-track dating (Breitzman et al., 1983) of the events recorded by the intrusive rocks of the Chagai-Ras Koh system. The ~ 35 Ma event is the most probable timing of complete closure of the remnant of the Neo-

Tethys Ocean and the collision of the Indian plate with the Afghan block (Treloar and Izatt, 1993); whereas the ~20 Ma event might relate to the initiation of strike-slip movement along the Chaman fault.

Table 2.2: ^{204}Pb (common lead) corrected U-Pb ratios of the three analyzed samples and calculated ages.

Analysis #	Corrected isotope ratios					Corrected ages (Ma)					
	$^{207}Pb/^{235}U$	±2σ (%)	$^{206}Pb/^{238}U$	±2σ (%)	rho	$^{206}Pb/^{238}U$	± 2σ	$^{207}Pb/^{235}U$	± 2σ	$^{207}Pb/^{206}Pb$	± 2σ
Sample # KA – 4											
1	0.067	0.009	0.010	0.0004	-0.138	61.9	2.4	65.8	8.4	206.8	329.2
2	0.105	0.019	0.010	0.0005	0.085	63.5	2.9	101.2	17.6	1113.4	367.9
3	0.057	0.013	0.010	0.0004	0.405	62.5	2.6	56.7	12.9	-186.0	551.8
4	0.191	0.026	0.011	0.0005	0.523	68.7	2.9	177.6	21.9	2086.5	206.7
5	0.155	0.021	0.010	0.0006	0.162	67.0	3.5	146.0	18.4	1750.1	249.9
6	0.084	0.014	0.010	0.0005	0.045	65.7	2.9	82.0	12.8	584.7	362.0
7	0.155	0.017	0.011	0.0005	-0.053	71.5	2.9	146.5	14.9	1639.5	220.5
8	0.130	0.021	0.010	0.0006	0.252	64.2	3.7	124.4	18.5	1513.2	289.8
9	0.170	0.021	0.011	0.0006	0.266	69.2	3.5	159.7	17.8	1867.6	212.2
10	0.120	0.011	0.010	0.0004	0.357	64.0	2.5	115.1	10.4	1362.2	171.9
11	0.056	0.020	0.010	0.0005	-0.435	65.5	3.2	55.4	18.8	-366.1	966.7
12	0.137	0.014	0.010	0.0005	0.052	66.4	3.5	130.2	12.8	1540.4	215.3
13	0.205	0.025	0.011	0.0006	0.477	71.2	3.6	189.5	21.0	2148.1	186.6
14	0.142	0.016	0.011	0.0004	0.257	67.6	2.5	134.7	14.5	1575.2	208.1
15	0.106	0.020	0.011	0.0005	-0.404	71.2	3.5	101.8	18.5	891.0	444.8
18	0.381	0.034	0.012	0.0007	0.379	79.0	4.4	327.5	25.1	3004.6	137.5
19	0.190	0.019	0.010	0.0004	0.427	64.0	2.5	176.4	16.0	2198.1	154.9
20	0.077	0.008	0.010	0.0003	0.124	66.5	2.2	75.1	7.2	356.8	228.2
Sample # ST – 1											
1	0.070	0.002	0.010	0.0003	0.350	61.0	1.7	68.4	2.4	332.5	83.7
2	0.071	0.003	0.010	0.0003	0.184	64.5	2.1	69.9	3.1	256.1	117.5
3	0.075	0.004	0.010	0.0004	0.288	61.7	2.5	72.9	3.8	456.2	126.8
4	0.608	0.051	0.013	0.0006	0.645	86.1	4.1	482.1	32.2	3602.0	98.5
5	0.228	0.010	0.010	0.0003	0.274	65.4	2.0	208.0	8.4	2469.6	79.4
6	0.456	0.041	0.013	0.0006	0.659	81.0	3.6	380.8	28.6	3247.7	108.8
7	0.095	0.005	0.009	0.0003	0.234	59.8	1.7	92.2	4.2	1036.0	100.2
8	0.107	0.005	0.010	0.0003	0.325	61.5	1.6	102.8	4.8	1208.3	94.2
9	0.075	0.003	0.009	0.0003	0.314	58.0	2.0	73.5	3.3	610.1	104.1
10	0.088	0.004	0.009	0.0003	0.374	60.5	2.0	85.2	4.0	845.8	99.5
11	0.072	0.004	0.009	0.0003	0.325	59.6	1.9	70.6	3.5	458.0	113.2
12	0.090	0.005	0.010	0.0002	0.366	61.2	1.6	87.0	4.6	865.9	106.4
14	0.158	0.015	0.010	0.0003	0.451	62.9	1.9	148.8	13.4	1904.2	157.1
15	0.060	0.003	0.009	0.0002	0.384	57.1	1.5	59.5	2.4	156.7	92.8
16	0.084	0.004	0.010	0.0003	0.218	64.8	2.0	81.9	3.8	613.2	110.1

Table 2.2 continues on next page.

Table 2.2 continued.

Analysis #	Corrected isotope ratios					Corrected ages (Ma)					
	$^{207}Pb/^{235}U$	±2σ (%)	$^{206}Pb/^{238}U$	±2σ (%)	rho	$^{206}Pb/^{238}U$	± 2σ	$^{207}Pb/^{235}U$	± 2σ	$^{207}Pb/^{206}Pb$	± 2σ
17	0.069	0.004	0.009	0.0002	0.198	57.9	1.4	67.8	3.8	432.8	129.7
18	0.068	0.003	0.009	0.0003	0.213	58.1	1.6	66.5	2.7	377.2	100.1
19	0.075	0.003	0.009	0.0002	0.549	57.9	1.4	73.8	3.2	621.3	81.5
20	0.072	0.002	0.009	0.0002	0.195	55.8	1.1	70.4	2.2	595.1	74.4
21	0.066	0.006	0.009	0.0003	-0.004	58.8	1.8	64.8	5.3	287.6	205.5
22	0.069	0.008	0.010	0.0005	0.373	64.1	3.0	67.6	7.2	190.7	237.5
23	0.104	0.006	0.010	0.0003	0.216	65.4	2.2	100.7	5.4	1042.7	119.5
24	0.093	0.006	0.009	0.0002	0.237	59.6	1.3	90.0	5.5	994.2	126.3
25	0.119	0.004	0.010	0.0002	0.428	61.1	1.4	114.3	4.1	1436.0	65.9
26	0.082	0.004	0.009	0.0003	0.250	60.5	1.7	79.9	3.6	703.2	103.5
27	0.074	0.003	0.009	0.0002	0.402	59.7	1.4	72.0	3.2	500.5	92.7
28	0.212	0.018	0.011	0.0003	0.448	69.8	1.7	195.3	14.7	2239.9	129.7
29	0.311	0.031	0.012	0.0005	0.446	79.2	3.3	274.8	23.6	2669.5	145.2
30	0.108	0.007	0.010	0.0003	0.130	63.5	1.9	104.1	6.9	1172.9	142.0
Sample # ST – 2											
1	0.076	0.007	0.010	0.0003	0.169	62.1	2.1	74.1	6.9	476.0	214.6
2	0.075	0.007	0.009	0.0004	-0.143	59.4	2.6	73.2	6.9	548.3	245.8
3	0.072	0.005	0.010	0.0005	0.290	62.0	2.9	71.0	5.0	382.7	167.9
4	0.060	0.003	0.009	0.0003	0.356	57.8	1.8	59.6	2.5	129.3	101.9
5	0.064	0.002	0.009	0.0002	0.424	56.3	1.4	62.7	2.0	311.1	72.4
6	0.187	0.008	0.010	0.0003	0.386	65.1	2.1	173.6	7.1	2138.3	76.9
7	0.258	0.026	0.012	0.0006	0.413	77.6	3.9	232.7	20.6	2389.7	154.0
8	0.074	0.003	0.009	0.0003	0.499	60.5	2.0	72.1	2.8	475.4	83.4
9	0.102	0.006	0.009	0.0003	0.333	60.0	1.9	98.1	5.4	1162.2	111.4
10	0.069	0.005	0.009	0.0003	0.245	57.5	2.0	67.8	4.7	447.3	159.7
11	0.075	0.005	0.010	0.0003	0.394	62.6	2.0	73.0	4.8	427.1	140.7
12	0.064	0.004	0.009	0.0003	0.159	57.3	1.7	63.1	3.5	287.0	136.4
13	0.061	0.003	0.009	0.0003	0.417	59.4	1.7	60.2	3.1	91.6	116.1
14	0.063	0.004	0.009	0.0003	0.378	56.6	1.7	61.7	3.4	263.5	120.7
15	0.104	0.005	0.009	0.0003	0.334	60.6	1.8	100.5	4.5	1191.9	92.3
16	0.096	0.004	0.014	0.0005	0.652	89.1	3.3	92.6	3.7	181.7	77.3
17	0.111	0.004	0.013	0.0004	0.691	82.4	2.3	106.4	3.7	680.5	56.6
18	0.131	0.008	0.014	0.0005	0.646	92.6	3.4	124.7	6.9	787.2	94.2
19	0.063	0.004	0.009	0.0003	0.082	55.9	1.6	62.4	3.6	314.1	144.7
20	0.064	0.006	0.010	0.0003	0.442	61.6	2.0	62.7	5.6	102.9	197.0
21	0.068	0.007	0.009	0.0003	0.797	57.8	1.7	66.9	6.5	403.6	175.6
22	0.068	0.008	0.009	0.0003	0.792	58.6	1.8	66.7	7.6	366.6	214.5

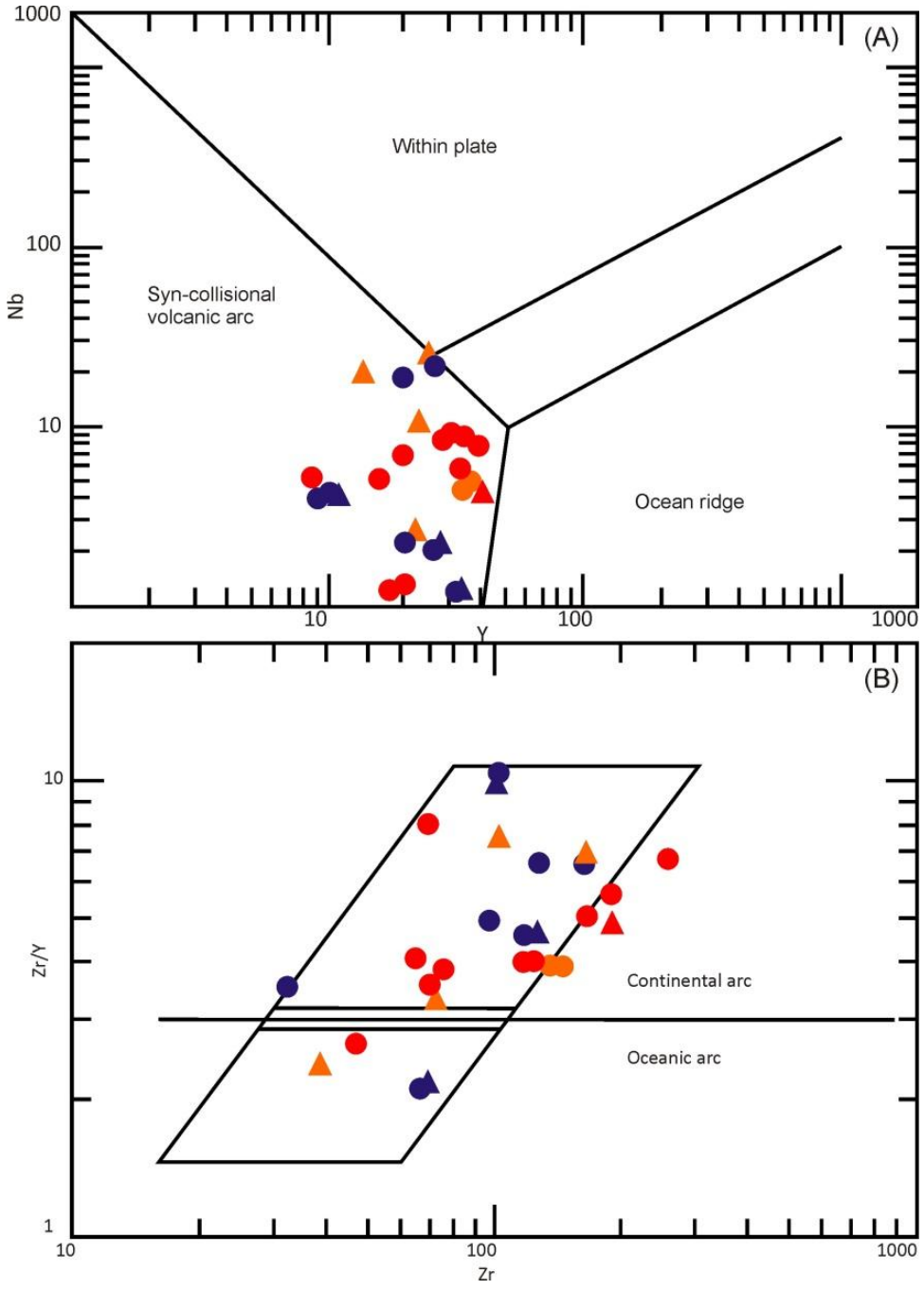

Figure 2.11: Tectonic discrimination diagram for the Chagai-Ras Koh-Khwaja Amran arc system that evolved as a syn-collisional (A) to a continental arc system (B). The outliers may represent the impact of low grade metamorphism and/or alterations. Boundaries in A by Pearce et al. (1984) and in B by Pearce (1983).

2.6. Conclusions

Major and trace elements geochemistry of volcanic and plutonic rocks from the fragments of the Chagi-Ras Koh arc system and Khwaja Amran-Spinatizha Crystalline Complex exposed west of the Chaman fault in Chaman area of Pakistan show subduction related signatures. Granite and diorite samples from the Khwaja Amran-Spinatizha area yield a U-Pb emplacement age of ~ 58 Ma, which suggests that magmatism in this part of the arc system continued until Paleocene.

Chapter 3 : Geomorphic response to an active transpressive regime: a case study along the Chaman strike-slip fault, Pakistan

3.1. Abstract

The Chaman left-lateral strike-slip fault bounds the rigid Indian plate boundary at the western end of the Himalayan-Tibetan orogen and is marked by contrasting topographic relief. Deformed landforms along the fault provide an excellent record for understanding this actively evolving intra-continental strike-slip fault. The geomorphic response to this active fault is studied utilizing digital elevation model (DEM) data integrated with Advanced Spaceborne Thermal Emission and Reflection Radiometer (ASTER) Visible and Near Infra-Red/Short Wave Infra-Red (VNIR/SWIR) and images from GeoEye-1. Geologic and geomorphic mapping reconstructs the geomorphic history of Late Quaternary transpression along a strand of the Chaman fault and the smaller Spinatizha fault in western Pakistan. Topographic analysis of a part of the transpression (the thrust bounded Roghani ridge) reveals northward growth of the thrust with the presence of three water gaps and two corresponding wind gaps. Geomorphic indices of active tectonics including stream length-gradient index, mountain front sinuosity, valley floor width to valley height ratios, and entrenchment of recent alluvial fan deposits are used to define the lateral growth and direction of propagation of the Spinatizha fault. Based on topographic analysis of the Roghani ridge and geomorphic mapping around an impressive alluvial fan, the Bostankaul Fan, left-lateral displacement along Chaman fault and uplift along the Spinatizha fault record slip partitioning along the Indian plate boundary and account for the convergence resulting from the difference in the Chaman fault azimuth and orientation of the velocity vector of the Indian plate.

3.2. Introduction

The interaction between active tectonics and fluvial systems is a key element for understanding Earth's dynamic surface. How evolving thrusts and folds affect coevolving fluvial systems and how fluvial systems influence uplifting blocks, have been studied both in the field and modeled in laboratories (Bernal et al., 2004; Pearce et al., 2004; Miller and Slingerland, 2006; Hilley and Arrowsmith, 2008). These studies are helpful for understanding the kinematics and mechanical evolution of active structures and regional tectonics. Furthermore, study of the characteristic landforms and drainage patterns around evolving structures has been used to infer direction and lateral growth of the structures (e.g. Jackson et al., 1996; Keller et al., 1999; Azor et al., 2002). The geometry and growth rate of structures, interaction of multiple structures, inherited topography, and characteristics of the fluvial system are the main variables that depict this interplay (Burbank et al., 1996). With lateral fault propagation, the fault lengthens in the direction of growth by lateral tip propagation and/or fault linkage (Densmore et al., 2007), which are expressed by the development of distinct topography and landforms (Cowie and Scholz, 1992; Jackson et al., 1996). The geomorphology in tectonically active regimes is therefore a powerful tool to assist in differentiating more active segments of a structure and can help in establishing the structural evolution of a region. The distinction between active and less active structures can be achieved through detailed studies of geomorphic indices of active tectonics, for example, stream length gradient index, mountain front sinuosity, valley floor width to height ratios, entrenchment of Quaternary deposits, and coeval drainage pattern that encompass a fault or fold (Keller and Pinter, 2002; Keller and DeVecchio, 2012).

Yet, there are still few geomorphic studies of evolving thrusts and folds (Cox et al., 2001; Francesco and Marta, 2011). I therefore examine here the geomorphic development of actively evolving thrusts within a restraining bend along the left-lateral Chaman strike-slip fault system in western Pakistan (Figure 3.1) to understand its evolution within an active plate boundary zone, which accommodates both lateral translation and convergence of the Indian plate beneath the Eurasian plate. The task is accomplished by using high-resolution satellite data, digital elevation models (DEMs), field investigations, and analysis of geomorphic indices. The arid climate and the sparse vegetation in the study area provide a good opportunity for the application of remotely sensed data.

3.3. Regional setting and study area

The Chaman fault stretches for ~ 860 km along the border regions of Pakistan and Afghanistan and is one of the world's major terrestrial transform faults. The geologically constrained 460 ± 10 km displacement along the Chaman fault with a slip rate estimated to be 24 - 35 mm/yr (Beun et al., 1979; Lawrence et al., 1992) accounts for about 70% of the ~ 36-45 mm/yr (Klootwijk et al., 1992; Molnar and Stock, 2009) of total collision of the Indian Plate into Asia. Recent sporadic GPS studies reveal 18 ± 1 mm/yr slip along the fault (Mohadjer et al., 2010), while Interferometric Synthetic Aperture Radar (InSAR) analysis along a part of the fault suggests slower movement at ~ 8 mm/yr (Furuya and Satayabala, 2008). Historical and recent instrumental seismic record, with the exception of 1892 M_w = 6.8 Chaman earthquake, along northern segment of the Chaman fault that runs through Pakistan (Figure 3.1) shows a gap in major seismic activity. Ambraseys and

Strike-slip fault
Thrust fault
Shear zone
Tarim Basin
Himalayan Convergence Zone
ATF
KF
HF
35°N
MBT
PS
KA
CF
GF
SK
AFGHANISTAN
30°N
CA
GBF
PAKISTAN
36 - 45 mm/yr
INDIA
Makran Subduction Zone
ONF
65°E
70°E
75°E
300 km

Figure 3.1: Location of the Chaman fault (CF) at the western end of the Himalayan-Tibetan orogeny; displayed on shaded relief map based on SRTM elevation data. CF marks the sharp boundary between Indian and Eurasian plates as a single continuous linear feature running from Makran subduction zone in the south to the Himalayan convergence zone in the north. Exposed outcrops of Kandahar arc (KA) and Chagai arc (CA) are shown in yellow hatches after Lawrence et al. (1981), while Indian Plate velocity is shown after Molnar and Stock (2009). ATF: AltynTagh Fault; GF: Gardiz Fault; GBF: Ghazaband Fault; HF: Herat Fault; KF: Karakoram Fault; MBT: Main Boundary Thrust; ONF: Ornach-Nal Fault; PS: Panjao shear; SK: Suliman-Kirthar Fold-thrust Belt; (modified after Khan et al. 2009; Mohadjer et al., 2010).

Bilham (2003) attributed this period of inactivity along the fault as non-representative of the long-term activity and have forecasted an overdue $M_w = 7$ event in the region where Late Quaternary activity along the Chaman fault system is evident from the deformed alluvial fan deposits, deflected drainage patterns, and pressure ridges (Lawrence et al., 1992).

The geomorphic expression of the Chaman fault system is evident throughout its entire length, mostly at the contact between the Quaternary deposits on the west and meta-sediments of the Late Eocene to Oligocene Katawaz Basin (Carter et al., 2010) to the east (Ruleman et al., 2007). Exceptions are where the fault brings slivers of the Late Jurassic to Cretaceous arc rocks west of the fault zone in contact with the meta-sediments (Lawrence et al., 1981). The segment of the Chaman fault that runs through western Pakistan represents the southern subsidiary system of the main shear zone (Figure 3.2). This segment is represented by linear zones that are < 1 km wide to zones of multiple strands with conjugate Riedel shears, and thrust fault systems that merge with the main fault (Lawrence and Yeats, 1979; Wheeler et al., 2005). The overall trend of the fault varies from N10°E to N35°E throughout its length due to the presence of many double bends in the fault (Lawrence et al., 1992). An example of a restraining bend is present between 30.50° N and 30.75° N where the main Chaman fault is joined by two subsidiary faults west of the main trace of the Chaman fault that Lawrence and Yeats (1979) call the Traqqi and Ghunzakhai faults. The trace of the main stretch of the Chaman fault in this area changes from ~ N17°E to about ~ N28°E north of village Bostankaul (Figure 3.1,

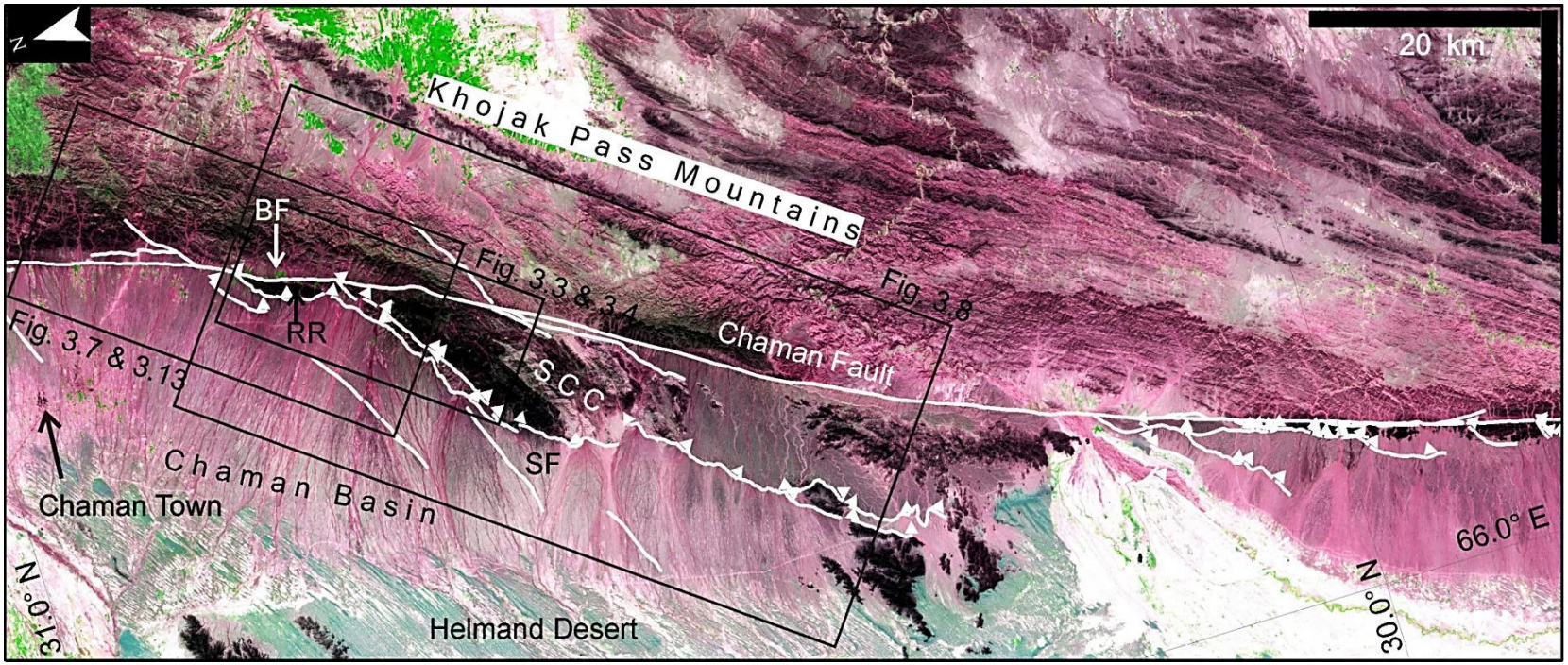

Figure 3.2: A segment of the Chaman fault illustrating a gentle bend in the azimuth of the fault and the associated areas of subsidiary structures (Background image ASTER 1-3-2). The Chaman Basin provides accommodation for the alluvial sediments eroded away from the uplifting Khojak Pass Mountains recording the interplay between this huge alluvial fan system and the Chaman fault system. The pop-up zone comprising of Spinatizha Crystalline Complex (SCC) and south-central part of the alluvial sediments of Chaman Basin marks the transpression along this double bend in the Chaman fault. RR: Roghani Ridge; SF: Spinatizha Fault; BF: Bostankaul Fan.

30.75° N/66.48° E). The Chaman fault continues along that trend until ~ 30.35 N°, where the trend then becomes ~ N15°E. Along this curved segment of the Chaman fault an incipient transpression, smaller in size but similar in geometry to the restraining bends reported elsewhere along the fault (Ruleman et al., 2007), is present to the west of the fault.

The transpressional bend has resulted in a pop-up block composed mostly of crystalline basement complex, and represents a N30°E trending ridge that is > 50 km long and ~ 10 km wide, but tapers out to the north. The crystalline basement complex is in contact with the Katawaz Basin sediments on its eastern side and is emerging from below the Quaternary alluvial fan sediments of the Chaman Basin. This uplifted block is unusual because the long-term sense of vertical displacement is east side up (Lawrence et al. 1992), resulting in the uplift of the eastern side Katawaz Basin sediment against the Quaternary alluvium along the western side of the fault. The present landscape is a consequence of the time–integrated interactions between the Chaman fault system and its associated structures, and the extensive bajada that originates from the Khojak Pass Mountains.

The Spinatizha Crystalline Complex, which comprises a part of the study area, is in the northern part of the pop-up zone and is composed of crystalline basement rocks that are not seen anywhere else in Pakistan west of the Chaman fault. This was mapped by Lawrence et al. (1981) and was divided into: (1) the Spinatizha Metamorphic Complex; (2) the Bazai Ghar Volcanics; (3) the Khawja Amran Intrusive Series; and (4) a

sedimentary sequence of unknown affinity. A wide range of rock compositions, similar to the widespread Late Jurassic to Cretaceous arc material present elsewhere, mostly west of the Chaman fault, were geochemically analyzed for petrographic study (Lawrence et al., 1981). The Spinatizha Crystalline Complex was interpreted by Lawrence et al. (1981) to be a sliver detached either from the Kandahar or Chagai arcs, and subsequently uplifted along the Chaman fault (Figure 3.1). The Kandahar and Chagai arcs are composed of pre-Indo-Eurasian collision granitic and andesitic rocks that formed on the southern edge of the central Iran, Lut and Afghan micro-continents extending to northeast as an oceanic arc (Lawrence et al., 1981; Treloar and Izzat, 1993). This study provides an insight into the evolution of this transpression along the Chaman fault and its impact on the associated evolving landscape.

3.4. Datasets and methods

DEM data extracted from Advanced Spaceborne Thermal Emission and Reflection Radiometer (ASTER) instrument were used for topographic analysis and to calculate geomorphic indices. ASTER data were also used for geological/geomorphic mapping. In addition, high resolution GeoEye-1 image data covering ~ 50 km^2 of the study area was used to help confirm the results derived through ASTER data. High-resolution images from Google Earth database were also utilized for geomorphic analysis.

The ASTER instrument, developed by National Aeronautics and Space Administration (NASA) and Japan's Ministry of Economy Trade and Industry (METI), is onboard the

Earth Observing System (EOS) TERRA satellite launched in December 1999, and it records Visible and Near Infra-Red (VNIR), Shortwave Infra-red (SWIR) and Thermal Infra-Red (TIR) portion of the solar radiation in fifteen spectral bands with wavelength ranges of 0.53 – 0.86 μm, 1.60 – 2.43 μm, and 8.13 – 11.65 μm, respectively (Yamaguchi et al., 1998; Table A1). Four VNIR bands at 15 m resolution (including the backward-looking telescope in Band 3 providing data as Band 3b for digital stereo-pair/DEM generation), six SWIR bands at 30 m resolution, and five TIR bands at 90 m resolution record spectral data with swath widths of 60 km. ASTER data were selected for use in this study because of its relatively high spectral (15 m in the VNIR bands) and comprehensive (15 bands covering 0.52 to 11.65 μm) resolution.

GeoEye-1 is a commercial satellite launched on September 6, 2008 that can image Earth's surface in any direction in panchromatic mode with a ground resolution of 0.41 m and multispectral mode with a ground resolution of 1.65 m (www.geoeye.com). Although the spectral resolution of 450 – 800 nm (panchromatic one band) and 450 – 920 nm (multispectral including three visible and one near infra-red) is restricted to Visible and Near Infra-Red, however, the high ground resolution favors large-scale geomorphic mapping. The ground accuracy of 4 to 6 m makes the GeoEye-1 data as one of the most accurate sub-meter sized imagery available (Table A3).

3.4.1. Geological/geomorphic mapping

ASTER bands combinations, ratios, and principal component analysis (PCA) applied to two ASTER granules (L1B data) acquired on June 14, 2007 were used for lithological discrimination and structural interpretation of the area. I selected these scenes because of the absence of clouds and the absence of snow on mountains within the study area during this time of the year. Further, the study area is a part of the Helmand desert with little vegetation cover. ASTER L1B data product (abbreviated as AST_L1B; Table A2) is registered radiance at the sensor dataset with surface reflectance as VNIR and SWIR, and thermal emissivity as TIR (Abrams et al., 2004). Log residual algorithm, which reduces noise from topography, instrument and sun (Khan and Khalid, 2008) was applied to the AST_L1B to account for any impacts of the topography on the data quality. The Darkest Pixel (DP) atmospheric correction method, which is useful for VNIR and SWIR ASTER data (Hadjimitsis et al., 2010) was applied to the data in this study using DARK_SUB_DOIT extension of ITT Envi-4.8. However, no apparent deviation from the original data was encountered after DP correction and I preferred to use the original data to avoid any undesired changes to the original image data due to the correction.

Among the several band combinations that were considered it was found that VNIR band-1, band-3, and band-2 combination displayed as red-green-blue (RGB) color composite was better suited to examine the general geologic and land cover overview of the area (Figures 3.2). This bands combination reflects a close to true ground color combination and is helpful in defining regional scale rock suites, landforms, and lineaments (Kalinowski and Oliver, 2004).

Band ratios enhance the spectral differences between bands, reduce the effects of topography by dividing one spectral band by another, and produce an image with relative band intensities. Each ratio displays spectral contrast of specific absorption features (Rowan and Mars, 2003). When displayed as color composites these combinations of different band ratios provide useful information about the surface features and materials. ASTER band ratios have proved useful to suppress brightness differences related to grain size variations (Khan and Glenn, 2006) and mineral/rock content of a surface (Kalinowski and Oliver, 2004). I examined several band ratios, among which the combination of 5/7-5/1-5/4 and 4/5-6/7-3/4 were found very useful for broad mapping and delineation of sediments and sedimentary rocks from metamorphic and intrusive igneous rocks (Figures 3.3 and 3.4).

Multispectral data bands are normally highly correlated to each other, which reduces contrast in output images. Principal Component Analysis (PCA) transforms multispectral data bands to produce uncorrelated output bands by finding a new set of orthogonal axes that have their origin at the data mean and that are rotated to maximize the data variance. The output data bands have segregated noise components and reduced data dimensionality (Kalinowski and Oliver, 2004). The percentage of data variance decreases from first PCA bands towards the last PCA bands, which are noisier with little variance. PCA bands produce more colorful composite images than the uncorrelated spectral color composite images (Richards, 1999).

The ASTER VNIR and SWIR data from two scenes were transformed using PCA tool of ITT Envi-4.8 software. The PCA VNIR bands transformation was most useful in classifying lithology throughout the study area because of the higher values of data variance. The PCA first forward transformation combinations of RGB 1-3-2 and 3-2-1 were used in the final classification (Figure 3.5). The ASTER PCA allowed Quaternary deposits to be differentiated into four major alluvial fan units, and to map the sharp contacts between alluvial fan sediments and crystalline bedrock. The PCA was also helpful in differentiating alluvial fan sediments from sedimentary bedrock. The surface expression of the loose sediments as compared to the lithified bedrock and the presence of hydroxyl (OH^-) content of the weathered clays and presence of water content (Kalinowski and Oliver, 2004) in the alluvial deposits in the study area provide a possible explanation for the contrast on the PCA images (Figure 3.5). These two PCA bands' combinations were specifically useful in mapping the individual rock units within the Spinatizha Crystalline Complex.

I was able to further refine the rock units mapped by Lawrence et al. (1981) using the remote sensing. This helped us identify and map several additional structural strands of the Chaman fault that had not previously been recognized (Figure 3.8). PCA was especially effective in differentiating the previously undifferentiated metamorphic and intrusive rock units in the central part of the mapped area. The ASTER band ratios and PCA were also helpful in examining the drainage pattern of the study area that in turn helped in mapping the Spinatizha fault and strike-slip lineaments present between the

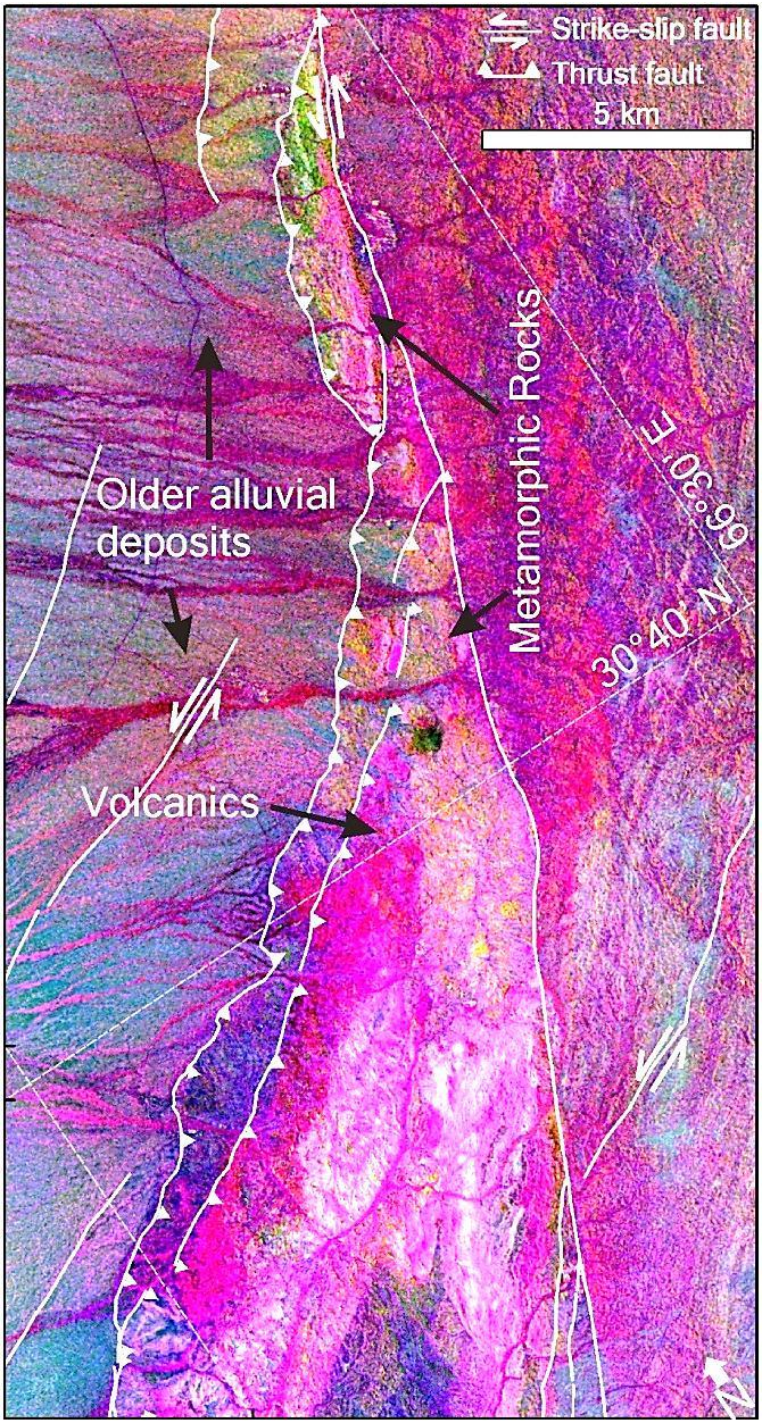

Figure 3.3: ASTER band ratios 5/7-5/1-5/4 were helpful in delineating different rock types and structural lineaments. For the location see Figure 3.2. This bands ratio combination differentiate among different alluvial fan generations based on presence of water content ($^{-}$OH) in the younger surfaces from the older dry surfaces.

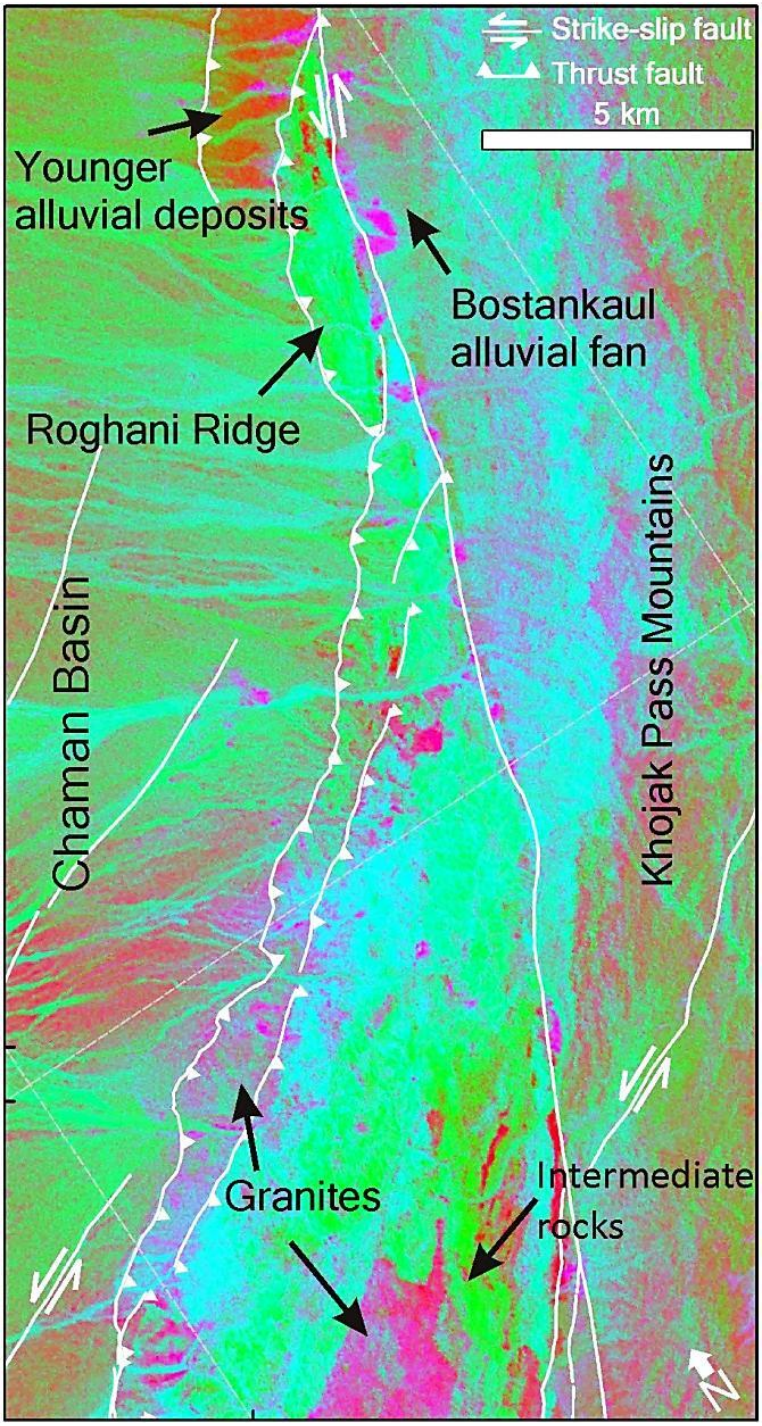

Figure 3.4: ASTER band ratios 4/5-6/7-3/4. This bands ratio was especially helpful in differentiating different generations of the alluvial fans. For the location see Figure 3.2. This bands ratio combination reflects contrast in clay content and texture of the surfaces, hence weathered crystalline rocks and younger fans (dark green colors) stands out different from the intact granitic bodies (pink), bluish colored volcanic and sedimentary bedrock of the Khojak Pass Mountains.

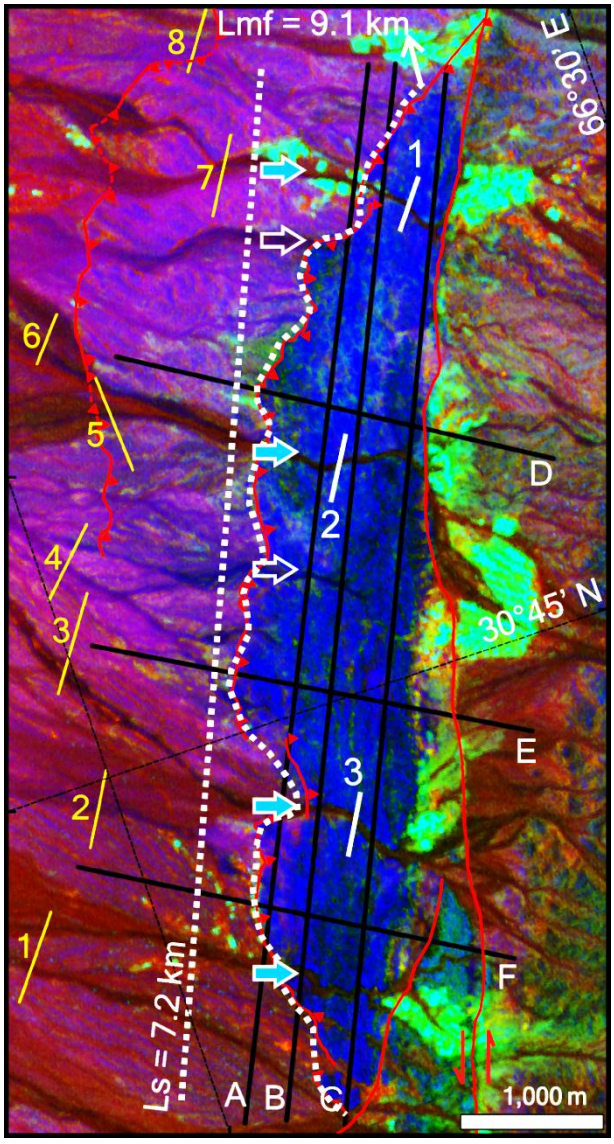

Figure 3.5: First Forward PCA of ASTER VNIR and SWIR displayed as 1-3-2 (RGB) used in geologic/geomorphic mapping. Notice the lenticular Roghani ridge (dark blue colored rock body) flanked by alluvial fan deposits (pink to dark pink colored on west of the ridge) with position of wind (white hollow arrows) and water gaps (blue filled white arrows). Green-colored patches are vegetated areas. The central water gap and the corresponding wind gap are 1348 ± 15 m apart. Black lines A-F are the topographic profile lines shown in Figure 3.12. Numbered white lines are the stream profiles used in Figure 3.14 while numbered yellow lines are stream profile lines used in Figure 3.15. Dashed white curved line (L_{mf}) is the measured length of mountain front of the Roghani ridge while dashed white straight line (L_s) is the equivalent parallel straight line used in mountain front sinuosity calculation ($S_{mf} = L_{mf}/ L_s = 1.27$). The Spinatizha thrust and Chaman strike-slip faults tend to maintain a straight front of the ridge that is dissected by the local drainage system.

Spinatizha and Chaman faults. GeoEye-1 image was used for geomorphic mapping of a deformed landform to measure the surface displacement associated with the Chaman and Spinatizha faults (Figure 3.6).

3.4.2. DEM extraction and geomorphic indices

A DEM was extracted using OrthoEngine Module of Geomatica 10 from a single ASTER image (L1A granule) acquired on June 14, 2007 covering the northern part of the study area. Occasional holes within the dataset in the DEM were filled through interpolation of the surrounding data. The DEM was exported as Geotiff into the ESRI ArcGIS software package for topographic analysis, for drainage extraction (Figure 3.7), and to calculate geomorphic indices.

3.4.2.1. Stream length-gradient index (SL)

The SL index provides a measure of the erosional resistance of the rocks involved and relative intensity of active tectonics (Azor et al., 2002; Keller and Pinter, 2002) and is defined as: $SL = (\Delta H/\Delta L)*L$ (equation 1)

where $\Delta H/\Delta L$ is the channel gradient of a particular reach of a stream (ΔH is the change in elevation along the length (ΔL) of the reach) and L is the total length of the channel from the midpoint of the reach to where the index is calculated upstream to the divide. The index is sensitive to channel slope, which is a result of tectonic activity, stream power and/or rock resistance in an area. SL values for and around the Roghani ridge were calculated using ASTER DEM for major streams identified during field visits and from ASTER PCA.

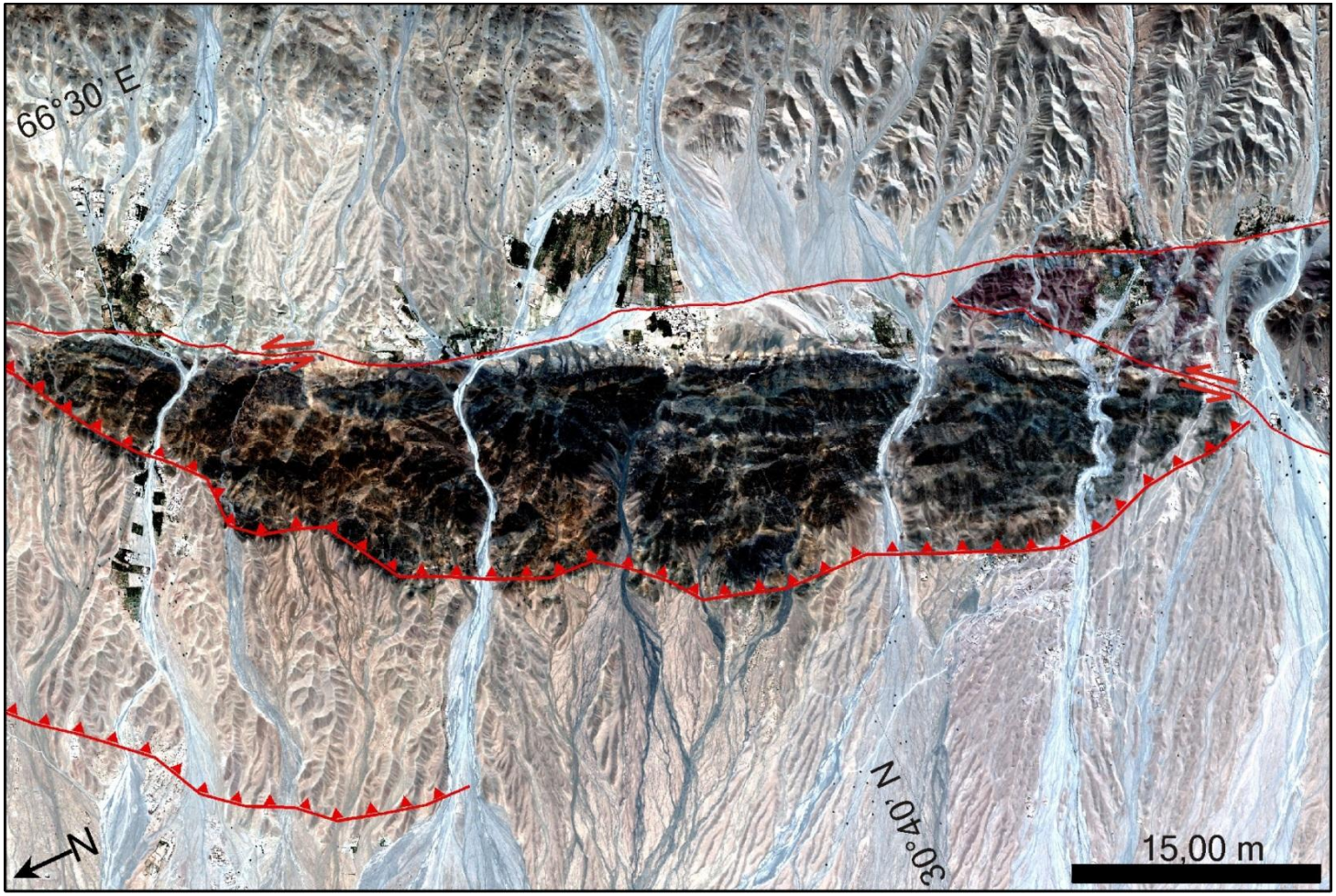

Figure 3.6: GeoEye-1 multispectral bands 1 (red), 2 (green), and 3 (blue) (with ground resolution of 1.65 m) are displayed as color composite RGB image of the Roghani ridge and Bostankaul alluvial fan. A part of the fan has displaced left-laterally ~ 1150 ± 55 m along a strand of the Chaman fault. The evolving Roghani ridge records stream deflection and quenching as wind and water gaps.

3.4.2.2. Valley floor width to valley height (Vf) ratio

The valley floor width to valley height (V_f) ratio is a measure of the valley floor width (V_{fw}) to the elevation divide at the right (E_{rd}) and left (E_{ld}) of the valley at a set distance from the mountain front (Keller and Pinter, 2002) and is calculated as:

$$V_f = 2V_{fw}/[(E_{ld} - E_{sc}) + (E_{rd} - E_{sc})] \qquad \text{(equation 2)}$$

where E_{sc} is the average elevation of the valley floor. Higher V_f values correspond to flat-floored valleys representing low tectonic activity in contrast to low V_f values for V-shaped valleys, which are related to rapidly uplifting mountain ranges with higher valley incision (Azor et al., 2002). V_f values for three antecedent streams across the Roghani ridge were measured using the DEM generated from the ASTER data.

3.4.2.3. Mountain-front sinuosity (Smf)

Mountain-front sinuosity (S_{mf}) defines the interaction between erosion and tectonics (Azor et al., 2002; Keller and Pinter, 2002). Active tectonics tends to generate a straight mountain front while erosional processes cut embayments into a mountain front. S_{mf} values were calculated as the ratio between the length of the mountain front (L_{mf}) and the straight-line length (L_s) approximately parallel to the mountain front such that:

$$S_{mf} = L_{mf}/L_s \qquad \text{(equation 3).}$$

More active tectonics results in lower S_{mf} values. ArcGIS was used in measuring the mountain front and the corresponding front parallel line.

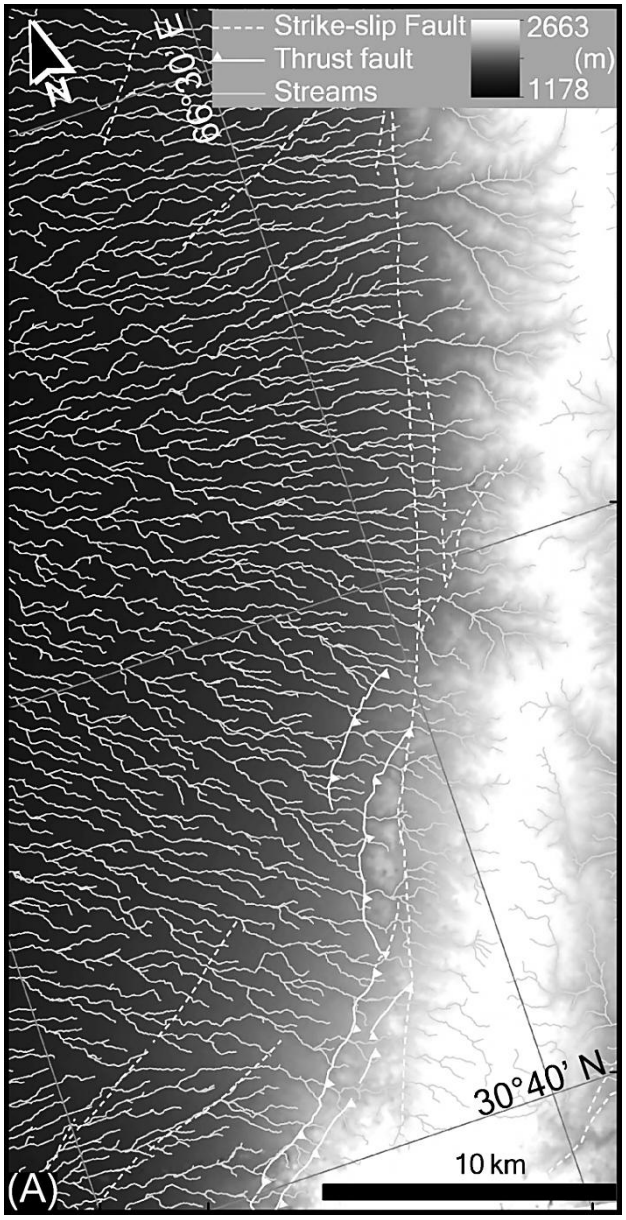

Figure 3.7: ASTER absolute DEM derived from 15 m VNIR 3N and 3B stereo images using 19 Ground Control Points (12 GPS ground points and 5 points from the topographic maps) and 15 Tie Points (mostly in parts of the image area where no elevation data was available) with average Root Mean Square (RMS) Error of 9 - 11 m horizontal and ~ 9 m vertical, displayed with drainage extracted from DEM data of the study area. The abrupt increase in topographic relief at the eastern side of the Chaman fault provides vast amount of sediment supply to the low-lying area of the Chaman Basin. Note the almost parallel, linear and transverse streams orthogonal to the Chaman fault in their proximity to the fault trace. The drainage pattern becomes oblique to almost longitudinal (northwestern part of the map) in a medial position in the basin. See Figure 3.2 for the location.

3.4.2.4. Entrenchment of Quaternary deposits (E)

Recent river entrenchment (E) is calculated as the difference in elevation between a channel bed and the alluvial plain that is being incised (Azor et al., 2002). Higher E values reflect longer uplift histories while lower E values reflect relatively recent uplift. With lateral fault propagation, values of E are expected to decrease in the direction of fault growth. Transverse stream profiles based on ASTER DEM were measured using Spatial Analyst extension of ArcGIS at a constant distance from the mountain front.

3.4.3. Field datasets

The Roghani ridge and Bostankaul alluvial fan were chosen for detailed field study (Figures 3.5), mainly because of their position within the zone of transpression and their accessibility. Topographic maps based on DEM derived from 15 m ASTER VNIR stereo-pairs together with 1:50,000 scale topographic maps of Survey of Pakistan were used as base maps for geomorphic mapping of the Quaternary landforms, drainage patterns, and sediments. In addition, stratigraphic sections along stream cuttings within alluvial fans of different ages and their lateral extents were measured. Soil development, vegetation type and cover, rock weathering, and degree of rock varnishing development were used to develop a morphostratigraphy for the Quaternary alluvial fans. Widths and depths of the three antecedent streams across the Roghani ridge were measured across several reaches. Terraces and bars present along these streams and within the valleys were mapped by walking along the boundaries of the individual landforms using a GPS with a ~ ± 5 m horizontal ~ ± 10 m vertical uncertainty. The map units (field-based polygons) were

exported to ESRI ArcGIS and compared with the landforms classified from the ASTER datasets to confirm their locations and sizes, and in particular the width and length of the streams within the study area. The width of the mapped streams and terraces matched within < 5 m with the polygons extracted from ASTER data.

3.5. Results

I extended the structural mapping of Lawrence et al. (1981) to the south of their study area. Emphasis was placed on understanding the interaction between structural evolution of the pop-up zone, which comprises of the Spinatizha Crystalline Complex in the north and the Quaternary sediments and landforms in the south, together with the surrounding coeval alluvial fan system.

The north and central part of the mapped area is the most structurally complex, with a comparatively wider Chaman fault zone comprising of a major fault trace with multiple converging synthetic faults and two antithetic faults (Figure 3.8). The shear system is more evident either within the Spinatizha Crystalline Complex on the west or the meta-sediments of the Katawaz Basin to the east. At the contact between the crystalline and sedimentary rocks in the fault zone, the alluvial fan deposits are either eroded away or are highly deformed and present only as small patches. Along the southern part of the Chaman fault the wide fault zone converges into a more continuous and linear fault trace with a left-lateral displacement of the transverse streams along the contact of the Quaternary alluvial fan deposits and sedimentary bedrock (Figure 3.9). Fault gouge is locally present in small patches along the fault trace, and is mainly composed of reddish

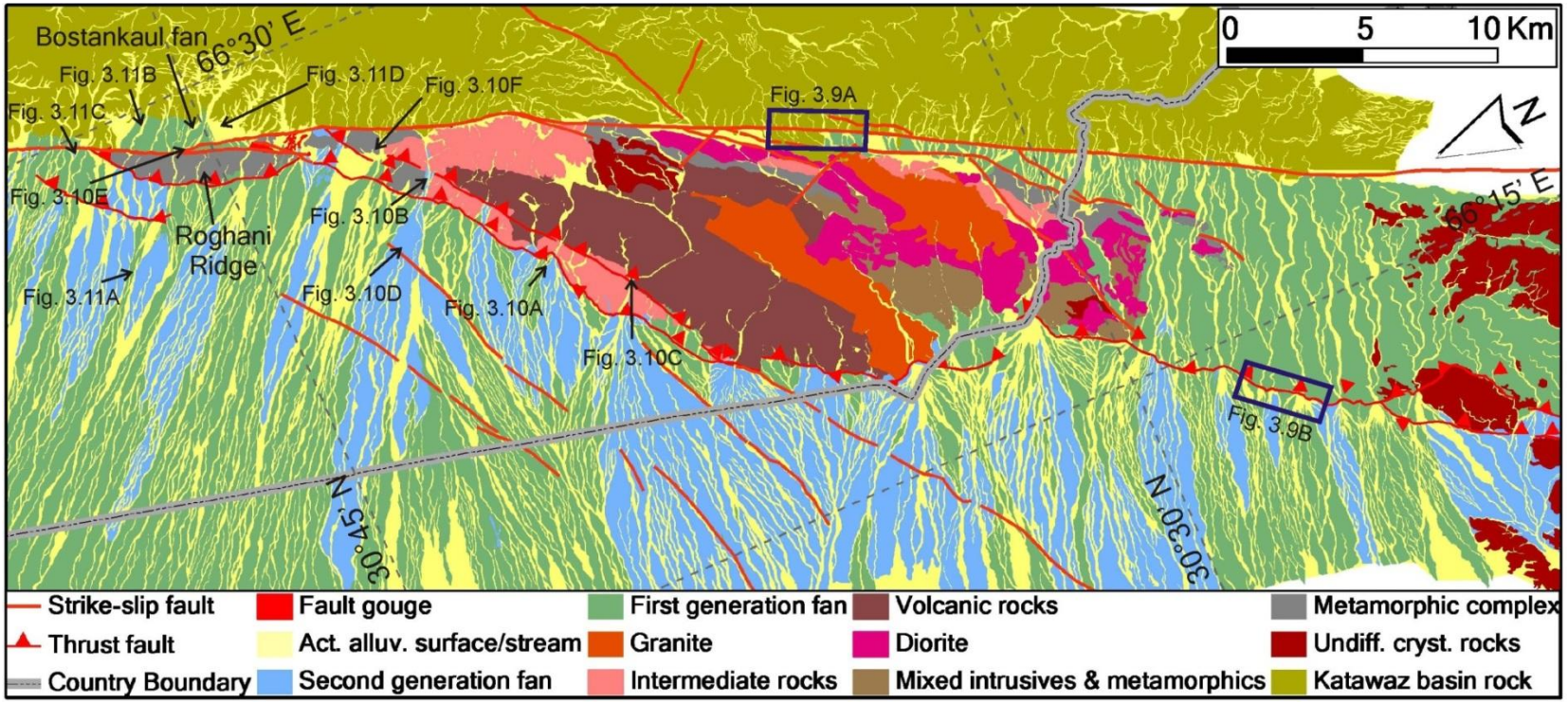

Figure 3.8: Geology of the Chaman and Spinatizha faults, and surrounding areas. The strike-slip strands of the Chaman fault system in the left half of the map is a complex shear zone incorporating rocks from both the meta-sediments of Katawaz Basin and rocks of the Spinatizha crystalline complex, which is considered to be fragments of the Cretaceous arc rocks exposed west of the Chaman fault. The arc-shaped south-east directed Spinatizha fault is an active frontal thrust that resulted from the combination of compression and strike-slip motion on the Chaman fault. The resultant topographic high along this thrust has strongly influenced the alluvial fan system of the Chaman Basin with deep stream entrenchment, deflection and quenching.

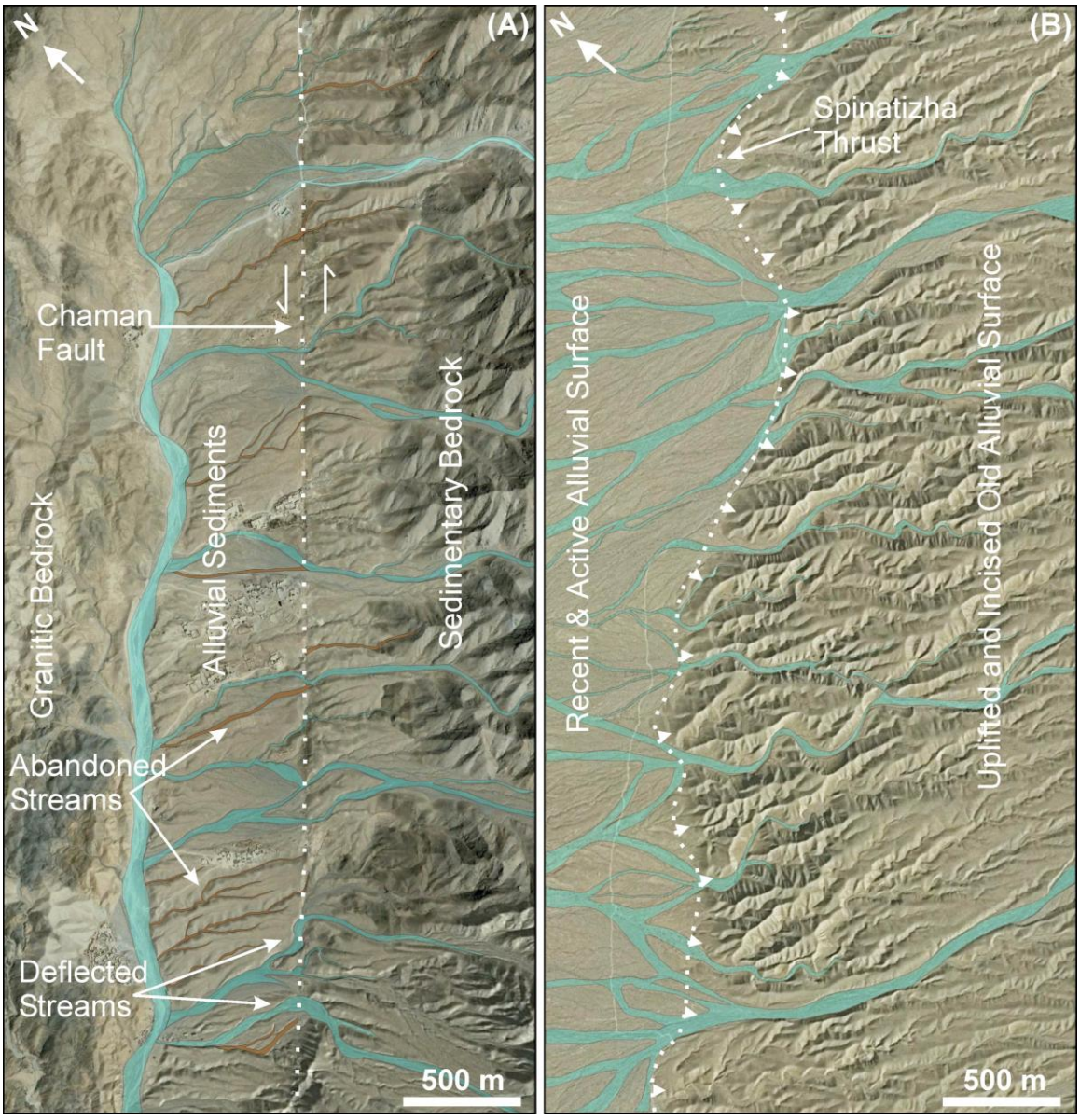

Figure 3.9: Thrust and strike-slip faults' distinctive geomorphic expressions captured on Google Earth high-resolution images (for the location see Figure 3.8). (A) Single trace of the Chaman fault along which the drainage system and old alluvial fan surfaces have been abandoned and left-laterally displaced. (B) The Spinatizha thrust has uplifted the alluvial surface, which is incised by a laterally migrating, almost parallel stream network. In the footwall of the fault the drainage pattern braids away from a single source point reworking the abandoned surface.

to dark grey colored mylonitized clay-rich material with occasional sandstone/shale blocks incorporated from the sedimentary rock of the Katawaz Basin.

The main finding of this study is the recognition of a southeast-dipping thrust fault, named as the Spinatizha fault. The Spanatizha fault thrusts crystalline bedrock over Quaternary alluvium. In addition, a bajada is present that records progressive propagation of the Spintizha thrust fault. I first describe and discuss the consequences of the actively interacting strike-slip and thrust faults on the coeval bajada of the Chaman Basin and then discuss the nature of the Spinatizha thrust fault.

3.5.1. Chaman alluvial fan system

The mapped area covers a part of the Chaman Basin, which is an elongated, arc-shaped, and asymmetrical accommodation zone for sediment derived from the eastern Khojak Pass Mountains. The Chaman Basin was created as a flexure within the eastern Eurasian Plate margin crust, which most probably composed of Cretaceous arc rocks (Treloar and Izzat, 1993; Jadoon and Khurshid, 1996), in response to the uplifting eastern block of the Chaman fault. The rising Khojak Pass Mountains, which borders the Chaman Basin to the east, is composed of Oligocene to Recent Katawaz Basin sedimentary rocks that are mainly shale and sandstone, some of which have experienced low-grade metamorphism. The Helmand desert flanks the western side of the basin, and two unnamed basins similar to the Chaman Basin flank the northern and southern ends of the basin (Figure 3.2). The Chaman Basin is ~ 80 km long and 20 km wide in its central part. The ephemeral streams

network that feeds the basins is mainly comprised of moderate to highly incised discontinuous channels occasionally transforming into deep gorges (Figure 3.10 A). These streams are unstable and shift across the valley floor continuously producing terrace risers and mid-channel bars (Figure 3.10 B).

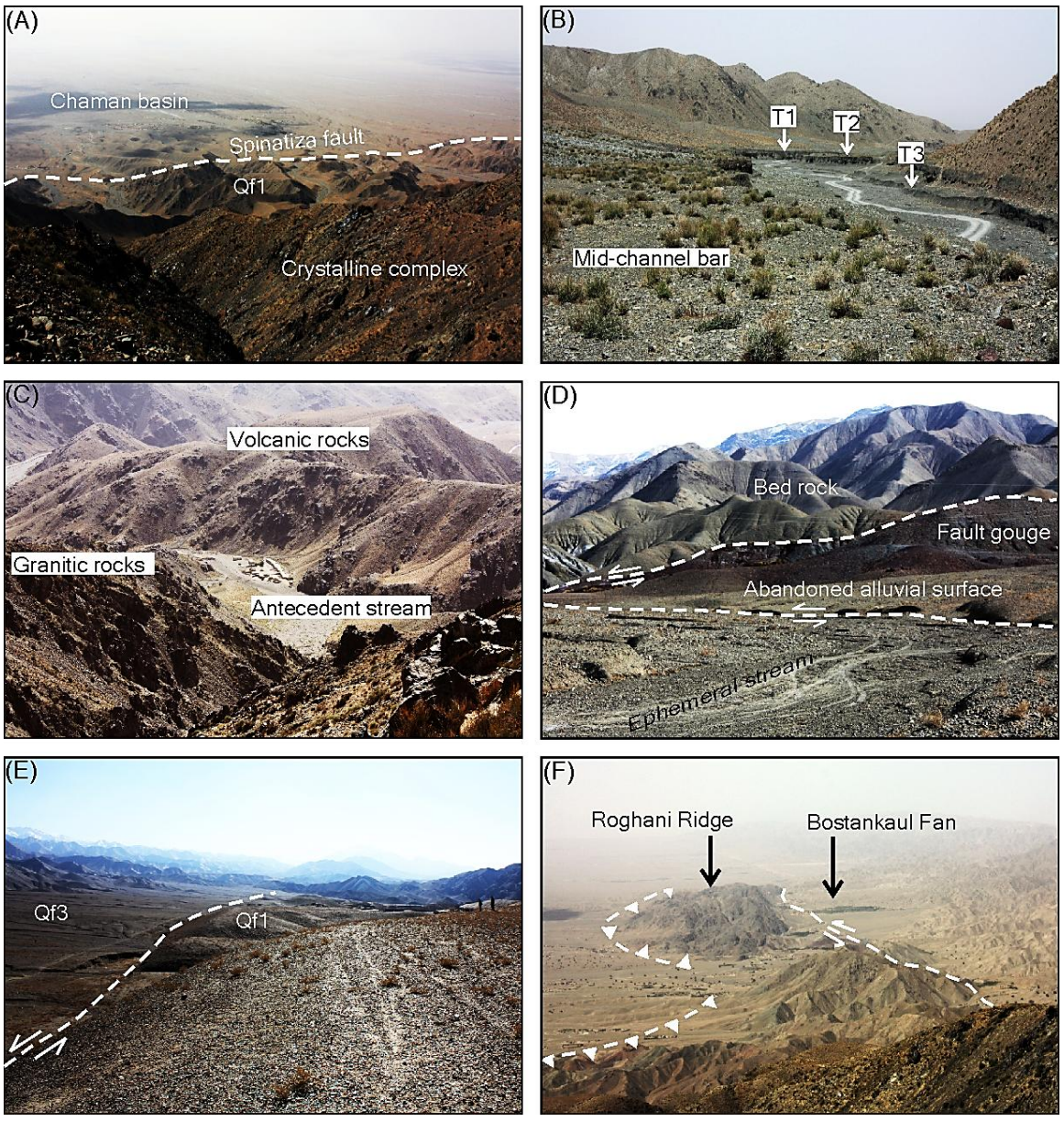
(A)
Chaman basin
Spinatiza fault
Qf1
Crystalline complex
(B)
T1
T2
T3
Mid-channel bar
(C)
Volcanic rocks
Granitic rocks
Antecedent stream
(D)
Bed rock
Fault gouge
Abandoned alluvial surface
Ephemeral stream
(E)
Qf3
Qf1
(F)
Roghani Ridge
Bostankaul Fan

Figure 3.10: Typical geomorphic settings in the study areas. See location of each field photograph in Figure 3.8. (A) View looking west at the ephemeral streams network at the foothills of the pop-up zone. These highly incised discontinuous channels in the high ground drop their load as these cross the probable location of the Spinatizha fault to becoming dispersed from a single source point occasionally transforming into deep gorges. (B) River terraces and active bars west of the main Chaman fault. Terraces and bars reflect degradational and agradational phases during the life span of a stream respectively and are the result of tectonic uplift and consequent erosional processes. (C) One of the several antecedent streams that cut across the rising thrust block. This stream is flowing along a NW directed fault at the contact of granitic and volcanic rocks of the Spinatizha crystalline complex. (D) A northwest striking synthetic strike-slip fault cutting across an abandoned alluvial surface. An active ephemeral stream follows the trend of this secondary fault of the shear system. (E) Looking south along a strand of the main Chaman fault displacing first generation of alluvial sediment (Qf1) against the third generation alluvial fan sediment (Qf3). (F) View looking northwards along the pop-up zone, the Roghani ridge, between Chaman and Spinatizha faults, which marks the northern extent of transpression. This isolated ridge is emerging from a mantle of Quaternary alluvium including the displaced Bostankaul alluvial fan to the east of the ridge. The ridge mainly comprises metamorphic rocks of the Spinatizha crystalline complex.

Two major streams patterns are common within the basin: (1) linear, almost parallel channels with well-defined channel banks, and (2) an anastomosing channel system that is developing a semi-dendritic pattern with less defined and migrating stream channels. In the mapped area, these two patterns are interchanging irrespective of the channel bed lithology (Figure 3.8). The dominant factor causing this drainage pattern is the actively evolving structures within the basin associated with the Chaman fault system as the other factors including, bedrock lithology and climate are constant in the study area.

Stream density within the basin is almost constant, except in the area underlain by crystalline bedrock, which is characterized by a less dense and deeply incised narrow antecedent streams network (Figure 3.10 C). However, these streams frequently follow the crosscutting splays of the Chaman fault (Figure 3.10 D; Lawrence et al. 1981).

The Khojak Pass Mountains are the main source of sediment for the alluvial fans sediment (Figure 3.11 A). Although the Khojak Pass Mountains provide the bulk of the sediment in central part of the basin, numerous boulders and framework sediments are sourced from the Spinatizha Crystalline Complex (Figure 3.2). Consequently either the crystalline rocks are the younger part of the transpression or these rocks are very resistant to erosion, and are not contributing to the sediment budget of the Chaman basin.

Based on my fieldwork and ASTER image interpretation I was able to differentiate four major generations of alluvial fans development (Figures 3.8 and 3.10 E). The oldest generation (green colored polygons in Figure 3.8) underlies most of the Chaman basin

and is proximal to the major structures within and around the basin. The alluvial fan sediments are mainly flashflood deposits comprising monotonous successions of fanglomerate that reach thickness as much as 40 m and are present along both sides of the main Chaman fault (Figure 3.11 B). Particle sizes range from meter-sized boulders to clay matrix, but no sorted sediment was present. Boulders frequency, however, decreases down alluvial fan. Most of the alluvial fans coalesce to form bajada; however, in places of incision by two adjacent streams and/or where uplift has produced isolated inliers of alluvial fan sediment. The alluvial fan sediments are unconsolidated, but carbonate cement is present at some locations, which result in partial lithification of the alluvial fan sediments (Figure 3.11 C). Soil has developed to a depth of about 1 m on most of the oldest alluvial fan surfaces.

The second generation of alluvial fans (blue polygons in Figure 3.8) is incised within the oldest alluvial fans, and covers most of the older landscape within the basin. With continued uplift and the consequent shift of the depositional center in the basin the previously deposited sediments were eroded away and re-deposited downstream. The alluvial fan sediments are comparatively rounded, polymictic and have particle sizes ranging from the occasional meter-sized boulders to clay-rich matrix. These fanglomerates are unconsolidated and massive, typical of flashflood deposits.

The third-generation alluvial fans (yellow polygons in Figure 3.8) are much more localized and are deposited along the margins of individual older alluvial fans within

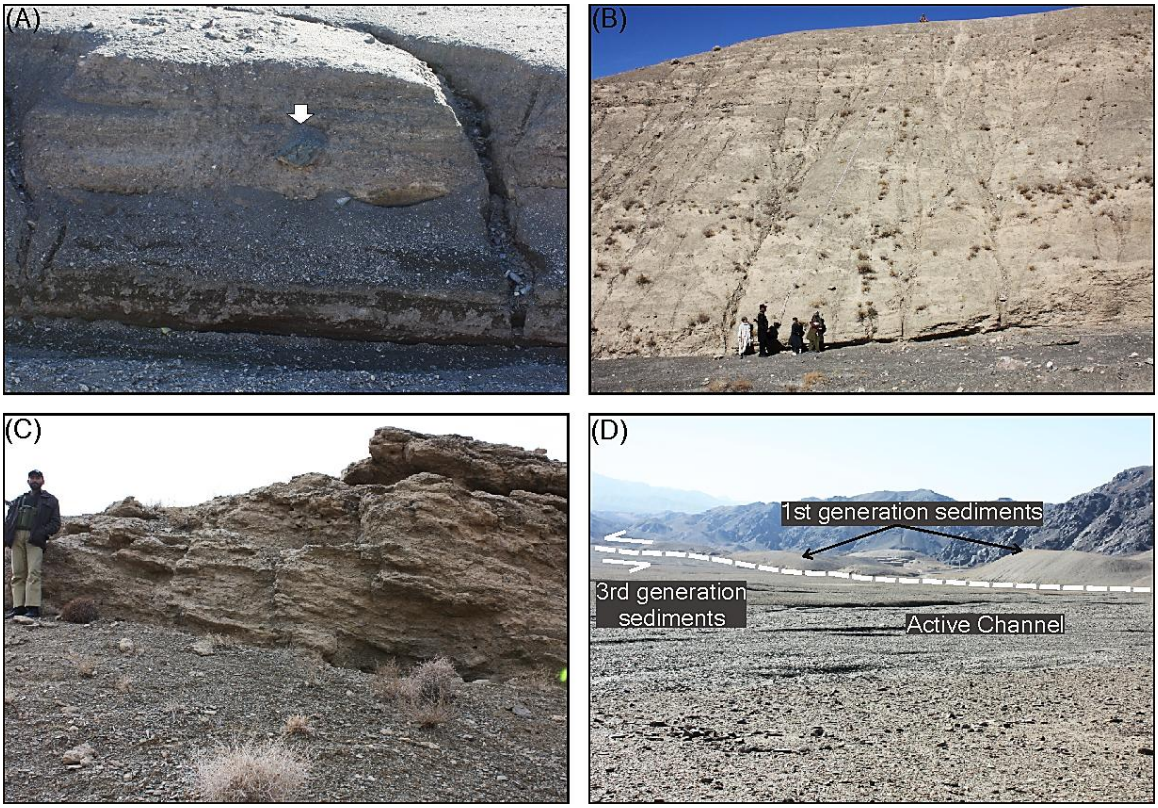

Figure 3.11: Field photographs showing alluvial fans and their sedimentology within the study areas (see Figure 3.8 for location). (A) Typical alluvial fan sediments incised ~ 3.5 m by an ephemeral stream within the Chaman Basin. The sediments comprise mainly shale and sandstone with occasional meter-sized silt-sandstone boulders derived from Khojak Pass Mountains (boulder in the center of the photo is about 60 cm across). (B) Stream cutting exposing about 40 m thick alluvial fan sediments. (C) View of a tilted partially lithified fanglomerate within the oldest alluvial fans proximal to the main Chaman fault. (D) View of typical third generation alluvial fans that overlay part of the Chaman fault. The oldest alluvial fans (1^{st} generation) are present near the base of the mountain front.

active drainage systems. Most of these alluvial fans have experienced little or no erosion and their surfaces are very flat, and are composed of sediment up to a few meters thick. These alluvial fan deposits are not faulted and overly tectonic structures within the study area (Figure 3.11 D). The fourth generation of alluvial fans (mapped as yellow polygons with the third generations of fans in Figure 3.8) is active, representing current streams beds and channel deposits.

3.5.2. Spinatizha fault

The Spinatizha fault is similar to many of the east-southeast dipping second-order structures described by Ruleman et al. (2007) that are mostly west of the main Chaman fault and are the result of both left-lateral slip and convergence on the main Chaman fault. These faults form a set of thrust faults of semi-arcuate shape at the front of the Spinatizha Crystalline Complex (Figure 3.8). In the northern part of the mapped area, the north-south trending Spinatizha fault thrusts crystalline rocks over the Quaternary alluvial fans deposits (this study and Lawrence et al., 1981). In contrast, the Spinatizha fault cut across alluvial fan deposits in the southern part of the study area. These thrust faults represent a growing thrust system that is propagating westward and widening the mountain range that comprises the Spinatizha Crystalline Complex. The pop-up zone, which comprises the Spinatizha Crystalline Complex and the alluvial fan deposits between Chaman and Spinatizha faults, is the hanging wall of the Spinatizha fault and may be the results of fault propagation growth folding. The presence of this thrust is marked by an abrupt change in the drainage pattern within the Chaman Basin. The stream

pattern is dominantly linear and almost parallel between the thrust and the main Chaman fault, but radiate and become braided after traversing the fault (Figure 3.9 B). Individual local highs developed within the thrust block, which mostly deflect the streams around them. Stream deflection is more common in the southern part of the study area where the Spinatizha fault has uplifted the eastern part of the Quaternary alluvial fan surface south of the Spinatizha Crystalline Complex.

3.6. Discussion

The active strand of the Chaman fault system and the resultant Chaman Basin that is examined in this study provides an example of the interaction between growing structures and coevolving landscapes. Drainage patterns and landform/landscape analysis along such evolving structures have been used to examine fold growth and lateral propagation of thrust faults in other regions of the world (e.g., Keller et al., 1999; Owen et al., 1999; Azor et al., 2002; Keller and Pinter, 2002; Scharer et al., 2004; Oskin and Burbank, 2007), but such studies are still rare. This study is the first of its kind along the western margin of the India-Asian collision zone.

The Chaman and Spinatizha faults have a strong impact on the geomorphic expression within the Chaman Basin. The stream pattern in the proximity of the Chaman fault is very distinctive of highly incised and almost parallel streams with well-defined stream banks. Contrary to this is the dominant radiating stream network imprinting the bajadas along the transpression front in a medial position within the Chaman basin (Figure 3.8).

Alluvial streams within the active transpression have overprinted the radiating drainage pattern with the range widening towards the Chaman basin, causing stream quenching. In the mapped area this radiating pattern is intersected by a strike-slip dominant stream pattern in the central part, while in the northern and southern parts away from the main Chaman fault the linear streams become more braided. Climate does affect ephemeral drainage network; however this kind of ephemeral stream behavior is also well documented along growing thrusts and associated folds (e.g. Pearce et al., 2004; Castelltort and Simpson, 2006).

While the Chaman fault left-laterally displaces the streams (Figure 3.9 A) shaping the downstream drainage pattern into a more regularly spaced linear and parallel streams network, the Spinatizha fault perturbs the drainage by increasing the local base level either for the stream to braid after crossing the elevated ground or to deflect locally around the noses of the rising topography (Figures 3.3 and 3.4). This is a common characteristic in such tranpressional settings (Humphrey and Konrad, 2000; Miller and Slingerland, 2006). Thus the longitudinal topographic rise associated with this transpression is the defining factor in shaping the geomorphology within the Chaman Basin.

The northern extreme of the transpression is represented by an ~ 10 km long isolated Roghani ridge that has a steep rise from 1740 m to ~ 2000 m average mean sea level (Figures 3.3 and 3.10 F). The sharp change in relief and highly incised narrow valleys within the deformed Quaternary landforms and Roghani ridge suggest a rapid and active

interaction of the landscaping processes with the active tectonics of growing folds and faults (Burbank et al., 1996; Keller and DeVecchio, 2012). These interactions of alluvial and hillslope processes with the rates and patterns of structural uplift and lateral displacement over considerable time spans are the ultimate variables of shaping the observable drainage patterns and geomorphology (Owen et al., 1999). In addition to the topographic analysis, geomorphic indices of active tectonics, including S_{mf}, V_f, recent stream entrenchment, and SL-gradient index of the ridge and surrounding area, are used to understand the tectonic geomorphology of the area.

3.6.1. Topography, wind and water gaps of the Roghani ridge

The lenticular shaped Roghani ridge is a southwest-verging thrust block oriented NNE-SSW, and is flanked by Quaternary alluvial fan deposits, with its northern and southern noses still rising from below the Quaternary to recently deposited sediment (Figures 3.5 and 3.7). The meta-volcanic rocks comprising the ridge are of upper greenschist facies of the Spinatizha Crystalline Complex (Lawrence et al., 1981). The ridge lies to the west and just south of the gentle double bend in the Chaman fault. The topography reveals a domal shape of the ridge with the highest point at the center of the ridge and plunging both ways towards north and south. Transverse profiling shows a highly asymmetrical ridge with an almost vertical eastern cliff face and a gently sloping western limb (Figure 3.12).

The uplift of the Roghani ridge above the depositional plain has strongly perturbed the local base level. A small aggrading basin has been created in response to this uplifting block between the Roghani ridge and Khojak Pass Mountains with sediment partly concealing the trace of the Chaman fault (Figure 3.11 D). Highly incised and gently west-sloping bajada surrounds the ridge from all sides except east. Most of the drainage flow from the ridge is towards west.

The ridge is dissected by four prominent water gaps and two corresponding wind gaps with streams beds' elevations decreasing from south to north. The water gaps divide the ridge into southern, central, and northern segments, each with different topographies (Figures 3.5 and 3.12). The central and northern water gaps are antecedent streams that have kept their course across this propagating thrust block. The central wind gap is situated ~ 115 m below the highest adjacent point at the top of the thrust block and ~ 77 m above the current stream course (water gap) inferring a total uplift of ~ 77 ± 15 m since the abandonment of the stream.

This wind gap is located south of the water gap and the two are ~ 1348 ± 15 m apart, depicting a southward displacement of the ridge along the Chaman fault. The northern wind gap near the northern nose of the ridge is situated ~ 56 m above the adjacent water gap and ~ 90 m below the adjacent high point at the crest of the thrust block. These two gaps are ~ 450 m apart. Although complex in nature, the presence of wind and water gaps indicate an older drainage network pre-dating the uplift (Simpson, 2004; Miller and Slingerland, 2006; Douglass et al., 2009).

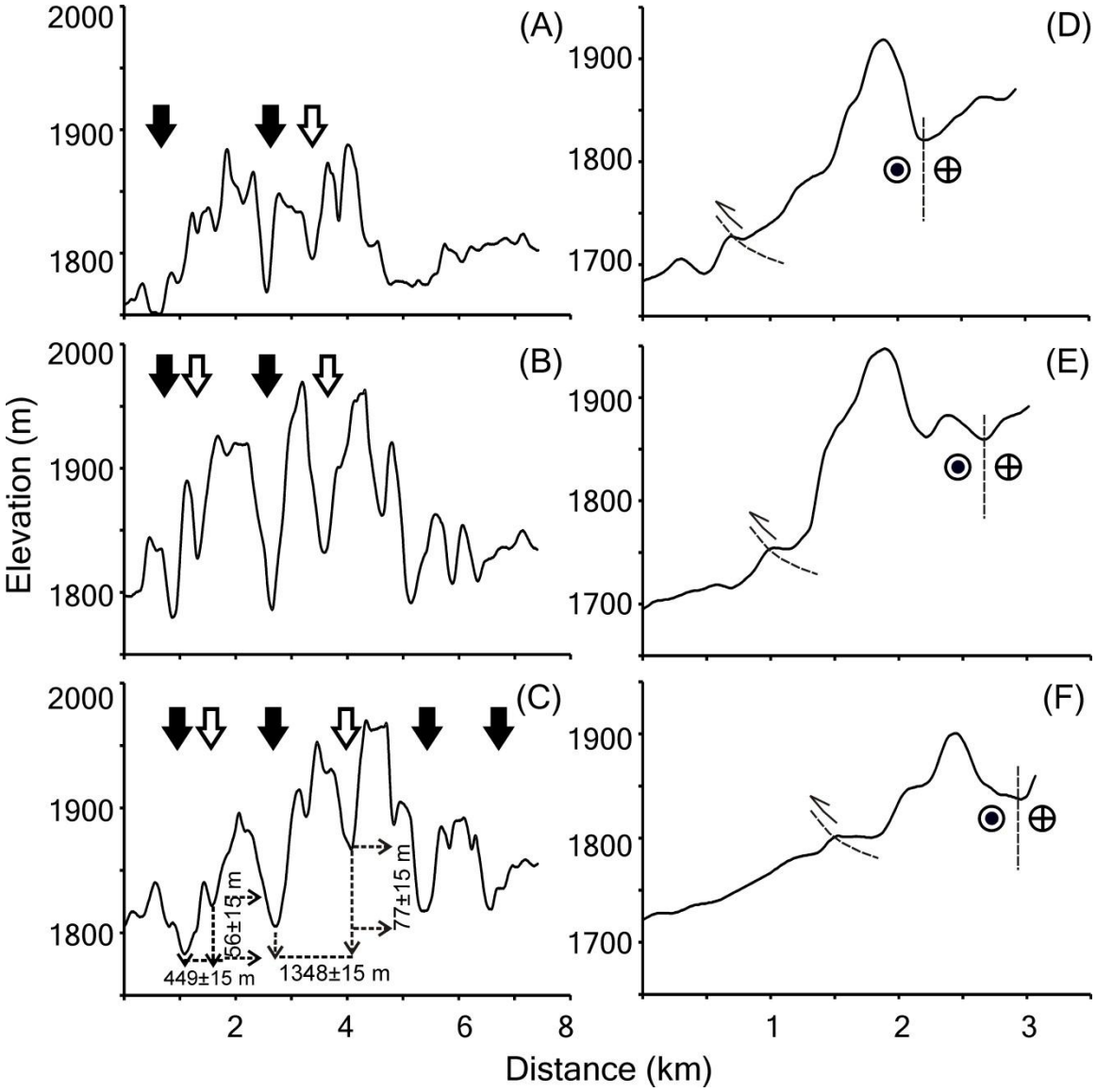

Figure 3.12: Longitudinal (A-C) and transverse (D-F) topographic profiles across the Roghani ridge and surrounding areas. Filled arrows point to water gaps while hollow arrows mark the locations of wind gaps. Note the gradual decrease in wind gaps' elevation from the center of the ridge towards north. The central water gap and corresponding wind gap are 1348 ± 15 m apart, while the wind gap is 77 ± 15 m above the present level of the water gap. Transverse profiles (on the right) with probable locations of Chaman and Spinatizha faults show a highly asymmetrical ridge with an almost vertical eastern ridge front. See Figure 3.5 for the location of the profiles.

With the continued interaction of strike-slip Chaman fault and Spinatizha thrust fault I record: 1) a decrease in topographic relief and decrease in the relief of the wind and water gaps along the direction of growth; 2) diversion of drainage around the tips of the thrust block; 3) lateral displacement of wind and water gaps in the direction of strike-slip movement; and 4) deep incision and deformation of younger deposits.

3.6.2. Bostankaul alluvial fan

The Bostankaul alluvial fan is one of the first-generation (oldest) alluvial fans mapped during this study. This alluvial fan borders the Roghani ridge on east and has an erosional contact with the rocks of the Khojak Pass Mountains on east and is being eroding by an active stream to the south (Figures 3.8 and 3.10 F). In the north, the Bostankaul alluvial fan coalesces with another alluvial fan to form a bajada. In the west where the Bostankaul alluvial fan borders partly the rock of the Roghani ridge, a strand of the Chaman fault cut across the main body of the Bostankaul alluvial fan and displaces it left-laterally (3.11 D). The total displacement, which was measured in the field and from satellite images, is 1150 ± 55 m (Figures 3.5 and 3.7). The southward displaced part of the Bostankaul alluvial fan, which is west of the strand of the Chaman fault, stands high above the present depositional surface and is the only east facing fault scarp present in the study area; however it lies almost at the same elevation as the northward displaced portion of the Bostankaul alluvial fan.

3.6.3. Stream length-gradient index (SL)

SL values were calculated for 134 reaches with a 25 m fixed contour interval along 14 trunk streams that traverse the Roghani ridge and the Chaman fault zone; point values were then interpolated into an SL index map (Table 3.1; Figure 3.13). Analysis of the index map suggests strong tectonic controls rather than bedrock controls on stream gradients. The higher SL index values on the west of the fault suggest recent and continued uplift of the ridge. SL values gradually becoming lower near the Chaman fault zone, which is likely due to shearing and less resistive fault gouge. Lower SL values on the eastern side of the fault zone are due to a comparatively flatter surface with lower gradients.

3.6.4. Valley floor width to valley height ratio (Vf)

V_f values at Roghani ridge were measured at ~ 800 m from the mountain front for three major transverse stream channels (Figure 3.14). Lowest values for the central and northern valleys suggest a higher uplift and incision rate for this part of the ridge as compared to the southern part. Nevertheless the V_f values range from 0.61 to 1.30, which suggests continued and comparatively higher uplift rates of the ridge.

3.6.5. Mountain-front sinuosity (Smf)

The Roghani ridge is bounded by an active fault that tends to generate a straight line front of the ridge opposing the stream erosion, which is cutting through the ridge and forming wind and water gaps to result in a more sinuous western margin of the ridge as compared

to the eastern margin. The S_{mf} value for the ~ 9 km-long western front of the ridge is 1.27 (Figure 3.5), which is in Keller and Pinter's (2002) range (S_{mf} = 1.0-1.6,) for active range bounding fault zones. S_{mf} values calculated along the ridge front encompassing the drainage area of each of the three major water gaps range from 1.23 for the central water gap to 1.32 for the northern water gap.

Table 3.1: Data used in calculating stream length-gradient index data along the fourteen trunk streams used in interpolating the SL-gradient index map shown in Figure 3.13.

S. No	Length of the Reach (ΔL)	Mid point	Mid Point of the reach (long, lat)		Max Cont	Min Cont	Gradient (ΔH)	Upstream Length (L)	SL Index
	Stream-1								
1	2,784.552	1,392	66.394	30.742	1600	1500	100	12966	466
2	2,390.496	1,195	66.415	30.733	1700	1600	100	10378	434
3	1,115.744	558	66.428	30.724	1750	1700	50	8,625	387
4	1,017.718	509	66.437	30.72	1800	1750	50	7,558	371
5	745.773	373	66.445	30.715	1850	1800	50	6,676	448
6	565.454	283	66.45	30.713	1900	1850	50	6,021	532
7	745.185	373	66.456	30.711	1950	1900	50	5,365	360
8	602.204	301	66.461	30.708	2000	1950	50	4,692	390
9	498.486	249	66.466	30.706	2050	2000	50	4,141	415
10	164.652	82	66.467	30.703	2100	2050	50	3,810	1157
11	480.249	240	66.468	30.701	2150	2100	50	3,487	363
12	456.099	228	66.472	30.699	2200	2150	50	3,019	331
13	531.379	266	66.475	30.695	2250	2200	50	2,526	238
14	230.623	115	66.477	30.692	2300	2250	50	2,145	465
15	326.939	163	66.478	30.691	2350	2300	50	1,866	285
16	211.026	106	66.479	30.688	2400	2350	50	1,597	378
17	613.688	307	66.481	30.685	2450	2400	50	1,184	96
18	1,333.043	667	66.479	30.679	2475	2450	25	211	4
	Stream-2								
1	2,756.167	1,378	66.411	30.76	1600	1500	100	11935	433
2	2,350.545	1,175	66.432	30.748	1700	1600	100	9390	399
3	989.390	495	66.445	30.739	1750	1700	50	7,720	390
4	858.177	429	66.454	30.737	1800	1750	50	6,796	396
5	1,397.511	699	66.463	30.732	1850	1800	50	5,668	203
6	973.126	487	66.469	30.728	1900	1850	50	4,483	230
7	464.206	232	66.468	30.723	1950	1900	50	3,764	405
8	572.297	286	66.47	30.719	2000	1950	50	3,246	284
9	517.739	259	66.474	30.716	2050	2000	50	2,701	261
10	477.223	239	66.478	30.714	2100	2050	50	2,203	231
11	392.533	196	66.481	30.712	2150	2100	50	1,769	225
12	240.196	120	66.483	30.709	2200	2150	50	1,452	302
13	422.192	211	66.484	30.707	2250	2200	50	1,121	133
14	219.771	110	66.485	30.704	2300	2250	50	800	182
15	687.109	344	66.488	30.702	2500	2300	200	347	101

S. No	Length of the Reach (ΔL)	Mid point	Mid Point of the reach (long, lat)		Max Cont	Min Cont	Gradient (ΔH)	Upstream Length (L)	SL Index
	Stream-3								
1	2,842.029	1,421	66.422	30.77	1600	1500	100	9,566	337
2	2,433.619	1,217	66.439	30.755	1700	1600	100	6,928	285
3	1,096.408	548	66.453	30.746	1750	1700	50	5,163	235
4	854.084	427	66.462	30.744	1800	1750	50	4,188	245
5	1,013.872	507	66.469	30.74	1850	1800	50	3,254	160
6	635.640	318	66.477	30.739	1900	1850	50	2,429	191
7	543.373	272	66.482	30.738	1950	1900	50	1,840	169
8	375.080	188	66.483	30.735	2000	1950	50	1,380	184
9	629.541	315	66.486	30.732	2050	2000	50	878	70
10	572.709	286	66.49	30.728	2175	2050	125	277	60
	Stream-4								
1	2,978.262	1,489	66.438	30.781	1600	1500	100	9838	330
2	1,478.086	739	66.455	30.772	1700	1600	100	7609	515
3	1,032.927	516	66.467	30.769	1750	1700	50	6,354	308
4	799.374	400	66.474	30.764	1800	1750	50	5,438	340
5	717.714	359	66.48	30.761	1850	1800	50	4,679	326
6	634.855	317	66.481	30.756	1900	1850	50	4,003	315
7	832.686	416	66.485	30.75	1950	1900	50	3,269	196
8	575.216	288	66.491	30.747	2000	1950	50	2,565	223
9	614.534	307	66.494	30.743	2050	2000	50	1,970	160
10	387.529	194	66.496	30.739	2100	2050	50	1,469	190
11	390.462	195	66.499	30.736	2150	2100	50	1,080	138
12	288.155	144	66.5	30.734	2200	2150	50	741	129
13	421.184	211	66.503	30.732	2350	2200	150	386	138
	Stream-5								
1	2605.924	1,303	66.445	30.792	1600	1500	100	9399	361
2	1926.694	963	66.465	30.786	1700	1600	100	7132	370
3	909.415	455	66.478	30.783	1750	1700	50	5,714	314
4	914.954	457	66.485	30.778	1800	1750	50	4,802	262
5	566.465	283	66.492	30.778	1850	1800	50	4,062	358
6	617.314	309	66.495	30.774	1900	1850	50	3,470	281
7	681.771	341	66.499	30.769	1950	1900	50	2,820	207
8	527.332	264	66.504	30.767	2000	1950	50	2,216	210
9	517.234	259	66.509	30.764	2050	2000	50	1,693	164
10	517.937	259	66.513	30.764	2100	2050	50	1,176	113

Table 3.1 continues on next page.

S. No	Length of the Reach (ΔL)	Mid point	Mid Point of the reach (long, lat)		Max Cont	Min Cont	Gradient (ΔH)	Upstream Length (L)	SL Index
11	684.669	342	66.519	30.762	2200	2100	100	574	84
	Stream-6								
1	2,479.581	1,240	66.452	30.8	1600	1500	100	8,675	350
2	1,796.115	898	66.47	30.793	1700	1600	100	6,537	364
3	936.936	468	66.483	30.79	1750	1700	50	5,171	276
4	730.505	365	66.491	30.788	1800	1750	50	4,337	297
5	688.877	344	66.498	30.786	1850	1800	50	3,627	263
6	597.105	299	66.503	30.784	1900	1850	50	2,984	250
7	611.765	306	66.508	30.782	1950	1900	50	2,380	195
8	482.664	241	66.513	30.78	2000	1950	50	1,833	190
9	451.649	226	66.518	30.779	2050	2000	50	1,366	151
10	349.965	175	66.52	30.776	2100	2050	50	965	138
11	505.431	253	66.524	30.775	2200	2100	100	537	106
	Stream-7								
1	2,552.860	1,276	66.474	30.822	1600	1500	100	7,884	309
2	1,568.444	784	66.484	30.808	1700	1600	100	5,823	371
3	810.858	405	66.491	30.8	1750	1700	50	4,633	286
4	565.048	283	66.498	30.798	1800	1750	50	3,945	349
5	485.094	243	66.502	30.796	1850	1800	50	3,420	353
6	503.763	252	66.506	30.793	1900	1850	50	2,926	290
7	770.913	385	66.511	30.779	1950	1900	50	2,288	148
8	485.511	243	66.515	30.786	2000	1950	50	1,660	171
9	553.407	277	66.518	30.782	2050	2000	50	1,141	103
10	740.474	370	66.524	30.782	2175	2050	125	494	83
	Stream-8								
1	2,602.732	1,301	66.485	30.836	1600	1500	100	6,381	245
2	2,076.390	1,038	66.501	30.823	1700	1600	100	4,041	195
3	779.399	390	66.508	30.813	1750	1700	50	2,613	168
4	590.754	295	66.509	30.808	1800	1750	50	1,928	163
5	540.096	270	66.515	30.805	1850	1800	50	1,363	126
6	511.620	256	66.518	30.803	1900	1850	50	837	82
7	431.164	216	66.52	30.8	1950	1900	50	366	42
	Stream-9								
1	2,676.575	1,338	66.486	30.838	1600	1500	100	8,926	333
2	2,281.426	1,141	66.504	30.825	1700	1600	100	6,447	283
3	897.805	449	66.519	30.823	1750	1700	50	4,858	271

Table 3.1 continues on next page.

S. No	Length of the Reach (ΔL)	Mid point	Mid Point of the reach (long, lat)		Max Cont	Min Cont	Gradient (ΔH)	Upstream Length (L)	SL Index
4	868.661	434	66.525	30.817	1800	1750	50	3,974	229
5	673.090	337	66.531	30.813	1850	1800	50	3,204	238
6	711.767	356	66.535	30.808	1900	1850	50	2,511	176
7	618.742	309	66.541	30.805	1950	1900	50	1,846	149
8	341.976	171	66.543	30.802	2000	1950	50	1,366	200
9	499.917	250	66.545	30.799	2050	2000	50	945	94
10	581.333	291	66.546	30.794	2150	2050	100	404	69
	Stream-10								
1	864.878	432	66.473	30.731	1950	1850	100	3,634	420
2	681.390	341	66.477	30.726	2000	1950	50	2,861	210
3	898.790	449	66.484	30.721	2100	2000	100	2,071	230
4	844.595	422	66.491	30.719	2200	2100	100	1,199	142
5	628.983	314	66.496	30.714	2400	2200	200	463	147
	Stream-11								
1	1,258.016	629	66.487	30.757	1950	1850	100	3,074	244
2	591.277	296	66.496	30.756	2050	1950	100	2,149	363
3	988.137	494	66.502	30.753	2150	2050	100	1,359	138
4	441.937	221	66.509	30.752	2200	2150	50	644	73
	Stream-12								
1	2,989.332	1,495	66.4091	30.7280	1700	1600	100	4,334	145
2	1,840.145	920	66.4231	30.7145	1800	1700	100	1,919	104
3	905.261	453	66.4354	30.7087	1875	1800	75	546	45
	Stream-13								
1	2,442.101	1,221	66.3807	30.7263	1600	1500	100	12,262	502
2	2,398.193	1,199	66.4017	30.7200	1700	1600	100	9,842	410
3	2,205.372	1,103	66.4197	30.7100	1800	1700	100	7,540	342
4	1,539.295	770	66.4347	30.7046	1900	1800	100	5,668	368
5	1,146.525	573	66.4467	30.6998	2000	1900	100	4,325	377
6	1,402.377	701	66.4547	30.6941	2100	2000	100	3,050	218
7	811.173	406	66.4633	30.6892	2200	2100	100	1,943	240
8	591.084	296	66.4680	30.6849	2300	2200	100	1,242	210
9	519.592	260	66.4710	30.6808	2400	2300	100	687	132
	Stream-14								
1	2,270.107	1,135	66.3728	30.7064	1600	1500	100	11,750	518
2	1,885.611	943	66.3936	30.7067	1700	1600	100	9,672	513
3	1,834.930	917	66.4112	30.7012	1800	1700	100	7,812	426

Table 3.1 continues on next page.

S. No	Length of the Reach (ΔL)	Mid point	Mid Point of the reach (long, lat)		Max Cont	Min Cont	Gradient (ΔH)	Upstream Length (L)	SL Index
4	1,657.761	829	66.4242	30.6918	1900	1800	100	6,066	366
5	1,806.482	903	66.4388	30.6855	2000	1900	100	4,334	240
6	629.834	315	66.4505	30.6850	2100	2000	100	3,115	495
7	1,222.377	611	66.4590	30.6815	2200	2100	100	2,189	179
8	486.946	243	66.4655	30.6773	2300	2200	100	1,335	274
9	468.033	234	66.4678	30.6736	2400	2300	100	857	183

Table 3.1 continued.

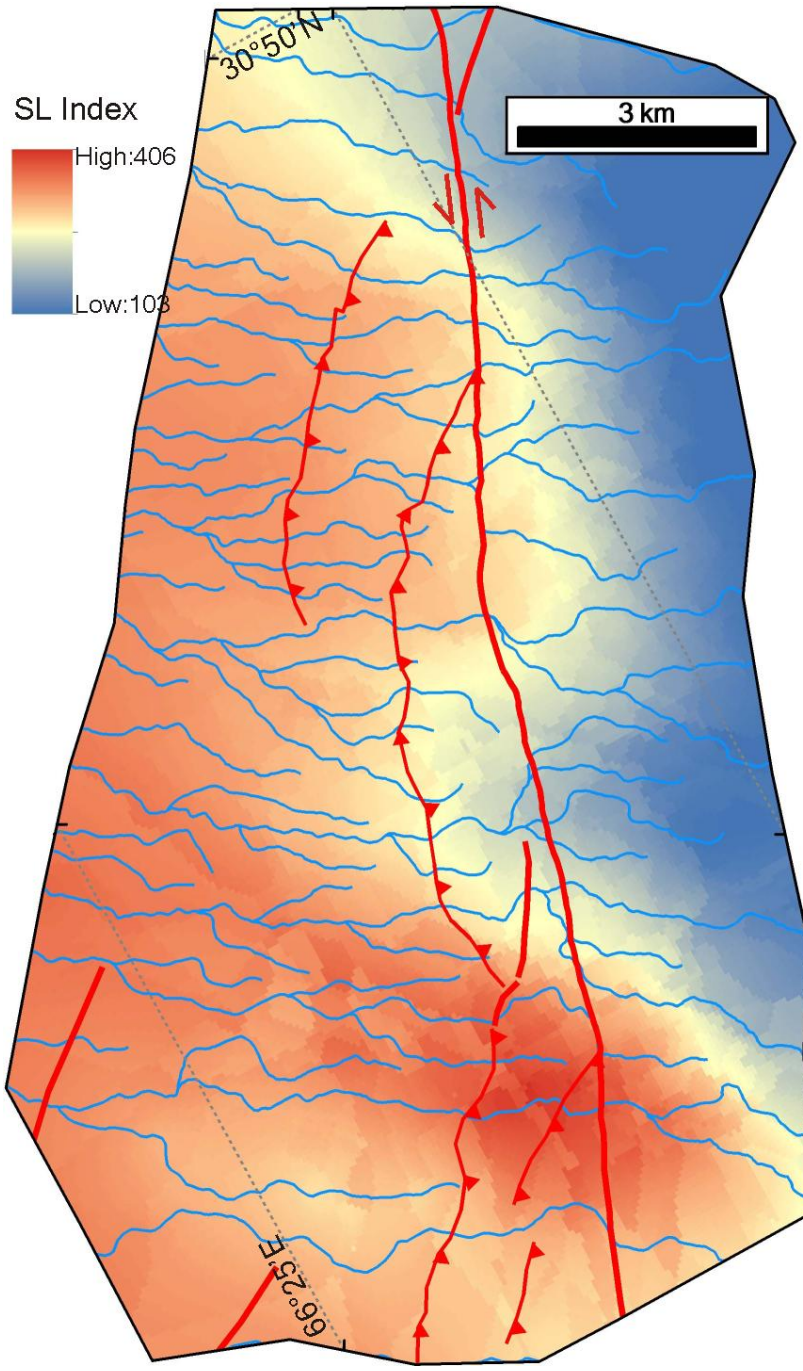

Figure 3.13: Stream length-gradient index map of the area based on stream length-gradient index values from 14 transverse trunk streams that cross the Roghani ridge and fault zone; see Figure 3.2 for the location of streams and structures. Higher SL-gradient index values on the west of the fault suggest recent uplift. The lower values in the fault zone are due to shearing and less resistive fault gouge.

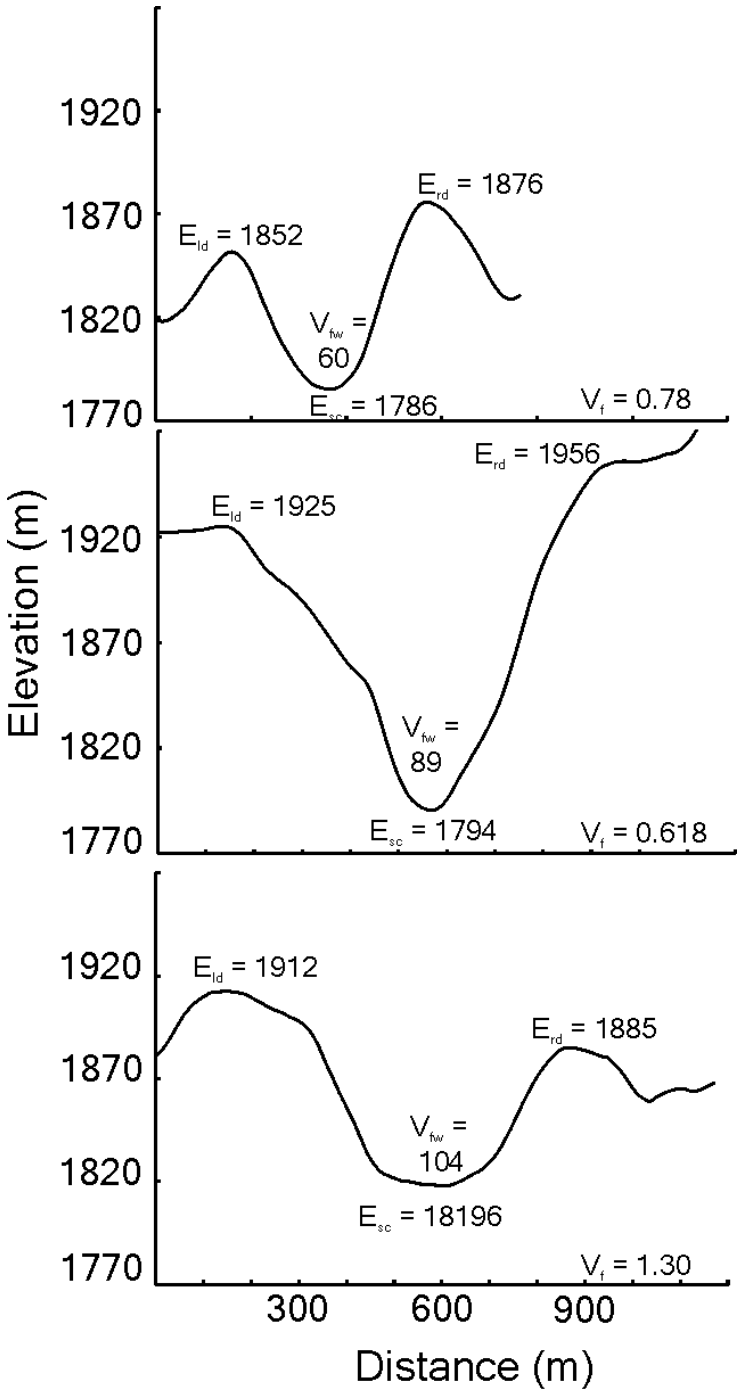

Figure 3.14: Valley floor width to height ratios (V_f) for the three antecedent streams from north to south (see Figure 3.5 for the locations of measured streams) recording a general trend of higher uplift in the northern portion of the ridge with maximum at its center. V_f values range from 1.30 in the south to 0.61 in the north.

3.6.6. Entrenchment (E)

E values calculated from 8 different streams at an average distance of 1.5 km from the Roghani ridge front vary from ~ 1 m of entrenchment to almost 6 m. The central part of the ridge has slightly lower E values than the southern and northern stretches, which suggest higher tectonics activity at the ends of the ridge (Figure 3.15). However, the overall E values of 1-6 m resemble a comparatively highly active tectonic regime (Azor et al., 2002). S_{mf}, V_f, and E values are also consistent with lateral propagation of the ridge. SL and E values are consistent with the progressive and continued deformation of the recent deposits. These values demonstrate higher uplift rates at the center and southern segments of the ridge in contrast to northern segment that is consistent with the topographic relief of the ridge and the relief of the water and wind gaps that decreases towards north along the ridge.

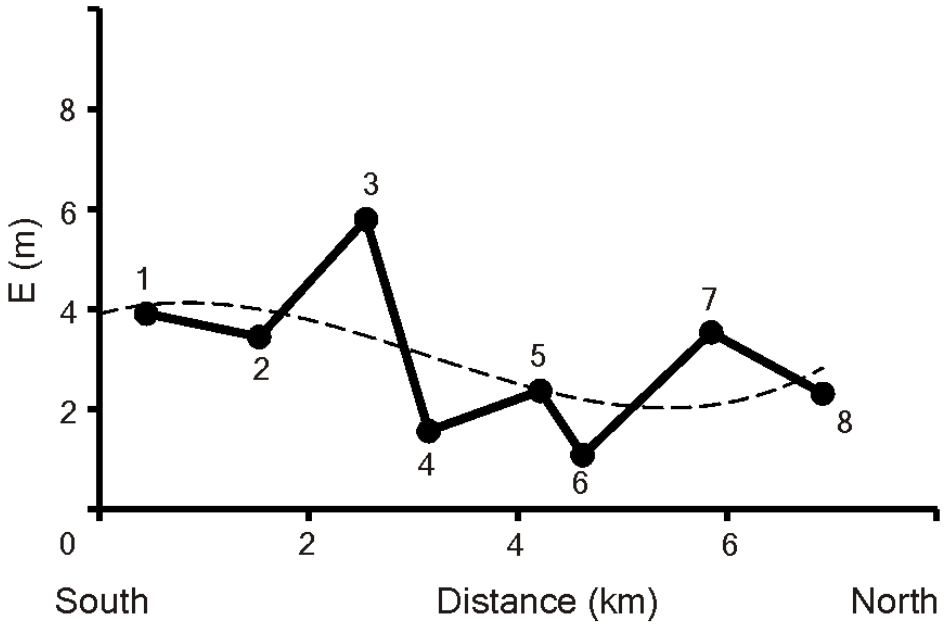

Figure 3.15: E values along the western front of the Roghani ridge, calculated for 8 streams with more than 50 m width at an average distance of 1.5 km from the mountain front. E values of 1-6 m resemble a recently uplifted thrust block. Location of points 1 through 8 is shown in Figure 3.5.

3.6.7. Tectonic implications

The separation and relief difference of the consecutive wind and water gaps coupled with displaced Bostankaul alluvial fan can be used to estimate the Late Quaternary slip rates along this fault system. The lateral displacement of 1150 ± 55 m recorded by the Bostankaul alluvial fan surface is in agreement with the 1348 ± 15 m separation between the central water gap and the corresponding wind gap. I interpret that this segment of the Chaman fault has moved ~ 1150 m since the abandonment of the Bostankaul alluvial fan surface. In addition, the topographic difference of 77 ± 15 m between the present day water and the wind gaps has recorded the dip slip component of this evolving transpression comprising Chaman and Spinatizha faults. Figure 3.16 summarizes present-day structural setup of this transpression and the resulting landscape and its evolution can be attributed to the presence of a half positive flower structure, which is a common structure along bends in the continental strike-slip faults (Mann, 2007).

Most of the slip rate (~ 30 mm/yr) resulting from the relative moment of Indian and Eurasian plates in this region is accommodated along the Chaman fault (Sella et al., 2003). However, the difference in azimuths of the strike of the Chaman fault (~ N 34°) and the Indian plate relative moment (N 12° E) essentially requires some convergence within the Indian plate boundary zone (Molnar and Dayem, 2011). The resultant convergence from this geometric setup in the Indian plate boundary zone has caused the formation of the Suliman-Kirthar (SK) fold-thrust belt (Figure 3.1).). A slip partitioning rate of ~ 3 – 13 mm/yr is estimated along several thrust faults present within the SK fold-thrust belt zone using the last 200 years earthquake data of the region (Ambraseys and

Bilham, 2003; Szeliga et al., 2009). The Spinatizha thrust fault is one of the several thrusts may account for this convergence within the boundary. Based on the topographic analysis I make a generalized estimation of the strike-slip and dip-slip component for this system. Morphostratigraphy of the alluvial fan deposits around the Roghani ridge I estimate that the alluvial fan surfaces of the Qf1 fan generation that surrounds the ridge are of the same age. Since the abandonment of these alluvial fan surfaces is contemporary with the stream deflection of the central water gap and consequent development of the associated water gap (Figure 3.12) I assume the total lateral displacement of the Bostankaul alluvial fan and the vertical uplift of the central water gap as time equivalent. Consequently the ~ 1150 m left-lateral displacement along the Chaman fault is time equivalent to the ~ 77 m uplift of the wind gap. This concludes that since the abandonment of the Bostankaul alluvial fan surface the Chaman fault has moved ~ 1150 m left-laterally while uplift along the Spinathizha thrust accounts for ~ 77 m in the same time period giving an estimate of ~ 14 m to 1 m of strike-slip to the thrust movement. Although a subsidiary of the Chaman fault system this thrust does provide the opportunity to understand the strain partitioning along the plate boundary and estimate the convergence rate of the Indian plate.

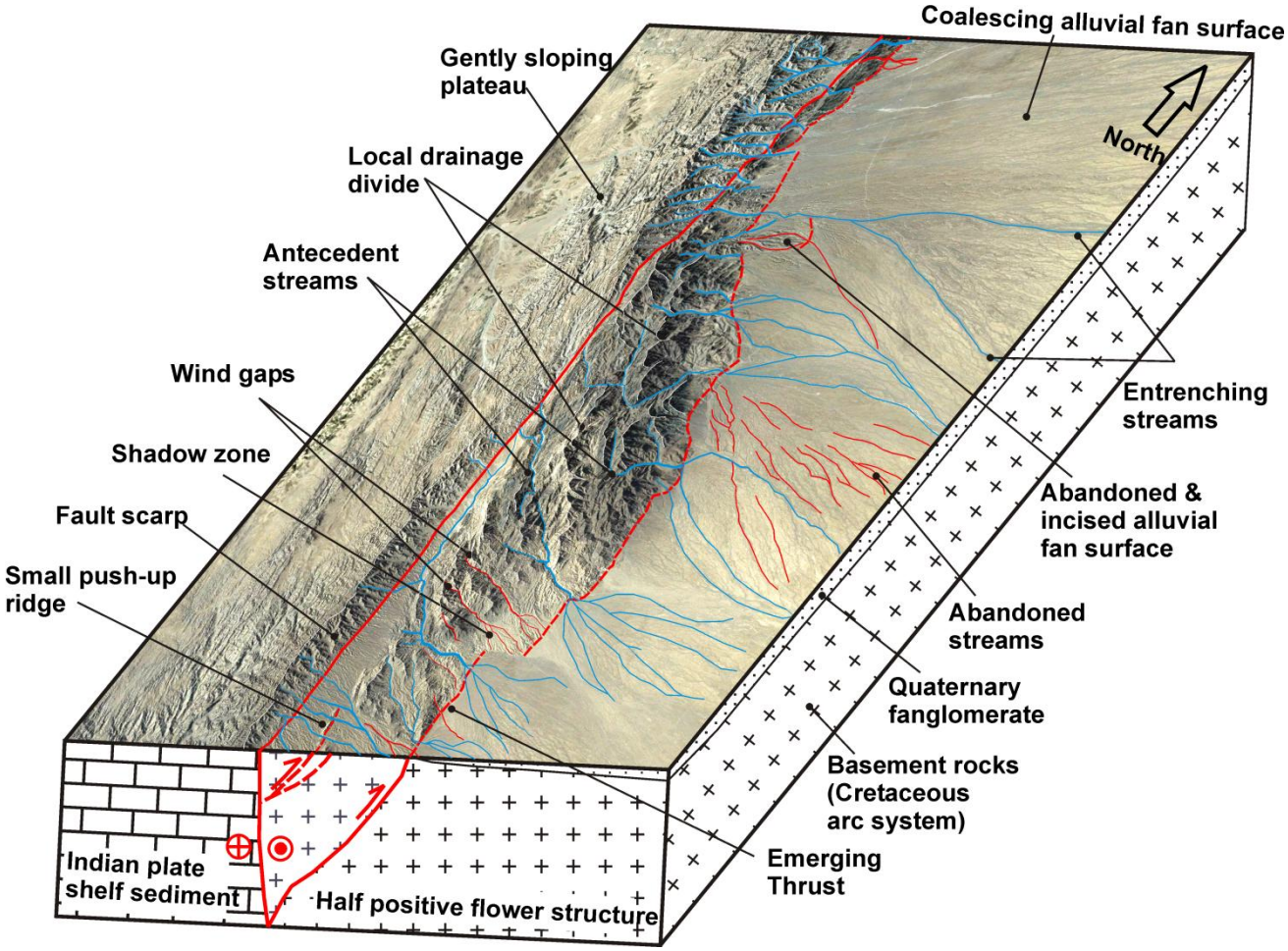

Figure 3.16: Block diagram showing major typical landforms and topography expected along a gently restraining bend in curvature of a left-lateral strike-slip fault. Structures from a Google Earth image covering a part of the Chaman fault are speculated from the surface downward making a half-positive flower structure.

3.7. Conclusions

The Roghani ridge and Bostankaul alluvial fan is an evolving landscaping system representing simultaneous interaction of active tectonics and erosional processes. The abandoned alluvial fan surface is deeply incised by narrow V-shaped valleys and is left-laterally displaced along an active segment of the Chaman fault. While the asymmetrical Roghani ridge, with a steep eastern cliff face and a gently sloping western limb, is formed on the hanging wall of the southeast dipping Spinatizha thrust fault. Topographic and geomorphic characteristics of the ridge indicate a northward lateral growth of the Spinatizha fault as a subsidiary of the Chaman fault. Geometric setup of the wind and water gaps in the ridge supports the northward uplift of the ridge and lengthening of the Spinatizha thrust fault. The indices of active tectonics also prove a progressive and continued activity of this thrust fault. The Spinatizha thrust fault represents one of the several transpressions present along the Chaman fault that compensate for the convergence required by the difference in azimuths of the strike of the Chaman fault and the relative motion of Indian and Eurasian plates.

Chapter 4 : Slip rates along the Chaman fault: implication for transient strain accumulation or fault inversion and strain partitioning along the western Indian plate margin

4.1. Abstract

The Chaman fault in Western Pakistan marks the western collision boundary between Indian and Eurasian plates and connects the Makran subduction zone to the Himalayan convergence zone. Geomorphic-scale slip rates along an active strand of the Chaman fault are added to the sporadic data set of this poorly investigated transform system. Field investigations coupled with high-resolution GeoEye-1 satellite data of an alluvial fan surface (Bostankaul alluvial fan) show ~ 1150 m left-lateral offset by the fault since the abandonment of the surface. An exposure weighted mean ^{10}Be age of ~ 34.8 kyr on the Bostankaul alluvial surface yields a slip rate of 33.3 ± 3.0 mm/yr. This rate agrees with the geologically constrained slip rates along the Chaman fault, but is approximately twice as larger than that inferred from the decade-long global positioning system measurements of 18 ± 1 mm/yr. The contrast in geomorphic and geodetic slip rates along the Chaman fault, like other major intra-continental strike-slip faults, has two major implications: 1) transient variations in rates of elastic strain accumulation, such that the geodetic rates might represent a period of reduced displacement as compared to the averaged Late Pleistocene rate; or 2) strain partitioning within the plate boundary zone. While strain partitioning could be the reason of slip-rate variations within the western Indian plate boundary zone, transient strain accumulation could explain contrasting slip rates along the Chaman fault, which is late in its seismic cycle.

4.2. Introduction

Understanding of the dynamics of large-scale intracontinental deformation is influenced by the two end-member views of: 1) highly localized deformation with the lithosphere deforming as a rigid plate (Peltzer and Tapponnier, 1988; Avouac and Tapponnier, 1993; Peltzer and Saucier, 1996; Tapponnier et al. 2001; Meade, 2007; Thatcher, 2007); and 2) regionally distributed, continuous deformation with the lithosphere deforming in a fluid-like fashion (Molnar and Tapponnier, 1975; England and Houseman, 1986; Bendick et al., 2000; Zhang et al., 2007). The preeminent Himalayan-Tibetan orogeny provides the opportunity to test these two hypotheses with the advancement in the ability to measure deformation at shorter timescales using the techniques of GPS/InSAR and the ability to date Late Quaternary landforms and sediments using numerical dating including terrestrial cosmogenic nuclides (TCN) and ^{14}C methods. The plate-bounding crustal-scale strike slip faults within the orogen are the center of such studies. Rigid-plate localized deformation supports high long-term (10^3–10^6 years) geomorphic slip rates (Van der Woerd et al., 1998; 2000; Tapponnier et al. 2001; Mériaux et al., 2004; 2005; Chevalier et al., 2005) while diffused deformation is supported by relatively low short-term (10^0-10^1 years) geodetic slip rates along these major strike-slip faults (Bendick et al., 2000; Chen et al., 2000; Shen et al., 2001; Phillips et al., 2004; England and Molnar, 2005).

Defining the temporal and spatial distribution of strain along plate boundaries is challenging, but is essential for developing and testing tectonic models. This is particularly so for the Himalayan-Tibetan orogen, which is one of the most logistically and politically difficult regions to study, yet ideal for examining the nature and dynamics

of continent-continent collision. In brief, the Himalayan-Tibetan orogen is a consequence of the collision of the Indian and Eurasian continental lithospheres (Yin and Harrison, 2000). As such, underthrusting of the Indian plate beneath the Himalaya accommodates around half (Thatcher, 2007) of its 36 – 45 mm/yr northward movement (Klootwijk et al., 1998; Molnar and Stock, 2009), but much of the remaining movement is adjusted within the Tibet plateau either localized along the crustal-scale strike-slip faults (Tapponnier et al., 2001) or distributed within the blocks bounded by these mega strike-slip faults (England and Molnar, 2005). While many studies (Bendick et al., 2000; Chevalier et al., 2005; He and Chéry, 2008; Wright et al., 2004) have focused on understanding the deformation along these mega-structures in the Himalaya and Tibet, little focus has been given to the western Indian plate boundary, which is largely defined by the Chaman transform fault system (Figure 4.1). Little focus has been placed on the Chaman fault because it was thought that Chaman fault is not playing any significant role in taking up shortening between India and Asia and partially due to its location in a geographic region of civil unrest.

Recent GPS and InSAR studies on the Chaman fault yield slip rates of 18 ± 1 mm/yr (Mohadjer et al., 2010) and a post-seismic slip rate of ~ 8 mm/yr (Furuya and Satyabala, 2008; Figure 4.1; Table 4.1). In contrast, Lawrence et al. (1992) provided a geologically (> 10^6 years timescale) constrained displacement of 460 ± 10 km, which was based on four tentatively observed regionally displaced features including: 1) presence of a major thrust fault laterally displaced for ~ 250 km on both sides of the Chaman fault; 2) correlation of subduction complexes present on both sides of the fault; 3) the depression

250 km
Strike-slip fault
Thrust fault
Shear zone
5 mm/yr
Eurasian Plate
MBT
HF
KoF
PS
MBT
GF
MF
CF
SK
Afghan Block
GBF
Indian Plate
36 - 45 mm/yr
ONF
Makran Subduction Zone
35° N
30° N
65° E
70° E
(A)
31.0° N
Chaman Town
Fig. 2
Bostankaul Alluvial Fan
Roghani Ridge
Chaman Basin
Helmand Desert
Spinatizha thrust fault
SCC
Chaman Fault
Khojak Pass Mountains
Pakistan
Afghanistan
30.0° N
66.0° E
20 km
(B)

Figure 4.1: Tectonic framework of the northwestern Indian Plate margin and Eurasia. Major active strike-slip faults, thrusts and suture zones (modified after Mohadjer et al., 2010; Khan et al., 2009) are displayed on SRTM elevation data. Blue arrows show GPS velocities with respect to fixed Eurasian plate/Afghan block (Mohadjer et al., 2010). The blue box is the position of Synthetic Aperture Radar (SAR) data used in InSAR studies (Furuya and Satyabala, 2008). Notice the azimuth of the Indian plate motion (N12°E) against the average N34°E azimuth of the strike of the CF is responsible for the strain partitioning in the Suliman-Kirthar Fold-thrust Belt (SK). The yellow rectangle shows position of part B. GF: Gardiz Fault; HF: Herat Fault; KoF: Konar Fault; MBT: Main Boundary Thrust; MF: Mokur Fault; MPT: Main Pamir Thrust; ONF: Ornach-Nal Fault; PS: Panjao shear. (B) Central section of the Chaman fault (CF) in western Pakistan shown on an Advanced Spaceborne Thermal Emission and Reflection Radiometer (ASTER) image (bands 1-3-2 displayed as RGB). The gentle bend in strike of the CF just north of the present study area helps create the Spinatizha thrust fault and the transpression uplifting the Spinatizha Crystalline Complex (SCC), and a part of the alluvial fan complex of the Chaman basin (Center of the map). The yellow box shows the location of the Bostankaul alluvial fan and Roghani Ridge in Figure 4.2.

Table 4.1: A compilation of previously reported offsets and slip rates along the Chaman fault.

Slip rate (mm/yr)	Location	Methods/Features used	Reference
08.0	31.96°N, 67.55°E	InSAR (a Mw 5.0 earthquake, Oct. 21, 2005)	Furuya and Satyabala, 2008
18 ± 1	Northern segment where Chaman fault bifurcates in to two strands	GPS observations over a seven years' time period	Mohadjer et al., 2010
19 – 24	Central segment of the fault from 29° N to 35° N near Chaman	Matching four features displaced along the fault	Lawrence et al., 1992
25 – 35	Northern segment of the fault in Afghanistan	~ 80 km displacement in a 2 Ma old volcanic unit and extrapolating the rate to the Chaman fault	Beun et al., 1979

of the Kharan desert south of the Ras Koh is equivalent to that of the Ab-e-Istada depression south of the Gardez fault, and (4) the sediment of the eastern Makran Ranges is equivalent to the sediment of the Katawaz Basin. These implied an average slip rate of 19 – 24 mm/yr since the inception of the strike-slip motion on the Chaman fault from 25 – 20 Ma (Lawrence et al., 1992). While Beun et al. (1979) extrapolated the offset of ~ 60 – 80 km along a north-south fault in a volcanic unit dated at ~ 2 Ma to the Chaman fault estimating a slip rate of 25 – 35 mm/yr. I present here the first ^{10}Be TCN surface exposure ages ever reported on a displaced alluvial fan, the Bostankaul alluvial fan (Figure 4.1 B), along the Chaman fault to provide geomorphic rates of displacement and further insight on the evolution and recent strain accumulation along the western Indian plate boundary zone. The definitive detection, and explanation, between short-term geodetic slip rates and those based on longer timescale geomorphic and geologic observations is a key in tectonic studies, and also has major implications for seismic hazard assessment.

4.3. Fault displacement and TCN ages

4.3.1. Regional setting

The Bostankaul alluvial fan is located within the Chaman Basin near the village of Bostankaul (30.75^{o}N/66.48^{o}E at ~ 2000 m above average mean sea level) and is morpho-stratigraphically among the oldest alluvial fans displaced by the Chaman fault (Figures 4.1 B and 4.2). The Chaman Basin is a ~ 80 x 20 km arc-shaped asymmetrical alluvial basin fed by a moderate to highly incised, discontinuous ephemeral stream network. The basin formed in response to uplift of the eastern block of the Chaman fault and is the depositional site for sediments derived from the Khojak Pass Mountains, which makes a part of the eastern block of the Chaman fault (Figure 4.1 A). The Khojak Pass Mountains comprise a part of the Tertiary Katawaz Basin, which was a remnant of the Neo-Tethys ocean basin prior to the collision of the Indian plate with the Afghan block and mainly filled with Tertiary deltaic to submarine fan sediment and late-stage molasse (Qayyum et al., 1996). The Helmand desert flanks the western side of the Chaman Basin, while two unnamed basins define the northern and southern ends of the Chaman Basin. The southern half of the Chaman basin is delimited by a complex transpressional structure along the eastern boundary of the basin, which comprises the Chaman strike-slip and the second order Spinatizha thrust faults (Figure 4.1 A). The pop-up zone within the transpressional structure is composed of the Spinatizha Crystalline Complex (SCC), a sliver from a pre- to syn-collision Cretaceous Chaghai-Kandahar arc system that was present on the southeastern boundary of Eurasia (Lawrence et al., 1981, 1992), and an alluvial fan surface uplifted along the Spinatizha fault.

4.3.2. Offset

4.3.2.1. Bostankaul Alluvial Fan Site

The displaced Bostankaul alluvial fan was mapped in the field trip and by using GeoEye-1 imagery. At this site the Bostankaul alluvial fan (whose surface and sediments were map as Qf1) overlies the rocks of the Khojak Pass Mountains to the east and is terminated to the west by a faulted contact with Roghani ridge (the northern most extreme of the SCC; Figure 4.2). In the south, the Bostankaul alluvial fan has an erosional contact with a younger generation of alluvial fans (mapped as Qf3), while in the north, the main part of the Bostankaul alluvial fan coalesces with another displaced alluvial fan of approximately the same age forming a bajada. On the west side of the Chaman fault, where the Bostankaul alluvial fan borders the rocks of the Roghani Ridge, the Chaman fault traverses the main body of the alluvial fan and displaces it left-laterally. The southward-displaced part of the alluvial fan stands high up to ~ 15 - 30 m above the present depositional surface and is the only east-facing fault scarp that is present within the study area (Figure 4.3); however, on average this part of the alluvial fan lies almost at the same topographic level (~ 1850 – 1900 m elevation) as the northward-displaced portion of the Bostankaul alluvial fan that lies east of the Chaman fault (Figures 4.4, 4.5, 4.6, and 4.7).

The Bostankaul village which resides on a low lying southern margin of the Bostankaul alluvial fan present between the Khojak Pass Mountains and Roghani Ridge is the site where I measured displacement along a strand of the Chaman fault. The alluvial surface

1,000 m
N
30° 45' N
66° 28' E
(A)
1,000 m
N
B
1
1
2
2
3
4
NBK-5
NBK-2
NBK-1
NBK-3
NBK-4
A
BK-3
BK-1
Fig. 3
RG-2
Index
Chaman Fault
Spinatizha Fault
Sample Location
Qf3
Qf2
Qf1
Khujak Pass Range
Spinatizha Cryst. Complex
(B)

Figure 4.2: Geology and geomorphology around the Roghani Ridge and Bostankaul alluvial fan. (A) GeoEye-1 satellite image (Red- Green-Blue) of the Bostankaul alluvial fan and Roghani ridge. The stream (narrow whitish feature cutting in center across the ridge) that contributed to the alluvial fan surface is represented by east-west directed paleo-channel also cutting across the ridge although at a higher altitude (dark greyish linear feature south of the main stream). (B) Alluvial fan surfaces Qf1 to Qf3 and bedrock superimposed on a GeoEye-1 image with the locations of dated samples. The ridge is dissected by four water gaps (white numbers 1 to 4) and two wind gaps (black numbers 1 to 2) corresponding to the northern and central water gaps. The positions of these wind and water gaps record left-lateral movement along the Chaman fault at different time scales. The black rectangle shows the position of Figure 4.10. The white lines A and B are the transect lines for the profiles shown in Figures 4.8 and 4.10, respectively.

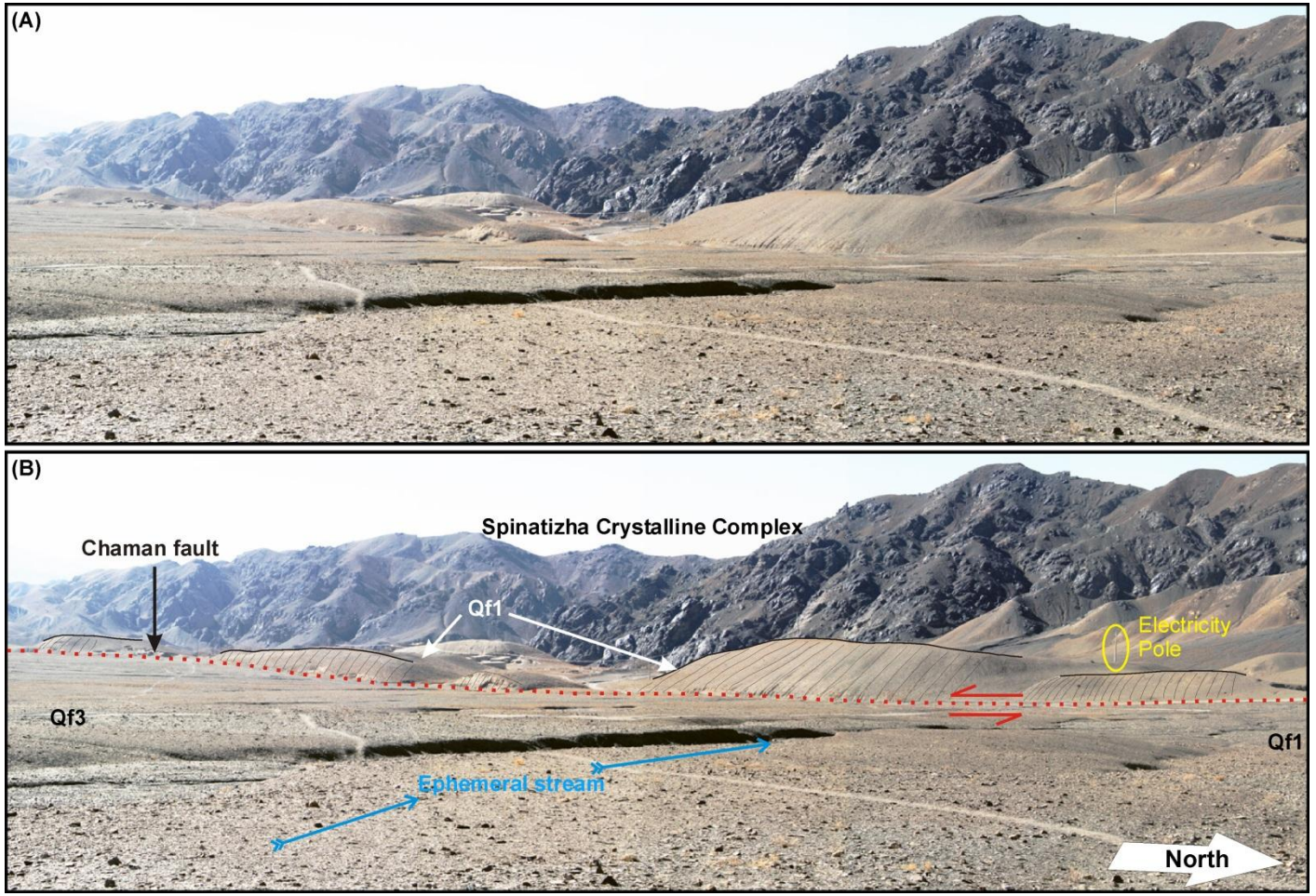

Figure 4.3: Field photographs of the Bostankaul fan and Roghani ridge. (A) Looking southwest field view of the southward displaced part of the BF making an east facing fault scarp with a maximum vertical height of ~ 40 m where sample # BK-1 was collected from a sandstone boulder of about 1.5 x 0.5 m size. Notice the smooth comparatively less incised surface of the Qf-3. An ephemeral stream to the north of the Qf-3 surface separates it from the Qf-1 surface.

has an average gradient of ~ 8 mm/m from east to west and records stream avulsion and incision as deep as ~40 m (Figure 4.8). On the southern periphery of the village there is a sharp slope discontinuity of about 30 – 35 m (see Figures 4.4 and 4.7), while northern limit of the fan body is not clearly defined because of the two coalescing fans forming a bajada (Figure 4.2). The discontinuity in slope at the southern extreme of the alluvial fan surface marks the southern boundary of the Bostankaul fan and I used this discontinuity as one of the piercing point (Figures 4.4 and 4.5). The sediment of the Bostankaul alluvial fan (Qf1) is marked by soil development and lithification to a level, which is lacking in sediment piles (Qf3) present south of the Bostankaul alluvial fan (Qf1) (Figure 4.9). The soil development on Qf1 is about 1 m thick and most of the human settlements (villages and fields) are inhabited on these surfaces where water is available (Figure 4.2, 4.6 and 4.7). Fanglomerates are infrequently present in Qf1 sediment mostly along the stream banks or in thrust blocks west of the Chaman fault. Qf3 surfaces are more uniform and unconsolidated having little stream incision mostly continuous having not been structurally disturbed (Figure 4.3 and 4.9 A).

The southward displaced part of the Bostankaul alluvial fan is an isolated body comprising of sediment correlating to the main alluvial fan sediment with a soil horizon at the top, comparatively lithified and deep erosion (Figure 4.3). There are about three small mounts aligned along a straight north-south line marking an east-facing fault scarp (Figures 4.10 and 4.11). The southernmost sediment pile is the last preserved patch of the Bostankaul alluvial fan and is used as the second piercing point to measure the total displacement (Figure 4.10 B). These small patches of alluvial fan sediments were once a

continuous body displaced as a single block but now incised by two ephemeral streams flowing from east to west (Figure 4.11). The average stream width of about 35 – 40 m adds to the total uncertainty in measuring displacement recorded by this displaced part of the alluvial fan body.

4.3.2.2. Roghani Ridge

This 8 x 1.5 km lenticular shaped ridge (Figure 4.2) is the northern extremity of the transpression comprising rocks of the Spinatizha Crystalline Complex. This is an isolated ridge that has recorded simultaneous progressive uplift associated with the northward propagation of the Spinatizha thrust and left-lateral displacement along the Chaman fault. The continued movement along the Chaman fault system has resulted in the formation of four prominent transverse water gaps and two corresponding wind gaps that dissect the ridge (Figures 4.2 and 4.5). The development of wind and water gaps, although a complex phenomenon, but is common along growing structures, especially along the thrust bounded folds (Burbank et al., 1996; Keller and DeVecchio, 2012). Further, it is essential to have at least two sets of wind and water gaps in a growing fault bound fold to estimate any lateral growth and direction of an active fault system (Azor et al., 2002). In case of Roghani ridge two prominent water gaps with their corresponding wind gaps were observed that are arranged in a way that supports northward growth of the Spinatizha thrust and left-lateral movement along the Chaman fault (Figure 4.4, 4.5 and 4.12). The abandoned stream which I assume as the past course of the present ephemeral stream (central water gap at ~ 1800 m elevation) that cut across the center of the Roghani

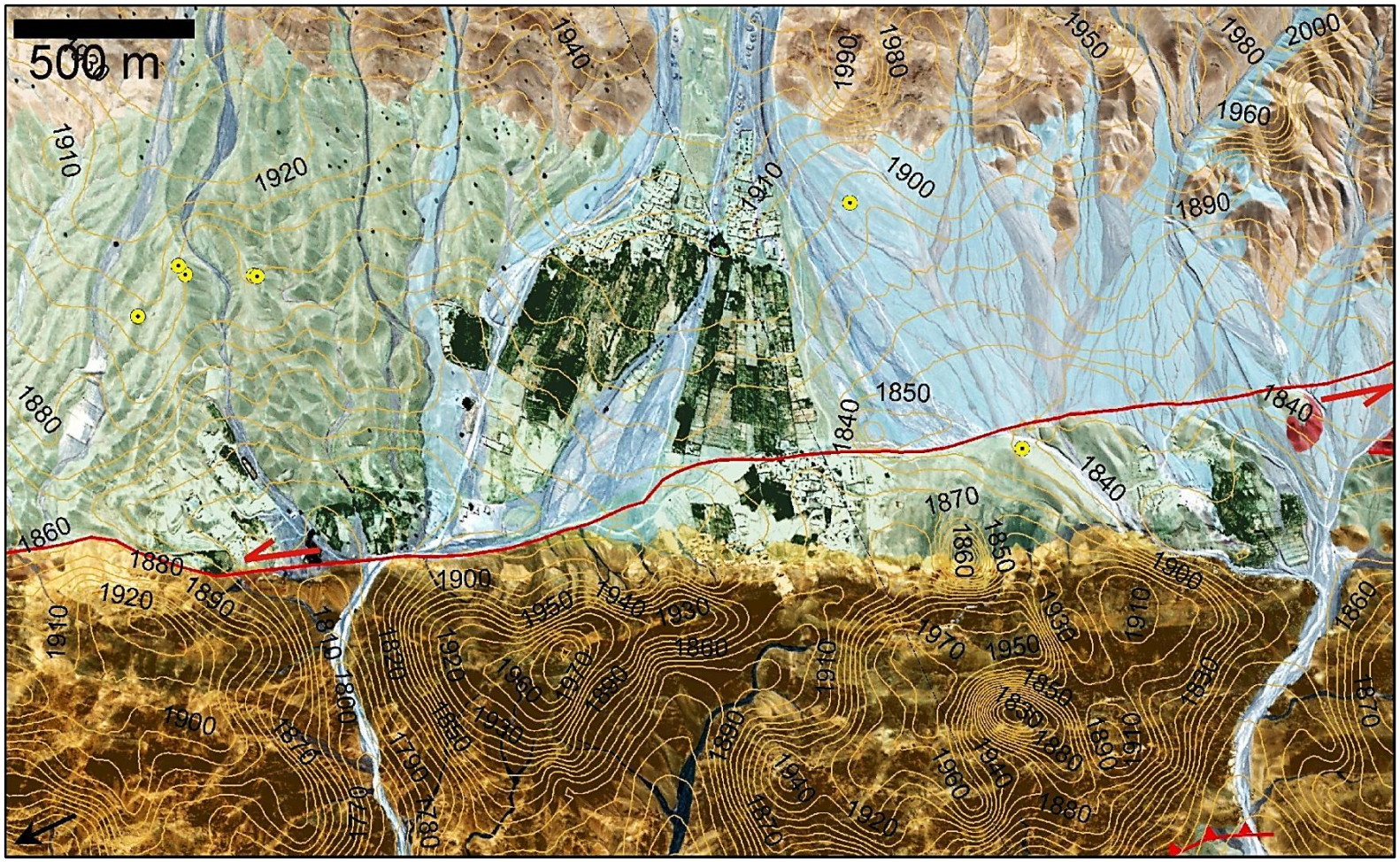

Figure 4.4: Bostankaul fan (green color) and Qf3 displayed with the contour lines extracted from 15 m absolute ASTER DEM with a 10 m contour interval. The Bostankaul village occupies the low-lying southern fringe of the fan body with an elevation difference from the Qf1. The southward displaced portion of the Qf1 forms an east-facing fault scarp as evident from the closely spaced contour lines.

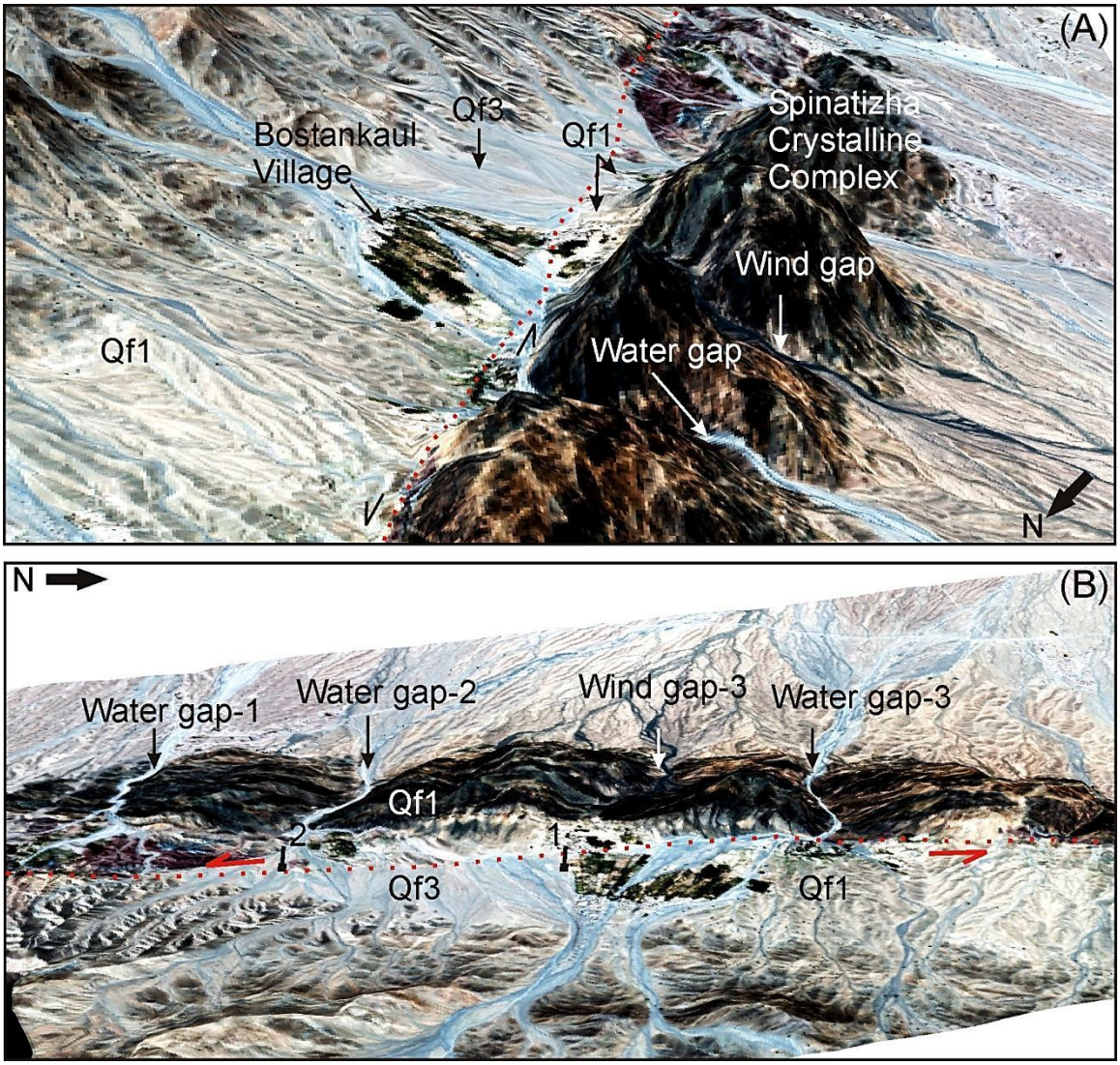

Figure 4.5: Perspective view extracted from GeoEye-1 data draped over ASTER DEM of the Roghani ridge and Bostankaul fan. In B the southward displaced part of the BF stands above the low lying Qf1. The older fan surface is deeply incised compared to the younger smooth surface. In C looking west the Roghani ridge is dissected by water gaps and a wind gap. The main Qf1 surface stands well above the active fan surface of Qf1. In center of the image is Qf1 to the west of the fault making an east-facing fault scarp.

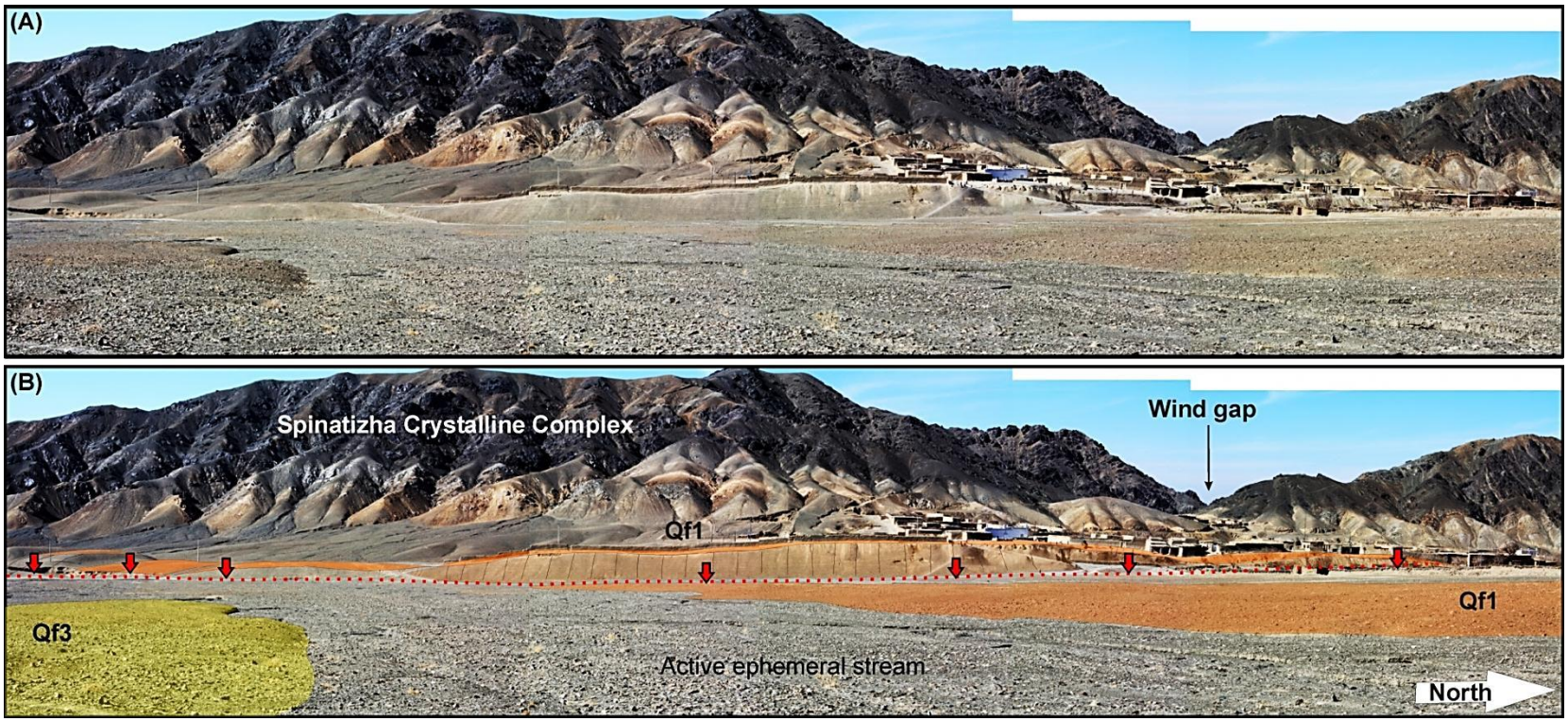

Figure 4.6: Field photographs of the Bostankaul fan and Roghani ridge. view of the ephemeral stream that separates the Qf-1 and Qf-3 and flowing orthogonal to the displaced part of the Qf-1 where it diverts towards south and follow a course longitudinal to the Spinatizha crystalline complex.

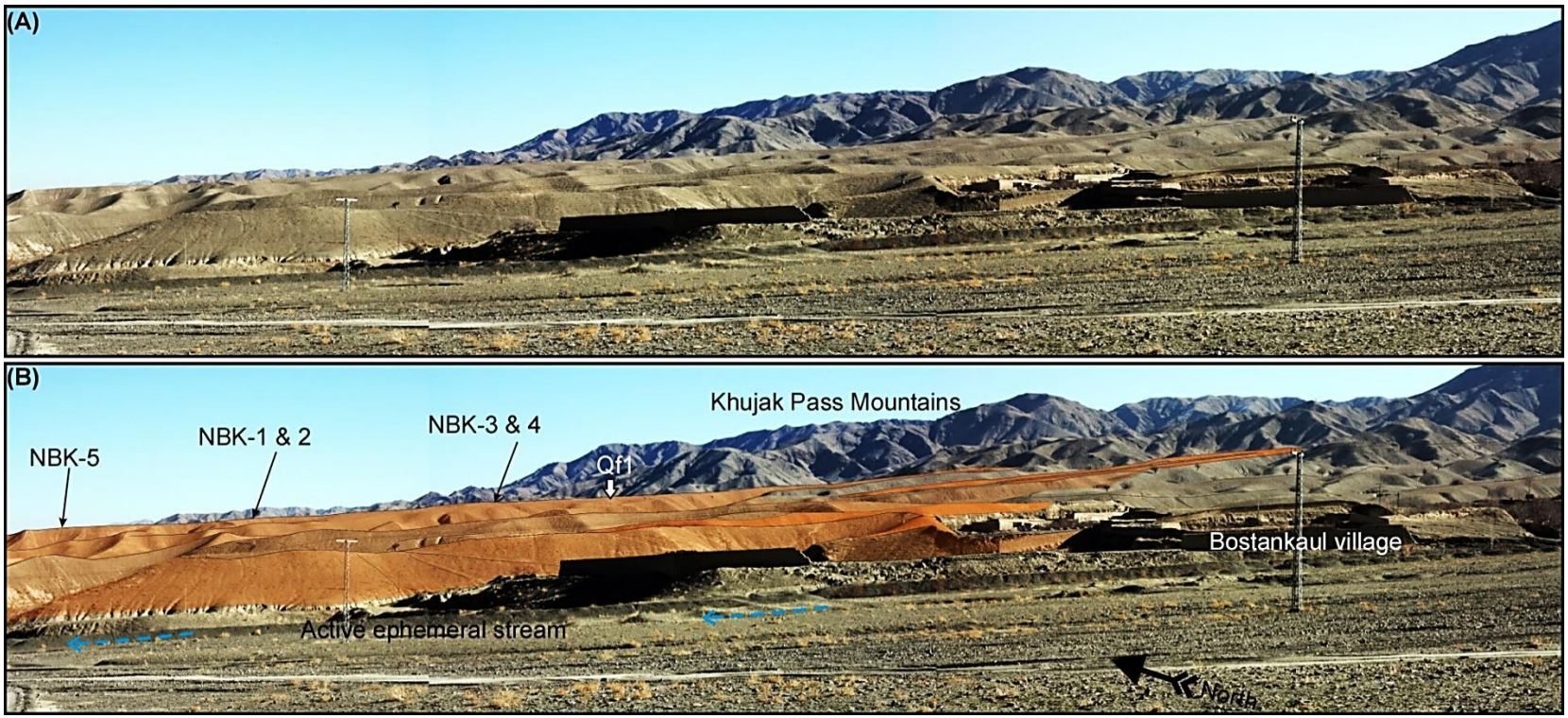

Figure 4.7: Main surface of the Bostankaul alluvial fan where most of the samples are collected. The overall surface is flat with a westward gradient of ~ 8mm/m. narrow streams with vertical and well-defined banks have incised the surface which is contrary to the Qf-3 surface (see A). The five samples that were collected from this surface are well spaced and settled in central parts of the flat surfaces with almost no burial or erosional signatures.

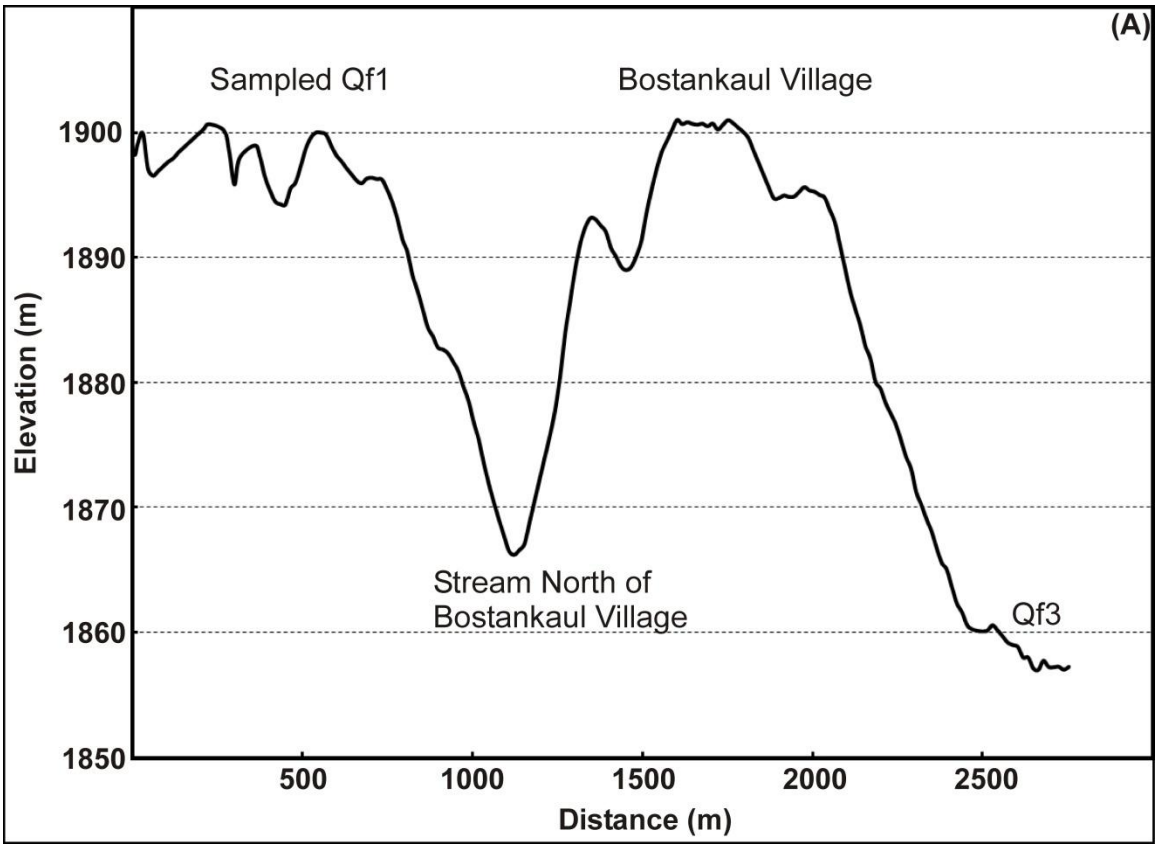

Figure 4.8: Surface expression of the Bostankaul alluvial fan (Qf1) and its association with Qf3 which lies almost ~ 40 m below the average Qf1 surface at ~ 1900 m altitude. Bostankaul village which lies on a part of the Qf1 surface is separated from the main fan body by a major stream dissecting the alluvial surface. Notice the narrow V-shaped stream in the center of the profile depicting fast incision and uplift.

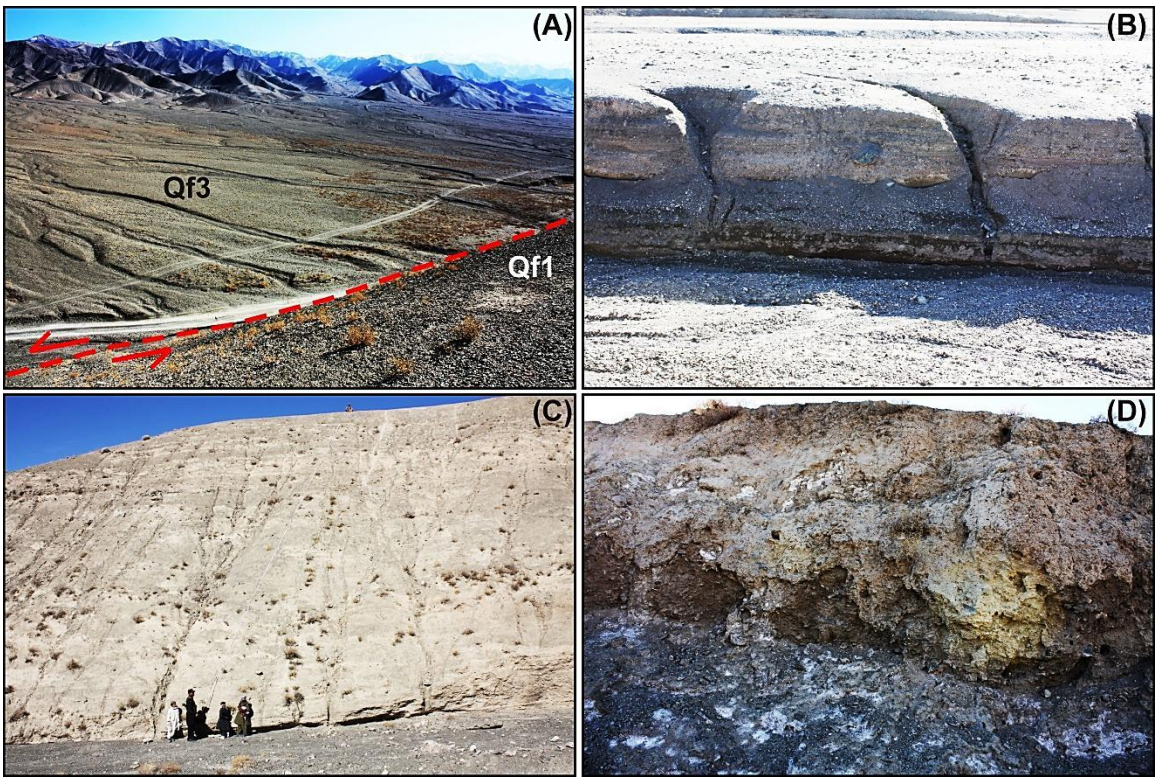

Figure 4.9: (A) Field view of a Qf3 surface with little or no incision. These generations of the alluvial surfaces are smooth and flat lying showing less deformation as compared to the Qf1 surfaces. (B) A close-up view of a vertical section in a Qf3 surface exposed in a stream. Qf3 sediment are unlithified and soil devoid upper sections. (C) An about 40 m vertical section within a Qf1 surface incised by a stream showing a well-lithified sequence. (D) Field view of an upper section of a Qf1 surface showing extreme leaching and soil formation. All Qf1 surfaces are marked by soil development supporting human settlements where water is present as in Bostankaul village which resides on a Qf1 surface.

N
30°45'N
A
A'
B
B'
C
C'
D
D'
E
E'
F
F'
350 m
(A)
Chaman Fault
Qf3
Qf1
Fault Gouge
Meta-volvanics of SCC
66°29'E
1150 ± 55 m
350 m
(B)

Figure 4.10: Left-lateral off-set along Chaman fault recorded by the southward displaced part of the Bostankaul alluvial fan. Lines AA' to FF' are the profile lines in Figure 4.11. (A) GoeEye-1 image of the displaced sediment incised by the ephemeral streams that are feeding to the Qf1 surface. (B) Geomorphological interpretation of the displaced landform as seen from the satellite images and measured in the field. This segment of the Chaman fault is sharply marked by an eastward facing almost vertical fault scarp. The two piercing lines which helped measure the actual displacement at this site are; 1) erosional contact between Qf1 and Qf3 east of the fault line and 2) southern limit of the Qf1 surface present west of the fault line and bounded by an ephemeral stream. The Qf1 surface west of the fault line is displaced towards south from the main fan body. This once continuous Qf1 surface is now dissected by the streams flowing orthogonal to the fault scarp. The streams width of 35-40 m adds significant error to the otherwise GeoEye-1 based measured displacement of 1150 m with a maximum ±3 m horizontal accuracy.

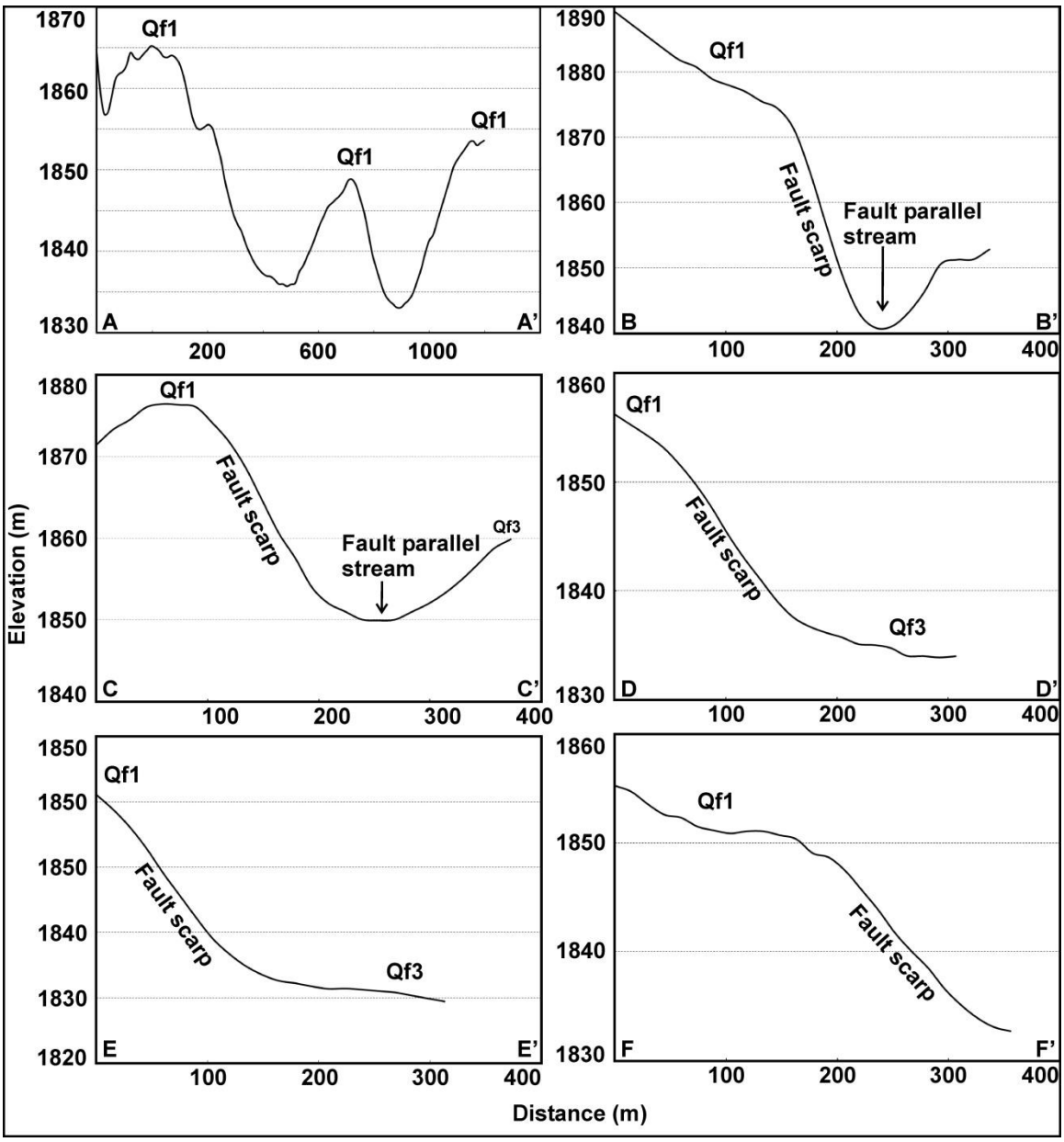

Figure 4.11: Surface expression and geometry of the fault scarp along the southward displaced part of the Bostankaul alluvial fan west of the Chaman fault. For location of the profile lines see Figure 4.10. (A) Longitudinal surface profile of the Qf1 body west of the fault which comprises of three small yet prominent mounts separated by two ephemeral streams is a continuous pile of sediment until its southern limit and has been displaced as an intact block. This Qf1 body makes a sharp east-facing fault scarp which rises ~ 15 m in the south to more than 30 m in the north above the Qf3 surface. (AA' – FF') Surface profiles orthogonal to the fault trace showing the east-facing fault scarp. The almost vertical fault scarp is a continuous plane of more than 1000 m length from the Bostankaul village in the north to the southern limit of the Qf1.

ridge may have fed to the Bostankaul alluvial fan is 77 ± 15 m above the water gap. Laterally the two gaps are 1348 ± 15 m apart with the water gap to the north of the wind gap implying a left-lateral displacement and northward propagation of the ridge (Figure 4.4, and 4.5). The other set of wind and water gaps at the northern end of the ridge also reinforce same sense of motion but with smaller lateral displacement (~ 450 m) and vertical uplift (~ 56 m) recording a younger activity along the Chaman fault system. The water gaps in the southern end of the ridge pose a complex evolution history with no preserved wind gap and will complicate further restoration of the displacement recorded by Bostankaul alluvial fan.

4.3.2.3. Observed displacement

The southward-displaced part of the Bostankaul alluvial fan was restored to its original position using field and satellite image measurements of Qf1 and Qf3 surfaces. The Qf1 shows a total displacement of 1150 ± 55 m (Figure 4.10). This is further supported by the topography of the Roghani ridge with the present positions of the adjacent water and wind gaps in center of the ridge.

4.3.3. ^{10}Be TCN dating

Eight samples were collected for ^{10}Be TCN dating from the three different alluvial fan surfaces, including six from the alluvial fan surface (Qf1) that has recorded the total displacement of 1150 ± 55 m (Table 4.2; Figure 4.2). The samples were collected from well-embedded sandstone boulders, typically meter-sized, that has well developed rock varnish and were sourced from the Khojak Pass Mountains (Figure 4.13). Boulders rich

in quartz with little evidence of weathering were preferentially sampled. About 700-1000 g of sample was collected from the top 1-3 cm of each desired boulder using a hammer and chisel. The samples were crushed in the geochronology laboratories at and the University of Cincinnati and quartz was separated from the 250–500 µm particle size fraction using the acid dissolution and heavy liquid separation as described in Owen et al. (2006; 2011). A ^{9}Be carrier was added to the purified quartz and Be (^{10}Be/^{9}Be) was separated using ion exchange chromatography. $Be(OH)_2$ was precipitated at pH > 7 and oxidized in quartz crucibles at a temperature of 700°C. BeO was then mixed with Nb metal prior to determination of the ^{10}Be/^{9}Be ratio by accelerator mass spectrometry at the Purdue Rare Isotope Measurement (PRIME) Laboratory at Purdue University. SPEX beryllium standard (trace ICP/ICP-MS grade) at 1000 mg mL^{-1} in 2% HNO3 was used for all samples and blanks. Two chemical blanks were processed and had a weighted mean ^{10}Be/^{9}Be ratio of 7.68 ± 2.24 x 10^{-15}. The Purdue Rare Isotope Measurement (PRIME) Laboratory accelerator mass spectrometer was calibrated using standard 200500020 from KN Standard Be 0152 with a ^{10}Be/^{9}Be ratio of 9465x10^{-15}. All ^{10}Be/^{9}Be ratios were converted to the revised ICN of Nishiizumi et al. (2007), which is assumed to be the most correct standard and requires a production rate of 4.5± 0.3 ^{10}Be atoms/yr and a half-life of 1.36 Myr for age calculation (PRIME Laboratory, 2007). ^{10}Be concentrations in quartz were calculated from ^{10}Be/^{9}Be measured ratios using the total Be in the samples and the sample weights. Production rates were scaled to the latitude and elevation of the Chaman sampling sites using the star scaling factors of Stone (2000), and an assumed 2.2% sea-level-high-latitude (SLHL) production muon contribution using the CRONUS-Earth online calculator, version 2.2 (Balco et al., 2008;

http://hess.ess.washington.edu/). These scaling factors reproduce the star scaling factors of Lal (1991). ^{10}Be concentrations were then converted to zero-erosion exposure ages using a SLHL ^{10}Be production rate of 4.5 ± 0.3 atoms/g quartz/yr (cf. Nishiizumi et al., 1989; Kubik and Ivy-Ochs, 2004). The impacts of topographic and depth corrections were determined by numeric integration of the flux corrected for the dip and topography at all azimuth directions (Nishiizumi et al., 1989).

TCN ages were calculated by applying the Stone (2000) and Lal (1991) time-independent model using the CRONUS-Earth online calculator, version 2.2 (Balco et al., 2008; http://hess.ess.washington.edu/). I use the time-independent model because of the continued debate regarding appropriate corrections and models for temporal variation in Earth's magnetic field. However, I recognize that different models may give up to 9 - 11% difference in ages. Slip-rate studies generally use 4-10 ^{10}Be dates per surface to identify clustering and to avoid the problems of sample displacement/erosion resulting in too young and inheritance resulting in too old ages (Chevalier et al., 2005; Frankel et al., 2007a,b; Blisniuk et al., 2010).

4.3.3.1. ^{10}Be model ages

The ^{10}Be model ages, excluding the one outlier (Sample # NBK-3) define a consistent depositional age cluster that was used to date their abandonment (Figure 4.14). ^{10}Be dates on the displaced Bostankaul alluvial fan range between 32 and 39 kyr (weighted mean age 34.8 ± 3.0 kyr (2σ error) excluding the outlier). The ^{10}Be date of 13.1 ± 1.7 kyr for

sample NBK-3 is likely the result of enhanced weathering and/or toppling of the sampled boulder. The ^{10}Be date for a sample on southward-displaced part of the Bostankaul alluvial fan is 38.6 ± 3.7 kyr (BK-1), which falls within the ^{10}Be age cluster for the main alluvial fan (Figure 4.14).

The young date of 6.5 ± 1.1 kyr for sample BK-3, a boulder on an alluvial fan surface south of the displaced Bostankaul alluvial fan, can be explained by being deposited within a much younger deposit that formed after the abandonment of the Bostankaul alluvial fan—hence marking the southern fringe of the alluvial fan. Alternatively, it by itself is the southern extreme of the Bostankaul alluvial fan that has been uplifted and eroded away since its abandonment, resulting in a younger depositional age. The first possibility places an upper limit on the displacement to be 1150 ± 55 m, which is in agreement with the displacement recorded by the positions of the water and wind gaps. In contrast, restoration of the fan based on the eroded portion of the alluvial fan, from its presumed apex, yields a total displacement of about 880 ± 55 m for the Bostankaul alluvial fan surface.

The only dated sample west of the Roghani Ridge dates to 20.1 ± 2.2 kyr, which I group to the ages of Bostankaul fan because of the sedimentological similarity in the two alluvial surface. The difference in the ages may reflect a more eroded alluvial surface west of the ridge in contrast to the alluvial surface present east of the Roghani ridge. Therefore the alluvial surface that I dated west of the ridge can be argued to be of the

same generation of alluvial fan as the Bostankaul fan. This implies that the Bostankaul alluvial fan and alluvial fans west of the Roghani ridge pre-date the uplift of the ridge, which rises 77 ± 15 m above alluvial fan surface (Figure 4.14), along the Spinatizha thrust fault.

4.3.4. Slip rates

Matching the 1150 ± 55 m offset with the surface abandonment sample ages for the Bostankaul alluvial fan yields a geomorphic left-lateral slip rate ranging from 30.1 ± 2.9 to 36.2 ± 3.1 mm/yr, with an average of 33.1 ± 3.2. These geomorphic rates are consistent with the geologically (10^6 years) estimated slip rate of 19–35 mm/yr (Beun et al., 1979; Lawrence et al., 1992), although they are at the high range. In contrast, the geomorphic rates are more than two to four times that of the geodetically estimated rate of 18 ± 1 mm/yr (Mohadjer et al., 2010) and the post-seismic slip rate of ~ 8 mm/yr that was estimated from InSAR analysis (Furuya and Satyabala, 2008).

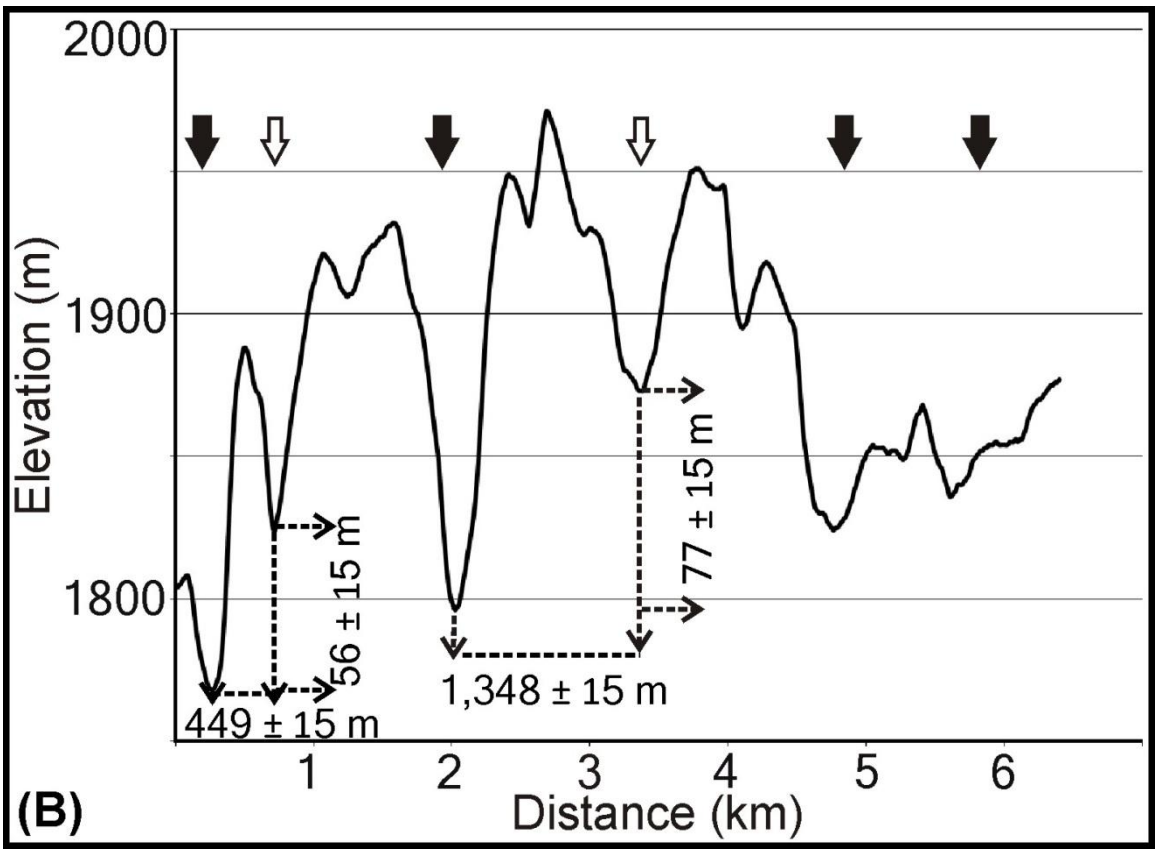

Figure 4.12: Longitudinal profile across the Roghani Ridge. Note the gradual decrease in wind gaps (hollow arrows) and water gaps' (filled arrows) elevation towards north. The wind gap associated with the central water gap is been translated toward south 1348 ± 15 m, which reconciles with the surface dislocation of about 1150 ± 55 m of the Bostankaul alluvial fan by a strand of the Chaman fault. The elevation difference of 77 ± 15 m between the two gaps accounts for the vertical uplift of the ridge.

Figure 4.13: Views of typical samples used in dating the BF surface. (A) Sample # NBK-1 location on a flat part of the BF. This meter-sized boulder is well set on the surface showing no toppling or burial. All the samples collected from BF surface are well exposed having no apparent shielding of the cosmic rays. (B) A close-up view of the boulder in A completely desert varnished and having no weathering effects of peeling off. All the boulders used in dating were similar to NBK-1. (C) Close-up view of the NBK-5 showing desert varnishing, cross-cutting calcite veins filling and no physical weathering effects.

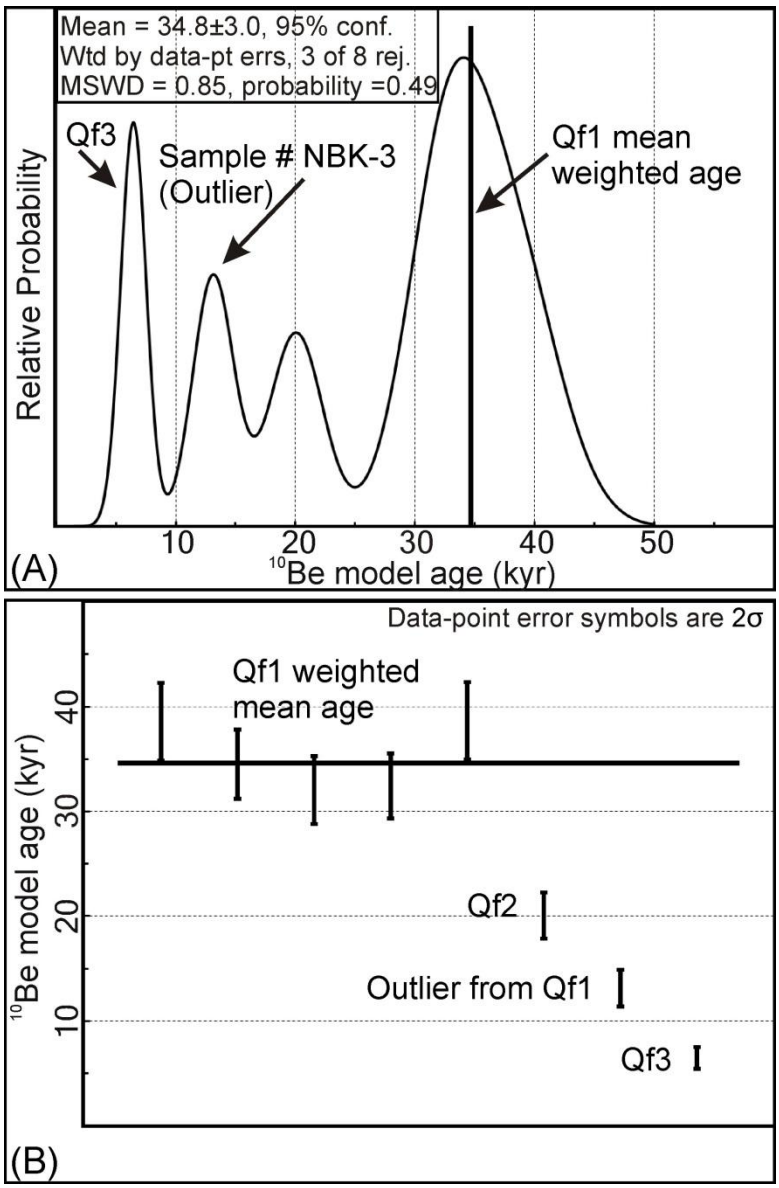

Figure 4.14: (A) Probability density function (PDF) and (B) weighted mean of the ^{10}Be model ages of the Bostankaul alluvial fan. All the ages used in calculating the slip rate cluster around weighted mean alluvial fan age of 34.8 ± 3.0 kyr excluding the outlier (Sample # NBK-3).

Table 4.2: Sample locations, descriptions, and summarized ^{10}Be TCN data and ages for three alluvial fan surfaces including the displaced Bostankaul alluvial fan.

Sample number	Surface	Lithology	Location		Altitude	Size a/b/c axes	Thick-ness	Production rate (atoms/g/yr)		Shiel-ding factor	Quartz#	Be carrier	^{10}Be/^{9}Be §,**	^{10}Be concentra-tion ††,##	Age §§,***	Age§§,†††
			latitude	longitude												
			°N	°E	(m asl)	(cm)	(cm)	Spallat-ion*	Muons†		g	(mg)	x 10^{-13}	10^4 atoms/ g SiO_2	kyr	kyr
NBK-1	Qf1	Sandstone	30.763	66.488	1926	90/50/40	1.5	14.86	0.335	1.0	21.585	0.3626	4.21±0.17	64.12±2.62	38.53±1.59	38.53±3.74
NBK-2	Qf1	Sandstone	30.763	66.488	1923	90/60/40	2	14.77	0.334	1.0	27.2966	0.3547	4.85±0.18	57.14±2.15	34.48±1.31	34.48±3.29
NBK-3	Qf1	Sandstone	30.761	66.488	1921	170/140/60	1	14.87	0.336	1.0	26.3834	0.3620	1.77±0.17	22.04±2.14	13.13±1.28	13.13±1.72
NBK-4	Qf1	Sandstone	30.761	66.488	1921	120/110/100	2.5	14.69	0.334	1.0	16.6977	0.3549	2.74±0.14	52.82±2.74	32.04±1.68	32.04±3.27
NBK-5	Qf1	Sandstone	30.765	66.488	1909	230/90/60	2.5	14.58	0.332	1.0	25.8119	0.3539	4.26±0.16	52.96±2.02	32.41±1.25	32.41±3.10
BK-1	Qf1	Sandstone	30.745	66.475	1884	130/50/40	2	14.39	0.330	1.0	14.9789	0.3462	2.97±0.11	62.26±2.35	38.64±1.47	38.64±3.69
BK-3	Qf3	Sandstone	30.747	66.482	1928	110/40/50	2	14.81	0.335	1.0	13.8512	0.3629	0.45±0.06	10.76±1.51	6.46±0.91	6.46±1.07
RG-2	Qf2	Sandstone	30.733	66.456	1826	130/90/80	1.5	13.91	0.325	1.0	11.5341	0.3451	1.16±0.08	31.42±2.13	20.05±1.37	20.05±2.22

*Constant (time-invariant) local production rate based on Lal (1991) and Stone (2000). A sea level, high-latitude value of 4.5 ± 0.3 at ^{10}Be g^{-1} quartz was used.
†Constant (time-invariant) local production rate based on (Heisinger et al., 2002).
A density of 2.6 g cm^{-3} was used for all surface samples.
§ Isotope ratios were normalized to ^{10}Be standards prepared by Nishiizumi et al. (2007) with a value of 2.85 x 10^{-12} and using a ^{10}Be half-life of 1.36 x 10^6 years.
**Uncertainties are reported at the 1σ confidence level.
†† Samples were corrected for a mean blank ^{10}Be/^{9}Be = ~7.68 ± 2.24 x 10^{-15}.
Propagated uncertainties include error in the blank, carrier mass (1%), and counting statistics.
§§ Beryllium-10 model ages were calculated with the CRONUS-Earth online calculator, version 2.2 (Balco et al., 2008; http://hess.ess.washington.edu/).
*** Analytical uncertainty is quoted.
††† Uncertainty quoted by propagated error in the model ages includes a 6% uncertainty in the production rate of ^{10}Be and a 4% uncertainty in the ^{10}Be decay constant.

4.4. Discussion

Multiple slip rates are important to understand the nature of fault systems (Frankel et al., 2011; Frankel and Owen, 2012). However, discrepancies between slip rates determined for different time intervals has led to contrasting interpretations including secular variations in slip rate along faults (e.g. Chevalier et al., 2005; Frankel and Owen, 2012), strain trade-off among interacting faults and fault inversion (e.g. Oskin et al., 2007; Blisniuk et al., 2010; Hoeft and Frankel, 2010). Some studies have tried to reconcile the geodetic and geomorphic slip rates (Cowgill et al., 2009).

The displacement measured during this study along the Chaman fault represents many earthquake cycles spanning over the last ~ 35 kyr. These earthquakes may account for the overall average displacement and thus restricting the impact of inter- and/or post-seismic relaxations, which has a major impact on the GPS and InSAR constrained slip rates (e.g. Meade, 2007). Seismic activity including instrumental data from 1974 until 2010 and the two historic earthquakes of 1892 Chaman earthquake (Mw ~ 6.7) and 1935 Quetta earthquake (Mw ~ 7.7) (Figure 4.15), and as summarized by Ambraseys and Bilham (2003), shows fewer events as compared to the total convergence accommodated by the boundary zone (Molnar and Dayem, 2010). Most of the activity is within the central part of the Chaman fault system where a slip rate of 49.1 mm/yr within a zone of 60 km including the Chaman fault is estimated contrary to the 3.1 mm/yr and 0.5 mm/yr slip rate in north and south of the most seismically active central part of the fault where I measured the slip rate (Figure 4.15). Ambraseys and Bilham (2003) predicted a slip

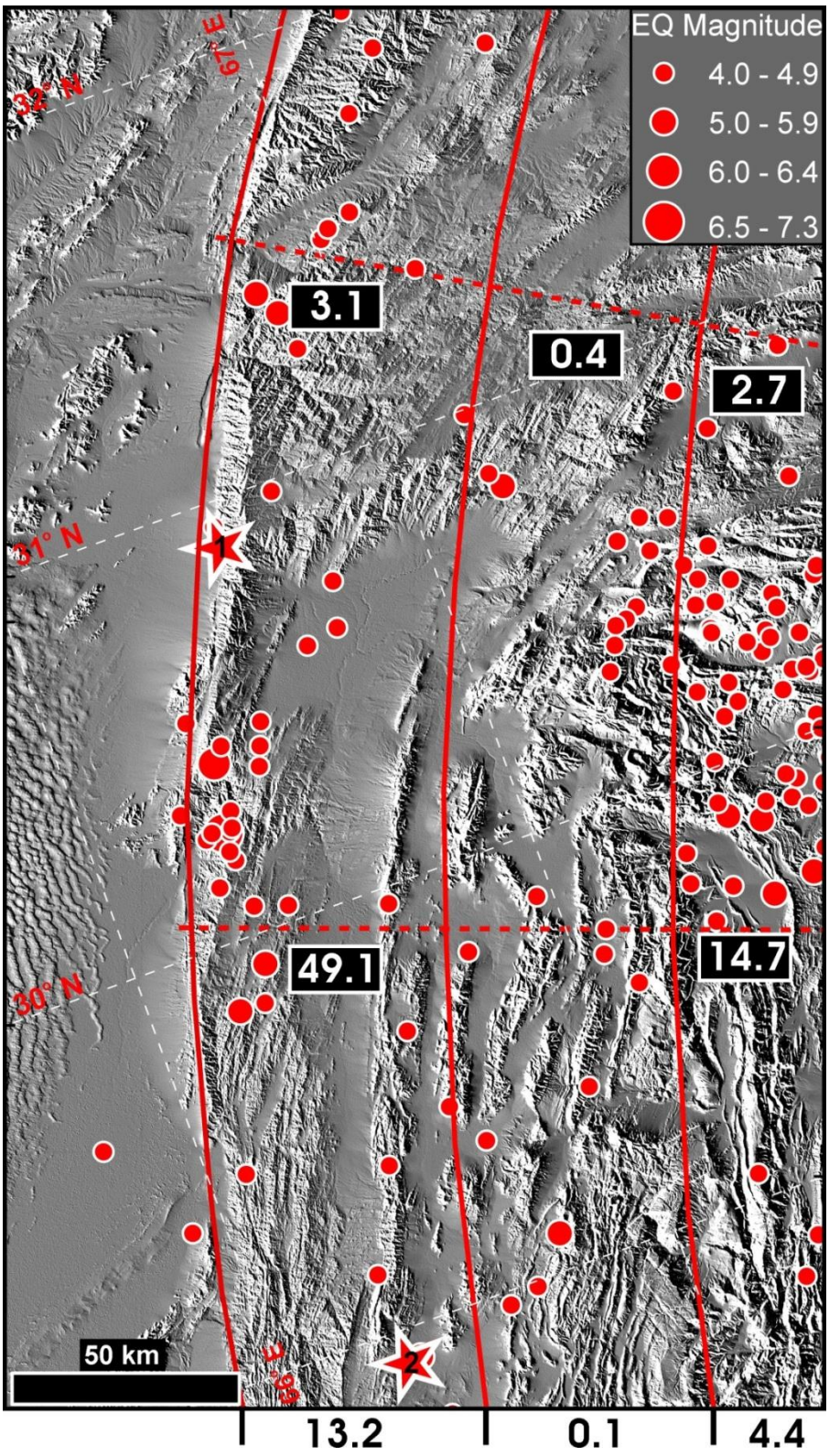
EQ Magnitude
4.0 - 4.9
5.0 - 5.9
6.0 - 6.4
6.5 - 7.3
3.1
0.4
2.7
49.1
14.7
1
2
32° N
31° N
30° N
67° E
68° E
50 km
13.2
0.1
4.4

Figure 4.15: Seismicity within a part of the western Indian plate boundary zone including instrumental earthquake data from 1974 – 2010 with events larger than Mw 4.0 (from USGS earthquake catalog) and the historical Mw ~ 6.7 Chaman earthquake of 1892 (star 1) and Mw ~ 7.7 Quetta earthquake of 1935 (star 2) (Ambraseys and Bilham, 2009). Seismic activity is concentrated east of the Chaman fault with almost no seismicity in the west of the fault. The three 60 km wide zones (red north-south lines) were estimated by Ambraseys and Bilham (2003) based on about 200 years earthquake data showing an average slip rate of 49.1 mm/yr in the western zone with a cumulative moment release equivalent to ~ 13.2 mm/yr slip rate. This zone includes the Chaman fault which limits the boundary zone in the west. Numbers in black rectangles in each 60 km swath is the equivalent slip rate of the moment release, while black numbers at the bottom of the figure resemble slip rate equivalent to the reduction in moment release.

deficit enough to trigger one or more events of Mw> 7 in this 60 km wide western plate boundary zone, and concluded that the seismic activity of the past century in the region is not representative of the long-term slip rate within the plate boundary zone. This further implies that the fault segment which is the center of most of the studies (the northern part of the Chaman fault that runs in Pakistan) is in the late stage of its seismic cycle and will be moving slow as compared to the cumulative geomorphic slip rate as has been noticed along the San Andreas fault system in Southern California (Chuang and Johnson, 2011). However, the earthquake cycle of the Chaman fault system is poorly defined across many time intervals and, of course, a more comprehensive dataset needs to be obtained from future studies. Moreover, plate boundary velocities estimated from InSAR data spanning a year and a half time period shows episodic slip along a creeping Chaman fault associated with a M_w5.0 earthquake (Furuya and Satyabala, 2008), implying larger displacements with surface ruptures associated with high magnitude events like the 1892 Chaman earthquake which are prevalent in this region (Lawrence et al., 1992). InSAR investigations on longer time scales may be able to resolve the strain distribution within the plate boundary zone.

Fault inversion within the shear zone may account for the presently slower displacements (18 ± 1 mm/yr) along the Chaman fault, which is a common phenomenon of strain distribution within the plate boundary zone (Bennet et al., 2004). The Ghazaband, Gardez and Ornach-Nal faults (Figure 4.1), which mark the eastern limit of the shear zone (Lawrence et al., 1992), might be the candidates for strain tradeoff between the Chaman fault and these other faults. However, it is very unlikely that such a process can occur on

a shorter timescale (< 10^6 yr) and as such these complimentary faults within the shear zone are responsible for sparse tectonic activity in Quaternary (Lawrence et al., 1992). Another possibility causing the disparity might be the convergence of the fold thrust belts along this transpressive plate boundary resulting in strain partitioning rates ranging from 3–6 mm/yr (Szeliga et al., 2009; Bernard et al., 2000) to 13 ± 3 mm/yr (Ambraseys and Bilham, 2003) (Figure 4.15). Strain partitioning is essential to the geometry of the azimuth of the Indian Plate motion relative to Eurasia (N12°E) and strike of the Chaman fault (N34°E) (Molnar and Dayem, 2010), which implies strain distribution within the northwestern rigid Indian Plate boundary although most of the strain is accommodated along the Chaman fault.

4.5. Conclusions

The 33.3 ± 3.0 mm/yr is the first geomorphic slip rate based on actual displacement along a strand of the Chaman fault. Strains partitioning within the plate boundary zone may be the main factor causing the disparity in geodetic and geomorphic slip rates along the Chaman fault; however, transient strain accumulation within in the plate boundary zone is the possible explanation of a faster moving Chaman fault which is late in its seismic cycle. Current geodetic and geomorphic datasets conclude that strike-slip faults in the Chaman transform zone along the Indian plate boundary have a complex history and evolution.

Chapter 5 : Summary

Kinematics of the Indo-Asian western collision boundary zone is studied from two broader aspects. 1) Evolution of the arc system in response to the Indian plate subduction beneath the Asian plate along its western boundary; and 2) Late Quaternary activity within the collision boundary zone by estimating morphochronologically constrained slip rate along the Chaman fault. This research relied mainly on processing of satellite images including multispectral ASTER and GeoEye-1, geochemistry/geochornolgy of igneous rocks, and cosmogenic ray exposure dating of the deformed landforms.

Rock from the fragments of the Chagai-Ras Koh arc system and Khwaja Amran-Spinatizha Crystalline Complex show subduction related geochemical signatures. Arc volcanic rocks in both areas are intruded by granitic rocks. U-Pb dating of the zircons from the Khwaja-Amran-Spinatizha area suggests that magmatisim in this part of the arc system continued until ~ 58 Ma. The ~ 35 Ma and ~ 20 Ma ages from the granitic rocks in Chagai-Ras Koh arc area may be related to; 1) completion of southernmost collision between Indian and Asian plates by ~ 35 Ma (Carter et al., 2010; Treloar and Izatt, 1993), and 2) initiation of strike-slip movement along the western collision boundary after the deposition of the Katawaz basin sediments by ~ 20 Ma (Lawrence et al., 1992).

The Late Quaternary activity along the Chaman fault is well explained by the geomorphology around a transpression along the fault. The actively evolving landscape of Roghani ridge and Bostankaul alluvial fan represents simultaneous interaction of the

Chaman strike-slip and Spinatizha thrust faults and the Chaman basin. The alluvial fan surfaces and bajadas are deeply incised by narrow v-shaped valleys and are left-laterally displaced. Topographic and geomorphic characteristics of the Roghani ridge indicate a northward lateral growth of the Spinatizha thrust fault as one of the several transpressions along the Chaman fault that accommodate convergence required for the difference in azimuths of the strike of the Chaman fault and the relative motion of Indian and Eurasian plates. The abandoned surface of the Bostankaul alluvial fan records ~ 1150 m left-lateral displacement along a strand of the Chaman fault. Six quartz-rich meter-sized sandstone boulders from this flat alluvial surface were processed to separate ^{10}Be cosmogenic nuclides generated since the abandonment of this surface. The AMS measured ^{10}Be atoms yields a weighted mean age of ~ 35 kyr for this surface. This exposure age when matched with the displacement recorded by the alluvial surface gives a slip rate of ~ 33 mm/yr along the Chaman fault in this site. This rate agrees with the geologically constrained slip rate of ~ 19–35 mm/yr (Buen, et al., 1979; Lawrence et al., 1992) but is almost twice that of the GPS modeled slip rate (Mohadjer et al., 2010). There are two possible explanations for this discrepancy; 1) slip partitioning, and/or 2) transient strain accumulation within the boundary zone. Slip portioning could be possible reason of the present slower Chaman fault as the fold-thrust belt of the Kirthar-Sulaiman range and other smaller faults within the transform shear zone may account for accommodating the Indian plate convergence. However, lack of major seismic events except the 1892 Chaman earthquake with surface rupture that accounted for ~ 80 cm displacement along the fault explains the current slow nature of the fault as modeled by a decade long GPS

data. The geomorphic slip rate from this study averages events like the 1892 over the last 35 kyr; hence averaging both the faster slower episodes of activity along the fault for the said time period. Thus a slower current Chaman fault which is late in its seismic cycle explains the phenomenon of transient strain accumulation within the plate boundary zone.

Bibliography

Abrams, M., Hook, S., and Ramachandran, B., 2004. ASTER User Handbook, Version 2. Jet Propulsion Laboratory, California Institute of Technology. Online: http:// asterweb.jpl.nasa.gov/content/03_data/04_Documents/aster_user_guide_v2.pdf

Altamimi, Z., Collilieux, X., Legard, J., Garayt, B., and Boucher, C., 2007. ITRF2005: A new release of the International Terrestrial Reference Frame based on time series of station positions and Earth Orientation Parameters. Journal of Geophysical Research 112: B09401, doi: 10.1029/2007JB00494.

Ambraseys N., and Bilham R., 2009. The tectonic setting of Bamiyan and the seismicity in and near Afghanistan for the past twelve centuries. In: Margottini, C., (ed.), The Destruction of the Giant Buddha Statues in Bamiyan, Central Afghanistan. UNESCO Special Publication: UNESCO's emergency activities for the recovering and rehabilitation of cliff and niches, 158 pp. (Chapter 5, 67–94).

Ambraseys, N., and Bilham, R., 2003. Earthquakes and associated deformation in northern Baluchistan. Bulletin Seismological Society of America 93: 1573–1605.

Arthurton, R.S., Alam, G.S., Ahmad, S.A., and Iqbal, S., 1979. Geological history of the Alam Reg-Mashki Chah area, Chagai, Baluchistan. In: Farah, A., and Dejong, K.A. (Eds.), Geodynamics of Pakistan, Geological Survey of Pakistan, Quetta, Pakistan, 325–331.

Avouac, J-P., and Tapponnier, P., 1993. Kinematic model of active deformation in Asia. Geophysical Research Letters 20: 895– 898.

Azor, A., Keller, E.A., and Yeats, R.S., 2002. Geomorphic indicators of active fold growth: South Mountain–Oak Ridge anticline, Ventura basin, southern California. Geological Society of America Bulletin 114: 745–753.

Balco, G., Stone, J.O., Lifton, N.A., and Dunai, T.J., 2008. A complete and easily accessible means of calculating surface exposure ages or erosion rates from ^{10}Be and ^{26}Al measurements. Quaternary Geochronology 3: 174–195.

Bendick, R., Bilham, R., Freymueller, J., Larson, K., and Yin, G., 2000. Geodetic evidence for a low slip rate in the AltynTagh fault system. Nature 404: 69–72.

Bennett, R.A., Friedrich, A.M., and Furlong, K.P., 2004. Codependent histories of the San Andreas and San Jacinto fault zones from inversion of fault displacement rates. Geology 32: 961–964.

Bernal, A., Hardy, S., Gawthorpe, R., and Finch, E., 2004. Stratigraphic expression of the lateral propagation and growth of isolated fault-related uplifts. Basin Research 16: 219–233.

Bernard, M., Shen-Tu, B., Holt, W., and Davis, D., 2000. Kinematics of active deformation in the Sulaiman Lobe and Range, Pakistan. Journal of Geophysical Research 105: doi: 10.1029/1999JB900405.

Beun, N., Border, P., and Carbonnel, J., 1979. Premières données quantitative relatives' au coulissage du décrochement de Chaman (Afghanistan du sud-est). C. R. Acad. Sci. Paris, 288: 931–934.

Bilham, R., 2004. Earthquakes in India and the Himalaya: tectonics, geodesy and history. Annals of Geophysics 47: 839 – 858.

Blisniuk, K., Rockwell, T., Owen, L.A., Oskin, M., Lippincott, C., Caffee, M.W., and Dortch J., 2010. Late Quaternary slip rates gradient defined using high-resolution topography and ^{10}Be dating of offset landforms on the southern San Jacinto Fault zone, California. Journal of Geophysical Research 115: doi: 10.1029/2009JB006346.

Breitzman, L.L., Birnie, R.W., and Johnson, G.D., 1983. Fission-track ages of the Chagai Intrusives, Baluchistan, Pakistan. Geological Society of America Bulletin 94: 253 – 258.

Brown. E.T, Bendick, R., Bourlés, D., Gaur, V. Molnar, P., Raisbeck, G.M., and Yiou, F., 2002a. Slip rates of the Karakorum fault, Ladakh, India, determined using cosmic ray exposure dating of debris flows and moraines. Journal of Geophysical Research 107: B9, 2192, doi: 10.1029/2000JB000100

Bull, W., 1997. Discontinuous ephemeral streams. Geomorphology 19: 227–276.

Burbank, D., 2005. Cracking the Himalaya. Nature 434: 963 – 964.

Burbank, D., Meigs, A., and Brozovic, N., 1996. Interactions of growing folds and coeval depositional systems. Basin Research 8: 199–223.

Carter, A., Najman, Y., Bahroudi, A., Bown, P., Garzanti, E., and Lawrence, R.D., 2010. Locating earliest records of orogenesis in western Himalaya: Evidence from Paleogene sediments in the Iranian Makran region and Pakistan Katawaz basin. Geology 38: 807 – 810.

Castelltort, S., and Simpson, G., 2006. Growing mountain ranges and quenched river networks. C. R. Geoscience 338: 1184–1193.

Chen, Z., Burchfiel, B.C., Liu, Y., King, R.W., Royden, L.H., Tang, W., Wang, E., Zhao, J., and Zhang, X., 2000. Global positioning system measurements from eastern Tibet and their implications for India/Eurasia intercontinental deformation. Journal of Geophysical Research 105: 16215–16227.

Chevalier, M.L., Ryerson, F.J., Tapponnier, P., Finkel, R.C., Van der Woerd, J.V., Haibing, L., and Qing, L., 2005. Slip-rate measurements on the Karakorum Fault may imply secular variations in fault motion. Science 307: 411–414.

Chuang, R.Y., and Johnson, K.M., 2011. Reconciling geologic and geodetic model fault slip-rate discrepancies in Southern California: Consideration of non-steady mantle flow and lower crustal fault creep. Geology 39: 627–630.

Cowgill, E., Gold, R.D., Chen, X.H., Wang, X.F., Arrowsmith, J.R., and Southon, J., 2009. Low Quaternary slip rate reconciles geodetic and geologic rates along the Altyn Tagh fault, northwestern Tibet. Geology 37: 647–650,

Cowie, P.A., and Scholz, C.H., 1992. Growth of faults by accumulation of seismic slip. Journal of Geophysical Research 97: 11085 – 11095.

Cox, R.T., Van Arsdale R.B., and Harris J.B., 2001. Identification of possible Quaternary deformation in the northeastern Mississippi Embayment using quantitative geomorphic analysis of drainage-basin asymmetry. Geological Society of American Bulletin 113: 615–624.

Cox, K.G., Bell, J.D. and Pankhurst, R.J., 1979. The Interpretation of Igneous Rocks. George Allen & Unwin Ltd., London, 450 pp.

Debon, F., Afzali, H., Le Fort, P., and Sonet, J., 1987. Major intrusive stages in Afghanistan: typology, age and geodynamic setting. Geologisches Rundschall 76: 245–264.

Densmore, A.L., Gupta, S., Allen, P.A., and Dawers, N.H., 2007. Transient landscapes at fault tips. Journal of Geophysical Research 112: F03S08, doi: 10.1029/2006JF000560.

Douglass, J., Meek, N., Dorn, R.I., and Schmeeckle, M.W., 2009. A criteria-based methodology for determining the mechanism of transverse drainage development, with application to the southwestern United States. Geological Society of America Bulletin 121: 586–598.

England, P., and Houseman, G., 1986. Finite strain calculations of continental deformation: 2. Comparison with the India–Asia collision zone. Journal of Geophysical Research 91: 3664–3676.

England, P., and Molnar, P., 2005. Late Quaternary to decadal velocity fields in Asia. Journal of Geophysical Research 110: doi: 10.1029/2004JB003541.

Farah, A., Abbas, G., De Jong, K.A., and Lawrence, R.D., 1984. Evolution of the lithosphere in Pakistan. Tectonophysics 105: 207–227.

Francesco, T., and Marta, D.S., 2011. Geomorphological response of fluvial and coastal terraces to Quaternary tectonics and climate as revealed by geostatistical topographic analysis. Earth Surface Processes and Landforms 36: 1193–1208.

Frankel, K.L., Brantley, K.S., Dolan, J.F., Finkel, R.C., Klinger, R.E., Knott, J.R., Machette, M.N., Owen, L.A., Phillips, F.M., Slate, J.L., and Wenicke, B.P.,

2007a. Cosmogenic ^{10}Be and ^{36}Cl geochronology of offset alluvial fans along the northern Death Valley fault zone: Implications for transient strain in the eastern California shear zone. Journal of Geophysical Research 112: doi: 10.1029/2006JB004350.

Frankel, K.L., Dolan, J.F., Finkel, R.C., Owen, L.A., and Hoeft, J.S., 2007b. Spatial variations in slip rate along the Death Valley-Fish Lake Valley fault system determined from LiDAR topographic data and cosmogenic ^{10}Be geochronology. Geophysical Research Letters 34: doi: 10.1029/2007GL030549.

Frankel, K.L., Dolan, J.F., Owen, L.A., Ganev, P., and Finkel, R.C., 2011. Spatial and temporal constancy of seismic strain release along an evolving segment of the Pacific-North America plate boundary. Earth and Planetary Science Letters 304: 565–576.

Furuya, M., and Satyabala, S.P., 2008. Slow earthquake in Afghanistan detected by InSAR. Geophysical Research Letters 35: doi: 10.1029/2007GL033049.

Hadjimitsis, D.G., Papadavid, G., Agapiou, A., Themistocleous, K., Hadjimitsis, M.G., Retalis, A., Michaelides, S., Chrysoulakis, N., Toulios, L., and Clayton, C.R.I., 2010. Atmospheric correction for satellite remotely sensed data intended for agricultural applications: impact on vegetation indices. Natural Hazards and Earth System Sciences 10: 89–95.

He, J., and Chéry, J., 2008. Slip rates of the Altyn Tagh, Kunlun and Karakorum faults (Tibet) from 3D mechanical modeling. Earth and Planetary Science Letters 274: 50–58.

Heisinger, B., Lal, D., Jull, A.J.T., Kubik, P., Ivy-Ochs, S., Knie, K., and Nolte, E., 2002. Production of selected cosmogenic radionuclides by muons: 2. Capture of negative muons. Earth and Planetary Science Letters 200: 357–369.

Hellstrom, J., Paton J., Woodhead, J., and Hergt, J., 2008. Iolite: Software for spatially resolved LA-(quad and MC) ICPMS analysis: In Sylvester, P., (ed.) Laser Ablation ICPMS in the Earth Sciences: Current Practices and Outstanding Issues, Mineral. Association of Canada, Vancouver: 343–348.

Hetzel, R., Tao, M.X., Stokes, S., Niedermann, S., Ivy-Ochs, S., Gao, B., Strecker, M.R., and Kubik, P.W., 2004, Late Pleistocene Holocene slip rate of the Zhangye thrust (Qilian Shan. China) and implications for the active growth of the northeastern Tibetan Plateau. Tectonics 23: TC6006, doi: 10.1029/2004TCOO1653.

Hetzel, R.. Niedermann, S., Tao, M., Kubik, P.W., Ivy-Ochs, S., Gao, B., and Strecker, M.R., 2002. Low slip rates and long-term preservation of geomorphic features in Central Asia. Nature 417: 428 – 432.

Hilley, G.E., and Arrowsmith, J.R., 2008. Geomorphic response to uplift along the Dragon's Back Pressure Ridge, Carrizo Plain, California. Geology 36: 367–370.

Hoeft, J.S., and Frankel, K.L., 2010. Temporal variations in extension rate on the Lone Mountain fault and strain distribution in the eastern California shear zone-Walker Lane. Geosphere 6: 917–936.

Humphrey, N.F., and Konrad, S.K., 2000. River incision or diversion in response to bedrock uplift. Geology 28: 43–46.

Hunting Survey Corporation Limited 1960. Reconnaissance geology of part of Western Pakistan; a Columbo Plan Cooperative project: Canadian Geological Survey (Ottawa) for the Government of Pakistan, 550 p.

Jackson, J., Norris, R., and Youngson, J., 1996. The structural evolution of active fault and fold systems in central Otago, New Zealand: Evidence revealed by drainage patterns. Journal of Structural Geology 18: 217–234.

Jadoon, A.K., and Khurshid, A., 1996. Gravity and tectonic model across the Sulaiman fold belt and the Chaman fault zone in western Pakistan and eastern Afghanistan. Tectonophysics 254: 89 – 109.

Kalinowski A., and Olive S., 2004. ASTER Mineral Index Processing Manual. Remote Sensing Applications, Geoscience Australia, 36 p.

Kazmi, A.H., and Jan, M.Q., 1997. Geology and tectonics of Pakistan. Graphic Publishers, Karachi, Pakistan, 554 p.

Keller, E.A, Gurrola, L, and Tierney, T.E., 1999. Geomorphic criteria to determine direction of lateral propagation of reverse faulting and folding. Geology 27: 515–518.

Keller, E.A. and DeVecchio, D.E., 2012. Tectonic geomorphology of active folding and development of transverse drainage. Treatise on Geomorphology, Elsevier (in press).

Keller, E.A., and Pinter, N., 2002. Active Tectonics: Earthquakes, Uplift, and Landscape (second edition): Englewood Cliffs, New Jersey, Prentice Hall, 362 p.

Khan, S.D., and Mahmood, K., 2008. The application of remote sensing techniques to the study of ophiolites. Earth Science Reviews 89: 135–143.

Khan, S.D., and Glenn, N., 2006. New strike slip faults and litho-units mapped in Chitral (North Pakistan) using field and ASTER data yield regionally significant results. International Journal of Remote Sensing 27: 4495–4512.

Khan, S.D., Walker, D.J., Hall, S.A., Burke, K.C., Shah, M.T., and Stockli, L., 2009. Did Kohistan-Ladakh island arc collide first with India? Geological Society of America Bulletin: 121, 366–384.

Klootwijk, C.T., Gee, J.S, Peirce, J.W., Smith, G.M., and McFadden, P.L., 1998. An early India-Asia contact: Paleomagnetic constraints from Ninety East Ridge, ODP Leg 121. Geology 20: 395–398.

Lal, D., 1991. Cosmic ray labeling of erosion surfaces: *in situ* nuclide production rates and erosion models. Earth and Planetary Science Letters 104: 424–439.

Lasserre, C., Gaudemer, Y., Tapponnier, P., Meriaux, A.S., Van der Woerd, J., Yuan, D.Y., Ryerson, F.J., Finkel, R.C., and Caffee, M.W., 2002. Fast Late Pleistocene slip rate on the Leng Long Ling segment of the Haiyuan fault, Qinghai, China. Journal of Geophysical Research 107: B11, 2276.

Lasserre, C., Morel, P.H., Gaudemer, Y., Tapponnier, P., Ryerson, F.J., King, G.P., Metivier, F., Kasser, M., Kashgarian, M., Baichi, L., Taiya, L., and Daoyang, Y., 1999. Postglacial left-slip rate and past occurrence of $M \geq 8$ earthquakes on the western Haiyuan fault, Gansu, China. Journal of Geophysical Research 104: 17633 – 17651.

Lawrence, R.D., and Yeats, R.S., 1979. Geological reconnaissance of the Chaman Fault in Pakistan. In: Farah, A., and DeJong, K.A., (eds.), Geodynamics of Pakistan: 351–357.

Lawrence, R.D., Khan, S.H., and Nakata, T., 1992. Chaman fault, Pakistan-Afghanistan. In: Bucknam, R.C., Hancock, P.L., (eds.), Major Active Faults of the World-Results of IGCP project 206: Supplement to Annnales Tectonicae 6: 196–223.

Lawrence, R.D., Yeats, R.S., Khan, S.H., Subhani, A.M., and Bonelli, D., 1981. Crystalline rocks of the Spinatizha area, Pakistan. Journal of Structural Geology 3: 449–457.

Ludwig, K.R., 1980. Calculations of uncertainties of U-Pb isotope data, Earth and Planetary Science Letters 46: 212–220.

Ludwig, K.R., 2003. User's Manual for Isoplot 3.00, A Geochronological Toolkit for Microsoft Excel, Special Publication 4: Berkeley Geochronology Center Berkeley, California.

Mann, P., 2007. Global catalogue, classification and tectonic origins of restraining-and releasing bends on active and ancient strike-slip fault systems. In: Cunningham, W.D. and Mann, P. (eds.), Tectonics of Strike-Slip Restraining and Releasing Bends. Geological Society of London, Special Publications 290: 13–142.

Meade, B.J., 2007. Present-day kinematics at the India-Asia collision zone. Geology 35: 81–84.

Mériaux, A.-S., Ryerson, F.J., Tapponnier, P., Van der Woerd, J., Finkel, R.C., Xu, X., Xu, Z., and Caffee, M.W., 2004. Rapid slip along the central AltynTagh Fault:

Morphochronologic evidence from Cherchen He and Sulamu Tagh. Journal of Geophysical Research 109: doi: 10.1029/2003JB002558.

Mériaux, A.-S., Tapponnier, P., Ryerson, F.J., Xiwei, X., King, G., Van der Woerd, J., Finkel, R.C., Haibing, L., Caffee, M.W., Zhiqin, X., and Wenbin, C., 2005. The Aksay segment of the northern AltynTagh Fault: Tectonic geomorphology, landscape evolution, and Holocene slip rate. Journal of Geophysical Research 110: doi: 10.1029/2004JB003210.

Middlemost, E.A.K., 1985. Magmas and Magmatic Rocks. Longman, London, 266 pp.

Miller, R.B., Paterson, S.R., and Matzel, J.P., 2009. Plutonism at different crustal levels: Insights from the ~5–40 km (paleo-depth) North Cascades crustal section, Washington. Geological Society of America Special paper 456: 125-149.

Miller, S.R., and Slingerland, R.L., 2006. Topographic advection on fault-bend folds: Inheritance of valley positions and formation of wind gaps. Geology 34: 769–772.

Mohadjer, S., Bendick, R., Ischuk, A., Kuzikov, S., Kostuk, A., Saydullaev, U., Lodi, S., Kakar, D. M., Wasy, A., Khan, M. A., Molnar, P., Bilham, R., and Zubovich A.V., 2010. Partitioning of India-Eurasia convergence in the Pamir-Hindu Kush from GPS measurements. Geophysical Research Letters 37: doi: 10.1029/2009GL041737.

Molnar, P., and Dayem, K., 2010. Major intracontinental strike-slip faults and contrasts in lithospheric strength. Geosphere 6: 444-467.

Molnar, P., and Stock, J.M., 2009. Slowing of India's convergence with Eurasia since 20 Ma and its implications for Tibetan mantle dynamics. Tectonics 28: doi: 10.1029/2008TC002271.

Molnar, P., and Tapponnier, P., 1975. Cenozoic tectonics of Asia: Effects of a continental collision. Science 189: 419– 426.

Nagell, R.H., 1975. Reconnaissance of the geology and ore mineralization in part of the Chagai District, Pakistan, 1964: U.S. Geological Survey Open-File Report 75-550, 73 p.

Nicolson, K.N., Khan, M. and Mahmood, K., 2010. Geochemistry of the Chagai–Raskoh arc, Pakistan: Complex arc dynamics spanning the Cretaceous to the Quaternary. Lithos: 118: 338–348.

Nishiizumi, K., Imamura, M., Caffee, M., Southon, J., Finkel, R., and McAnich, J., 2007. Absolute calibration of Be-10 AMS standards. Nuclear Instruments & Methods in Physics Research B 258: 403–413.

Nishiizumi, K., Winterer, E., Kohl, C., Klein, J., Middleton, R., Lal, D., and Arnold, J., 1989. Cosmic ray production rates of ^{26}Al and ^{10}Be in quartz from glacially polished rocks. Journal of Geophysical Research 94: 17907–17915.

Oskin, M., and Burbank, D.W., 2007. Transient landscape evolution of basement cored uplifts: Example of the Kyrgyz Range, Tian Shan. Journal of Geophysical Research 112: doi: 10.1029/2006JF000563.

Oskin, M., Perg, L., Blumentritt, D., and Mukhopadhyay, S., 2007. Slip rate of the Calico fault: Implications for geologic versus geodetic rate discrepancy in the Eastern

California Shear Zone. Journal of Geophysical Research 112: doi: 10.1029/2006JB004451.

Owen, L.A., Caffee, M.W., Bovard, K.R., Finkel, R.C., and Sharma, M.C., 2006. Terrestrial cosmogenic nuclide surface exposure dating of the oldest glacial successions in the Himalayan orogen: Ladakh Range, northern India. Geological Society of America Bulletin 118: 383–392.

Owen, L.A., Cunningham, W.D., Windley, B.F., Badamgarov, J., and Dorjnamjaa, D., 1999. The landscape evolution of Nemegt Uul: a Late Cenozoic transpressional uplift in the Gobi Altai, southern Mongolia. In: Smith, B.J., Whalley, W.B., Warke, P.A., (eds.), Uplift, Erosion and Stability: Perspectives on Long-term Landscape Development. Geological Society of London, Special Publications 162: 201–218.

Owen, L.A., Frankel, K.L., Knott, J.R., Reynhout, S., Finkel, R.C., Dolan, J.F. and Lee, J., 2011. Beryllium-10 terrestrial cosmogenic nuclide surface exposure dating of Quaternary landforms in Death Valley. Geomorphology 125: 541–557.

Pearce, J.A., 1983. The role of sub-continental lithosphere in magma genesis at active continental margins. In Hawkesworth, C.J., and Norry, M.J. (Eds.), Continental Basalts and Mantle Xenoliths: Nantwich (Shiva Publications), 230–249.

Pearce, J.A., 1996. A User's Guide to Basalt Discrimination Diagrams: In Wyman, D.A. (ed.) Trace Element Geochemistry of Volcanic Rocks: Applications for Massive Sulphide Exploration. Geological Association of Canada, Short Course Notes 12: 79 – 113.

Pearce, J.A., Harris, N.B.W., and Tindle, A.G., 1984. Trace element discrimination diagrams for the tectonic interpretation of granitic rocks. Journal of Petrology 25: 956–983.

Pearce, S.A., Pazzaglia, F.J., and Eppes, M.C., 2004. Ephemeral stream response to growing folds. Geological Society of America Bulletin 116: 1223–1239.

Peltzer, G., and Saucier, F., 1996. Present-day kinematics of Asia derived from geologic fault rates. Journal of Geophysical Research 101: 27943 – 27956.

Peltzer, G., and Tapponnier, P., 1988. Formation and evolution of strike-slip faults, rifts, and basins, during the India-Asia collision: An experimental approach. Journal of Geophysical Research 93: 15085–15117.

Phillips, R.J., Parrish, R.R., and Searle, M.P., 2004. Age constraints on ductile deformation and long-term slip rates along the Karakoram fault zone, Ladakh. Earth and Planetary Science Letters 226: 305–319.

Qayyum, M., Niem, A.R., and Lawrence, R.D., 1996. Newly discovered Paleogene deltaic sequence in Katawaz basin, Pakistan, and its tectonic implications. Geology 24: 835–838.

Richards, J.A., 1999. Remote Sensing Digital Image Analysis: An Introduction, Springer-Verlag, Berlin, Germany, 240 p.

Rowan, L.C., and Mars, J.C., 2003. Lithologic mapping in the Mountain Pass, California area using Advanced Spaceborne Thermal Emission and Reflection Radiometer (ASTER) data. Remote Sensing of Environment 84: 350–366.

Ruleman, C.A., Crone, A.J., Machette, M.N., Haller, K.M., and Rukstales, K.S., 2007. Map and database of probable and possible Quaternary faults in Afghanistan: U.S. Geological Survey Open-File Report 2007-1103, 39 p.

Ryerson, F.J., Tapponnier, P. Finkel, R.C., Meriaux, A.-S., Van der Woerd, J., Lassiere, C., Chevalier, M.-L., Xiwei, X., and Harbing, L., 2006. Applications of morphochronology to the active tectonics of Tibet. Geological Society of America Special Papers 415: 61–86.

Scharer, K.M., Burbank, D.W., Chen, J., Weldon, R.J., Rubin, C., Zhao, R., and Shen J., 2004. Detachment folding in the southwestern Tian Shan, Tarim foreland, China: Shortening estimates and rates. Journal of Structural Geology 26: 2119–2137.

Searle, M.P., 1986. Structural evolution and sequence of thrusting in the High Himalayan, Tibetan Tethys and Indus Suture zones of Zannsker and Ladakh, western Himalaya. Journal of Structural Geology 8: 923–936.

Sella, G.F., Dixon, T.H., and Mao, A., 2002. REVEL: A model for recent plate velocities from space geodesy: Journal of Geophysical Research 107: doi: 10.1029/2000JB000033.

Shareq, A., Chmyriov, V.M., Stazhilo-Alekseev, K.F., Dronov, V.I., Gannon, P., Lubemov, B.K., Kafarskiy, A., and Malyarove, E.P., 1977. Mineral Resources of Afghanistan, 2nd edition. Afghan Geological and Mines Survey, Afghanistan.

Shaulis, B., Lapen, T., and Toms, A., 2010. Signal linearity of an extended range pulse counting detector: Applications to accurate and precise U-Pb dating of zircon by laser ablation quadrupole ICP-MS. G-Cubed 11: doi: 10.1029/2010GC003198.

Shen, Z., Wang, M., Li, Y., Jackson, D.D., Yin, A., Dong, D., and Fang, P., 2001. Crustal deformation along the Altyn Tagh fault system, western China, from GPS. Journal of Geophysical Research 106: 30607–30622.

Siddiqui, R.H., Khan, M.A., and Jan, Q., 2005. Petrogenesis of Eocene lava flows from the Chagai arc, Balochistan, Pakistan and its implications. Geological Bulletin University of Peshawar 38: 163 – 187.

Siddiqui, R.H., 1996. Magmatic evolution of Chagai-Ras Koh arc terrane and its implication for porphyry copper mineralization. Geologica 2: 87 – 119.

Siddiqui, R.H., 2004. Crustal evolution of the Chagai-Raskoh arc terrane, Balochistan, Pakistan. Unpublished Ph.D. Dissertation, University of Peshawar, Pakistan.

Sillitoe, R.H. and Khan, S.N., 1977. Geology of the Saindak porphyry copper deposit, Pakistan. Trans. Instn Min. Metall., Sec. 86: B27–B42.

Sillitoe, R.H., 1978. Metallogenic evolution of a collisional mountain belt in Pakistan, a preliminary analysis. Journal of the Geological Society of London 135: 377–387.

Simpson, G., 2004. Role of river incision in enhancing deformation. Geology 32: 341–344.

Stone, J.O., 2000. Air pressure and cosmogenic isotope production. Journal of Geophysical Research 105: 23753–23759.

Sun, S.S. and McDonough, W.F., 1989. Chemical and isotopic systematics of oceanic basalts: implications for mantle composition and processes. In: Saunders, A.D.

and Norry, M. (eds.) Magmatism in Ocean Basins. Geological Society of London Special Publication 42: 313-345.

Szeliga, W., Bilham, R., Schelling, D., Kakar, D.M., and Lodi, S., 2009. Fold and thrust partitioning in a contracting fold belt: Insights from the 1931 Mach earthquake in Baluchistan. Tectonics 28: doi: 10.1029/2008TC002265.

Tapponnier, P., Xu, Z. Roger, F., Meyer, B., Arnaud, N., Wittlinger, G., and Yang J., 2001. Oblique stepwise rise and growth of the Tibet Plateau. Science 294: 1671–1677.

Tapponnier, P.M., Mattauer, F.P., and Cassaigneau, C., 1981. Mesozoic ophiolite, sutures, and large scale tectonic movements in Afghanistan. Earth and Planetary Science Letters 52: 355–371.

Thatcher, W., 2007. Micro-plate model for the present-day deformation of Tibet. Journal of Geophysical Research 112: doi: 10.1029/2005JB004244.

Treloar, P.J., and Izatt, C.N., 1993. Tectonics of the Himalayan collision between the Indian Plate and the Afghan Block: A synthesis: In Treloar, P.J., and Searle, M.P., (eds.), Himalayan Tectonics. Geological Society of London, Special Publication 74: 69–87.

Ul-Hadi, S., Khan, S.D., Owen, L., and Khan, A.S., 2012. Geomorphic response to an active transpressive regime: a case study along the Chaman strike-slip fault, western Pakistan. Earth Surface Processes and Landforms (in revision).

Van der Woerd, J., Ryerson, F.J., Tapponnier, P., Gaudemer, Y., Finkel, R., Meriaux, A. S., Caffee, M.W., Guoguang, Z., and Qunlu, H., 1998. Holocene left-slip rate

determined by cosmogenic surface dating on the Xidatan segment of the Kunlun fault (Qinghai, China). Geology 26: 695–698.

Van der Woerd, J., Tapponnier, P., Ryerson, F.J., Meriaux, A.S., Meyer, B., Gaudemer, Y., Finkel, R.C., Caffee, M.W., Zhao, G.G., and Xu, Z.Q., 2002b. Uniform postglacial slip-rate along the central 600 km of the Kunlun fault (Tibet), from Al-26, Be-10, and C-14 dating of riser offsets, and climatic origin of the regional morphology. Geophysical Journal International 148: 356 – 388.

Van der Woerd, J., Xu, X., Li, H.B., Tapponnier, P., Meyer, B., Ryerson, F.J., Meriaux, A.S., and Xu, Z.Q., 2001. Rapid active thrusting along the northwestern range front of the Tanghe Nan Shan (western Gansu, China). Journal of Geophysical Research 106: 30475 – 30504.

Wheeler, R.L., Bufe, C.G., Johnson, M.L., and Dart, R.L., 2005. Seismotectonic map of Afghanistan with annotated bibliography: U.S. Geological Survey Open-File Report 2005-1264: 31p.

Wright, T.J., Parsons, B., England, P.C., and Fielding, E.J., 2004. InSAR observations of low slip rates on the major faults of western Tibet. Science 305: 236– 239.

Yamaguchi, Y., Kahle, A.B., Tsu, H., Kawakami, T., Pniel M., 1998. Overview of Advanced Spaceborne Thermal Emission and Reflection Radiometer (ASTER). IEEE Transactions on Geoscience and Remote Sensing 36: 1062–1073.

Yin, A., 2006. Cenozoic tectonic evolution of the Himalayan orogen as constrained by along-strike variation of structural geometry, exhumation history, and foreland sedimentation. Earth-Science Reviews 76: 1-131.

Yin, A., and Harrison, T.M., 2000. Geologic evolution of the Himalayan–Tibetan orogen. Annual Reviews of Earth and Planetary Science 28: 211–280.

Zhang, P.Z., Molnar, P., and Xu, X., 2007. Late Quaternary and present-day rates of slip along the Altyn Tagh Fault, northern margin of the Tibetan Plateau. Tectonics 26: doi: 10.1029/2006TC002014.

Appendix

Introduction to ASTER

The Advanced Spaceborne Thermal Emission and Reflection Radiometer (ASTER) covers a wide spectral region with 14 bands from the visible to the thermal infrared with high spatial, spectral and radiometric resolution along with the additional backward-looking near-infrared band, which provides stereo coverage. Each ASTER scene covers an area of 60 x 60 km. The ASTER instrument in itself consists of three separate subsystems. Each subsystem operates with its own telescope(s) in a different spectral region. The backward viewing telescope provides stereoscopic capability of ASTER with the near-infrared spectral band (band 3B). The sun-synchronous Terra spacecraft orbits around the earth at an altitude of 705 km with equatorial crossing at local time of 10:30 a.m. having a repeat interval of 16 days. The pertinent features of the ASTER instrument and its 15 data bands are provided in Table A1.

ASTER Data types

ASTER data is available in different forms from Level 1 to Level 4 (Table A2). I used L1A (one scene) and L1B (two scenes) products of ASTER Level-1 data and a brief introduction to these data types is provided below;

Table A1: Characteristics of ASTER instrument and bands (Abrams, et al., 2004)

Characteristic	VNIR	SWIR	TIR
Spectral Range	Band 1: 0.52 - 0.60 µm Nadir looking Band 2: 0.63 - 0.69 µm Nadir looking Band 3: 0.76 - 0.86 µm Nadir looking Band 3: 0.76 - 0.86 µm Backward looking	Band 4: 1.600 - 1.700 µm Band 5: 2.145 - 2.185 µm Band 6: 2.185 - 2.225 µm Band 7: 2.235 - 2.285 µm Band 8: 2.295 - 2.365 µm Band 9: 2.360 - 2.430 µm	Band 10: 8.125 - 8.475 µm Band 11: 8.475 - 8.825 µm Band 12: 8.925 - 9.275 µm Band 13: 10.25 - 10.95 µm Band 14: 10.95 - 11.65 µm
Ground Resolution	15 m	30m	90m
Data Rate (Mbits/sec)	62	23	4.2
Cross-track Pointing (deg.)	±24	±8.55	±8.55
Cross-track Pointing (km)	±318	±116	±116
Swath Width (km)	60	60	60
Detector Type	Si	PtSi-Si	HgCdTe
Quantization (bits)	8	8	12

Level-1 Data

The ASTER Level-1 data is provided to user community in two formats: Level-1A (L1A) and Level-1B (L1B) (http://asterweb.jpl.nasa.gov/data_products.asp). ASTER L1A data are reconstructed, unprocessed instrument data at full resolution and consist of the image data, the radiometric coefficients, the geometric coefficients and other auxiliary data without applying the coefficients to the image data, thus maintaining original data values (Abrams et al., 2004). All acquired image data are processed to L1A. On-board storage limitations on the spacecraft limit ASTER's acquisition to about 650 L1A scenes per day.

Level 1A: Geometric correction and radiometric calibration coefficients are appended but not applied to the image data. This product, therefore, does not match a map of any projection type. It is segmented into scene. All products are generated from this product.

Level 1B: This product is generated by applying the radiometric and geometric correction coefficients contained in Level1A. This product, therefore, does matches a map with a projection type selected by user.

The ASTER L1B Registered Radiance at the Sensor product contains radiometrically calibrated and geometrically co-registered data for all the channels acquired previously through the telemetry streams of 3 different telescopes in Level-1A. This product is created by applying the radiometric calibration and geometric correction for all the bands has been accomplished relative to the reference band of each sub-system. The L1B radiance product offers the same number of bands at the same resolution as the L1A. L1B data provide the input for generating higher Level-2 geophysical products. These L1B are produced at the Ground Data System (GDS) in Tokyo, Japan, and sent to the Land Process (LP) Distributed Active Archive Center (DAAC) for archiving, distribution, and further processing.

ASTER Level-1 scenes used in this study are;

1. L1B_003061420070625 09_20090430160636_20298.hdf
2. L1B_003061420070625 17_20090430160636_20288.hdf
3. L1A_003061420070625 09_20100706174759_417.hdf

These scenes were acquired on same day (June 14, 2007) with same orbit characteristics. L1B data was used in lithologic mapping while L1A was used for DEM extraction as Geometica10 favors processing L1A data.

Table A2: ASTER Standard and Semi-Standard Products (http://www.gds.aster.ersdac.or.jp)

Code	Name	Sensor*	Ground Resolution
L1A	Level 1A	V1, V2, S, T	V1(15m), V2(15m),S(30m), T(90m)
L1B	Level 1B	V1, V2, S, T	V1(15m), V2(15m),S(30m), T(90m)
B01V	Earth Surface Radiance VNIR	V	15m
2B01S	Earth Surface Radiance SWIR	S	30m
2B01T	Earth Surface Radiance TIR	T	90m
2B03	Earth Surface Temperature	T	90m
2B04	Earth Surface Emissivity	T	90m
2B05V	Earth Surface Reflectance VNIR	V	15m
2B05S	Earth Surface Reflectance SWIR	S	30m
3A01	Terrain Correction Image	V1,V2,S,T	V(15m),S(30m),T(90m)
4A01	Relativity DEM XYZ	V2	30m
4A01	Relativity DEM Z	V2	30m

* V1: VNIR bands 1, 2

V2: VNIR bands 3N, 3B

S: SWIR

T: TIR

GeoEye-1 Satellite

(The following information is gathered from GeoEye website and further information can be found on www.geoeye.com)

The GeoEye-1 satellite is equipped with the most advanced technology ever used in a commercial remote sensing system. The satellite collects images at 0.41 m panchromatic (black & white) and 1.65 m multispectral resolution. Data reflects ground sample distance resolution at Nadir for exclusive use by the U.S. government and any foreign government that the U.S. government may designate. Imagery sold to commercial customers will be resampled to 0.5 m resolution. GeoEye's current operating license with NOAA does not permit the commercial sale of imagery below 0.5 m resolution. The satellite can collect up to 700,000 square kilometers of panchromatic (and up to 350,000 square kilometers of pan-sharpened multispectral) imagery per day. This capability is ideal for large scale mapping projects. GeoEye-1 can revisit any point on Earth once every three days or sooner.

Imagery Products

Customers have a choice of ordering half-meter Geo™, GeoProfessional™ and GeoStereo™ imagery products, as well as imagery-derived products, including DEMs (digital elevation models) and DSMs (digital surface models), large-area mosaics, and feature maps.

Satellite Technical Capabilities

A polar orbiting satellite, GeoEye-1 orbits the Earth 15 times per day flying at an altitude of 681 kilometers or 423 miles with an orbital velocity of about 7.5 km/sec or 17,000 mi/hr. Its sun-synchronous orbit allows it to pass over a given area at about 10:30 a.m. local time every pass. The entire satellite turns and swivels very quickly in orbit to point the camera at areas directly below, as well as from side-to-side and front-to-back. This agility enables it to collect more imagery during a single pass.

Table A3: GeoEye-1 technical capabilities and data specifications. (A) Imaging & collection specifications of Geoeye-1. (B) Technical information about the Geoeye-1 commercial satellite; (http://launch.geoeye.com/LaunchSite/about/fact_sheet.aspx)

(A)

Launch Date	September 6, 2008 11:50:57 a.m. PDT
Camera Modes	• Simultaneous panchromatic and multispectral (pan-sharpened) • Panchromatic only • Multispectral only
Resolution	• 0.41 m / 1.34 ft* panchromatic (nominal at Nadir) • 1.65 m / 5.41 ft* multispectral (nominal at Nadir)
Metric Accuracy/ Geolocation	• Mono: 5 m CE90, horizontal, without GCP, exclusive of terrain displacement • Stereo: 4 m CE90, horizontal, without GCP 6 m LE90, vertical, without GCP These are specified as 90% CE (circular error) for the horizontal and 90% LE (linear error) for the vertical with no GCP (ground control point)
Swath Widths & Representative Area Sizes	• Nominal swath width - 15.2 km / 9.44 mi at Nadir • Single-point scene - 225 sq km (15x15 km) • Contiguous large area - 15,000 sq km (300x50 km) • Contiguous 1° cell size areas - 10,000 sq km (100x100 km) • Contiguous stereo area - 6,270 sq km (224x28 km) (Area assumes pan mode at highest line rate)

Table A3 continues on next page.

Table A3 continued.

Imaging Angle	Capable of imaging in any direction		
Revisit Frequency at 681 km Altitude (40° Latitud Target)	**Max Pan GSD (m)**	**Off Nadir Look Angle (deg)**	**Average Revisit (days)**
	0.42	8.3	10
	0.50	2.8	28
	0.59	2.1	35
Daily Monoscopic Area Collection Capacity	• Up to 700,000 sq km/day (270,000 sq mi/day) of pan-only area (equivalent to about the size of Texas) • Up to 350,000 sq km/day (135,000 sq mi/day) of pan-sharpened multispectral area (equivalent to about the size of New Mexico)		

(B)

Satellite Manufacturer	General Dynamics Advanced Information Systems
Electro-Optical Camera	ITT Corporation
Launch Facts	Boeing Corporation / Delta II vehicle / Vandenberg Air Force Base, CA
Satellite Weight	1955 kg / 4310 lbs
Satellite Storage and Downlink	1 Terabit recorder; X-band downlink (at 740 Mb/sec)
Operational Life	Fully redundant 7+ year design life; fuel for 15 years
Satellite Modes of Operation	• Store and forward • Real-time image and downlink • Direct uplink with real-time downlink
Orbital Altitude	681 kilometers / 423 miles
Orbital Velocity	About 7.5 km/sec or 17,000 mi/hr
Inclination/Equator Crossing Time	98 degrees / 10:30am
Orbit type/period	Sun-synchronous / 98 minutes

References

Abrams, M., Hook, S., and Ramachandran, B., 2004. ASTER User Handbook, Version 2. Jet Propulsion Laboratory, California Institute of Technology. Online: http://asterweb.jpl.nasa.gov/content/03_data/04_Documents/aster_user_guide_v2.pdf

ASTER data products, 2004. Jet Propulsion Laboratory, California Institute of Technology (http://asterweb.jpl.nasa.gov/data_products.asp)

GeoEye-1 Fact Sheet, 2008. GeoEye Information Services (http://launch.geoeye.com/LaunchSite/about/fact_sheet.aspx) and www.geoeye.com